Scuola di Dottorato
Università degli Studi di Milano - Bicocca

Department of Materials Science

PhD program in Materials Science and Nanotechnology

Optical investigation of phenomena induced by spin-orbit coupling in group IV heterostructures

Simone Rossi

Reg. Nr. 776561

Supervisor: Prof. Fabio Pezzoli
Tutor: Prof. Emiliano Bonera
Coordinator: Prof. Marco Bernasconi

XXXIV Cycle - Academic Year 2021/2022

Contents

1 Introduction **4**

2 Spin-orbit coupling **9**
2.1 Rashba and Dresselhaus effect 11
2.2 Spin-Hall effect 16

3 Optical spin orientation **22**

4 Hanle effect **28**

5 Spin-relaxation mechanisms **30**
5.1 Elliott-Yafet mechanism 30
5.2 D'yakonov-Perel mechanism 32
5.3 Bir-Aronov-Pikus mechanism 33
5.4 Hyperfine interaction 33

6 Materials: Si, Ge, Sn and their alloys **34**
6.1 Structural properties 34
6.1.1 Heteroepitaxy and strain 38
6.2 Electronic properties 40

7 Heterostructures **44**
7.1 Band alignment 44
7.2 Strain effects on energy band 48
7.3 Quantum wells 53
7.3.1 Modulation doping 56
7.3.2 Magnetotransport in 2D systems 57
7.3.3 Quantum-confined Stark effect 58

8 Chemical vapour deposition **64**
8.0.1 Low-energy plasma-enhanced CVD 66

8.0.2 Reduced-pressure CVD 66

9 Ge/$Si_{0.15}Ge_{0.85}$ multiple QWs p-i-n diodes 68

9.1 The Ge/$Si_{0.15}Ge_{0.85}$ p-i-n devices 68
9.2 Electrical investigation 69
9.3 Device simulation 73
9.4 Optical investigation 77

10 Emergent SOC phenomena in $Ge_{1-x}Sn_x$ heterostructures 87

10.1 Recombination dynamics in $Ge_{1-x}Sn_x$ epilayers 88
10.2 p-type modulation-doped $Ge_{0.91}Sn_{0.09}$ quantum well 102
10.2.1 Magnetotransport measurement 102
10.2.2 Electrical characterization 105
10.2.3 Optical characterization 108
10.2.4 Inverse spin-Hall effect 117

11 Conclusions 124

A 128

A.1 Continuous-wave PL set-up 128
A.2 Time-resolved PL set-up 130
A.3 Photocurrent measurements 133
A.4 Magnetic field characterization 133

B 136

B.1 Stokes analysis 136

C 139

C.1 Additional experimental results: p-i-n diodes 139
C.2 Additional experimental results: $Ge_{1-x}Sn_x$ epilayer 145
C.3 Additional experimental results: $Ge_{1-x}Sn_x$ QW 146

D **149**
D.1 Nextnano simulation code 149

Bibliography **154**

Acknowledgement **185**

1 Introduction

The technological advancement of Si-based electronics has been enabled by the continuous downscaling process of the integrated circuits. In 2021 IBM has proposed a technology based on components with the astonishing size of 2 nm, which would result in the implementation of approximately 50 billion transistors in less than 1 cm^2 [1]. However, such aggressive miniaturization process has brought the industry to face problems associated to the implementation of the next technology nodes. These ”future” components are indeed limited by energy dissipation in the dormant state (ON/OFF leakage currents) and the emergence of quantum-mechanical effects [2]. These phenomena become increasingly important as we approach sizes close to the atomic scale and open the discussion about the possibility to realize smaller devices. We are nowadays at the point where the Moore's law may very soon reach a halt.

A call for disruptive technologies based on alternatives to electron charge has therefore emerged. Within this framework, spintronics has arisen as a blossoming field that brings promising potential in the information and communication technology [3–5]. Spintronics aims at utilizing the spin degree of freedom for electronic applications and therefore relies on the the generation, manipulation, and detection of a spin current [6, 7]. To do so a new generation of devices, which includes spin-FETs [8], spin-lasers [9] and spin-LEDs [10], is required in order to adapt to this paradigm shift. At variance of charge transport, spin currents can be obtained also without a net mass flow. This feature is of key importance to overcome the heat dissipation problem, which arises from leakage currents and can damage the device functionality.

Spintronics bases its functioning on the spin-orbit coupling (SOC), a relativistic coupling of the spin degree of freedom to the momentum of carriers. The SOC lifts the spin degeneracy of the band structure without requiring external fields. The removal of this degeneracy is described in low dimensional semiconductor heterostructures, such as quantum wells (QWs), by two Hamiltonian terms,

namely Rashba and Dresselhaus contributions, whose origin is found in the structure and bulk inversion asymmetry (SIA and BIA, respectively) [11–17]. The zero-field spin splitting permits for example the control of the spin polarization via a gate voltage [16–19], making the Rashba effect a perfect tuning knob to be engineered for spintronics applications. This is immediately clear in the prototypical spintronics device proposed by Datta and Das: the spin-FET [8]. Here, after the injection of the spin into a two-dimensional electron spin (2DEG) channel via a ferromagnetic electrode, the spin in manipulated by an electric field applied to the gate. In this framework, the Rashba field would be the perfect candidate to be exploited in the gate functioning.

Group IV materials are a promising platform to study the Rashba interaction as the centrosymmetric lattice gives a negligible BIA, thus removing the Dresselhaus term. This ultimately results in the suppression of spin relaxation mechanisms, known as Dyakonov-Perel, and a lengthening of the spin lifetime and spin diffusion length [20].

Among group IV semiconductors, Si and Ge as well as their alloys are low-cost materials compatible with nowadays microelectronics. They have proven over the years to be viable solid-state platforms for spin-based information [21–23]. Their long spin lifetime [21, 24, 25] and diffusion length [26, 27] as well as the long spin decoherence time [28] make them suitable candidates for future applications. Additionally, the well-established manufacture developed for these materials opened up the way to bandgap and strain engineering as further degrees of freedom to tune the spin dependent phenomena. Despite these appealing results, the Rashba physics of Ge heterostructures is still vastly unknown. Some results have been obtained from electrical measurements [29] but no optical investigation has been carried out so far. All-optical techniques prevent spin depolarization arising from interfaces between ferromagnetic and semiconductor materials, which affect electrical measurements and mask the intrinsic spin lifetime [30]. With this in mind, the starting point of this thesis is the study of the Rashba effect via photoluminescence (PL) in structurally asymmetric p-i-n diodes, where

the intrinsic region is composed of 50 $Ge/Si_{0.15}Ge_{0.85}$ QWs.

In the last decade another group IV material, namely Sn, has started to attract some interest in the community. As an heavier element it intrinsically possesses a stronger SOC with respect to Si and Ge, enhancing the spin-dependent properties. This feature can be exploited by alloying Ge and Sn to form $Ge_{1-x}Sn_x$ binaries. However, the strong out-of-equilibrium condition required for the material growth, due to the low (∼1 %) Sn solubility in Ge, has precluded for a long time the investigation of this alloy. Only in the last decade advancements in out-of-equilibrium growth technique allowed for the realization of samples with sufficient crystalline quality [31], leading to the first observed direct bandgap group IV material [32, 33] and, consequently, to the first group-IV-based laser [34]. Despite these promising results, spin physics of $Ge_{1-x}Sn_x$ remains vastly unexplored [35, 36]. Within this contest, we developed a magneto-optical technique that aims at unveiling the spin lifetime in $Ge_{1-x}Sn_x$ epilayers. This technique has been introduced since the emission range of $Ge_{1-x}Sn_x$ lies in the infrared, even above 2000 nm: a challenging region for time-resolved techniques, wehere only expensive superconducting Ge nanowires might be able to operate. The technique introduced in this thesis performs carrier lifetime estimation by exploiting the Hanle effect via well consolidated continuous-wave photoluminescence (CWPL) analysis, for which conventional and less expensive semiconductor-based detectors are available.

Additionally, we point out that the Rashba-induced zero field spin splitting gives origin also to intriguing phenomena such as the (inverse) spin-Hall effect, where a charge (spin) current is transformed into a spin (charge) transverse current [37, 38]. The stronger SOC offered by the $Ge_{1-x}Sn_x$ alloy compared to Ge and the additional degree of freedom offered by the low dimensionality constitute an interesting playground to optically address the inverse spin-Hall effect in $Ge_{1-x}Sn_x/Ge$ QW.

To summarize, this thesis focuses on the study of the SOC in heterostructures of group IV materials via polarization-resolved photoluminescence. In particular

we focus on Ge and $Ge_{1-x}Sn_x$ alloys as they possess a stronger SOC compared to Si, thus enhancing spin-depended effects. On top of this, we leverage bandgap and strain engineering as a further degrees of freedom to tailor the SOC and to better study spin-dependent properties in Si-compatible devices. Our analysis is carried out at first on Ge QWs embedded in a p-i-n diode to study the tuning of the Rashba field by an external electric field and then on $Ge_{1-x}Sn_x$ systems to investigate spin-to-charge interconversion phenomena.

This thesis is organized as follows. From Ch. 2 to Ch. 8 we summarize the theoretical fundation of this work. Specifically, we introduce the process of optical spin orientation, the spin-orbit coupling and the Hanle effect. In addition, we discuss the materials and the epitaxial growth of the heterostructures studied in this work.

Then, in Ch. 9 we describe the experimental results on the Rashba physics occurring in asymmetric Ge QWs embedded in the intrinsic region of a p-i-n diode. This device allows for the application of an external bias to tune and explore the Rashba effect in low dimensional systems. An electrical characterization shows the expected diode response and an 8-bands $\mathbf{k}\cdot\mathbf{p}$[1] calculation confirms the type-I band alignment as well as the band bending due to the built-in bias. The optical investigation shows that a strong effect on the PL polarization is obtained by changing the excitation power density while only a reduced effect is found with the application of a bias. These results are further supported by time-resolved photoluminescence measurements (TRPL).

Finally, in Ch. 10 we shift our attention to $Ge_{1-x}Sn_x$ alloys. At first we investigate a set of samples with variable Sn content. We determine the carrier lifetime by applying, for the first time to group IV materials, a steady-state magneto-optical technique based on the Hanle effect. Our investigation unveils a carrier lifetime of as long as 2 ns and the presence of crystal defects through the emergence of non-radiative recombination centres.

We then focus our efforts onto a novel system constituted by modulation-

[1] $\mathbf{k}$ is the wavevector and $\mathbf{p}$ is the quantum-mechanical momentum operator.

doped $Ge_{0.91}Sn_{0.09}$ QWs embedded in Ge barriers. These heterostructures are found to host a two-dimensional-hole-gas (2DHG) at low temperature, opening the path for the investigation of new spin physics. Photoluminescence analysis resulted in a sizable and polarized emission. Power dependent Hanle effect measurements enables us to extract a few-ns-long carrier lifetime. Finally we observed the emergence of spin-to-charge interconversion and we characterized it by extracting the spin-Hall angle.

The main results obtained in this work are summarized in Ch. 11.

In Appendix A we describe the experimental set-up used for the optical investigations. In Appendix B we introduce the Stokes analysis, that has been used for the analysis of the polarization. In Appendix C we show additional results on devices that are not discussed in the main text. Finally, in Appendix D we report the code used for the simulation of the p-i-n diodes.

2 Spin-orbit coupling

According to a semiclassical treatment the spin-orbit coupling, that is, the coupling between the orbital and the spin degrees of freedom, is a relativistic correction to the electron energy levels.

We focus now on an hydrogen atom and then we expand the results to solid-state materials. In the former, the positively charged nucleus generates a radial electric field $\mathbf{E}$ that is perceived by the electron in its rest frame as an effective magnetic field:

$$\mathbf{B_{eff}} = -\frac{\mathbf{v} \times \mathbf{E}}{c^2} \tag{1}$$

where $\mathbf{v}$ is the velocity of the electron and c is the speed of light.

We can rewrite Eq. 1 by using the radial coordinates, i.e. $\mathbf{E} = 1/e\,\partial_r V(r)\hat{\mathbf{r}}$ where e is the electron charge and $V(r)$ is the potential of the central field. Also, using the momentum operator $\mathbf{p} = m_e\mathbf{v}$, where m_e is the electron mass, and the angular momentum $\mathbf{L} = \mathbf{r} \times \mathbf{p}$ we get:

$$\mathbf{B_{eff}} = \frac{1}{m_e\, ec^2}\frac{1}{r}\frac{\partial V(r)}{\partial r}\mathbf{L} \tag{2}$$

The magnetic moment of the electron $\boldsymbol{\mu} = -g\mu_b/\hbar\,\mathbf{S}$, where g is the g-factor, μ_b is the Bohr magneton and $\mathbf{S}$ is the spin operator ($\mathbf{S} = \hbar\boldsymbol{\sigma}/2$, $\boldsymbol{\sigma}$ being the Pauli spin matrices), interacts with the magnetic field via:

$$\mathrm{H_{SOC}} = -\boldsymbol{\mu} \cdot \mathbf{B_{eff}} = \frac{-g\,\mu_b}{\hbar\, m_e^2\, e\, c^2}\frac{1}{r}\frac{\partial V(r)}{\partial r}\mathbf{S} \cdot \mathbf{L} = \lambda_{\mathrm{SO}}\,\mathbf{S} \cdot \mathbf{L} \tag{3}$$

here λ_{SO} is the spin-orbit coupling constant that depends on the atomic number Z. In the hydrogenoid model λ_{SO} scales as Z^4. However, this dependence is reduced to Z^2 for heavier materials once the screening of core electrons is taken into account. Equation 3 explicitly shows the coupling between the angular and the spin degree of freedom entering into the SOC Hamiltonian.

The effect of the SOC can be seen more easily by rewriting Eq. 3 in the form:

$$\mathrm{H_{SOC}} \sim \frac{g\,\mu_b}{2\,m_e\,c^2}\,(\mathbf{E}\times\mathbf{p})\cdot\boldsymbol{\sigma} \tag{4}$$

In relativistic quantum theory, $2m_ec^2$ is the energy gap between an electron and a positron, i.e., approximately 1 MeV [39]. Therefore, the SOC is negligible for a particle with non-relativistic momentum in a vacuum.

To expand this theory to condensed matter systems we have to consider that in crystals we have to describe the electron motion via energy bands and crystal momentum. The SO Hamiltonian in solids results to be a generalised version of Eq. 4:

$$\mathrm{H_{SOC}} \sim \frac{\hbar}{m_e^2\,c^2}\,(\nabla V\times\mathbf{p})\cdot\boldsymbol{\sigma} \tag{5}$$

where the potential V is now a sum of the periodic crystal potential V_0 and disorder potential V_{imp} stemming from the presence of impurities, lattice defects, etc... We point out that for the case of typical semiconductors, the energy bandgap is now in the order of 1 eV. Thus, when compared to a particle system, semiconductors show an enhancement of about six orders of magnitude of the SOC, resulting in sizable effects.

If we compare Eq. 4 to the Zeeman Hamiltonian:

$$\mathrm{H_Z} \sim \mu_b\,\mathbf{B}\cdot\boldsymbol{\sigma} \tag{6}$$

It turns out that the SOC introduces a Zeeman-like splitting in the energy levels due to an effective magnetic field [16, 40]:

$$\mathbf{B}(\mathbf{p}) = -\mu_b(\nabla\mathbf{V}\times\mathbf{p})/mc^2. \tag{7}$$

In the following we discuss two important effects that are relevant for this thesis and arise because of the spin-orbit coupling. These are the Rashba/Dresselhaus and the spin-Hall effects.

2.1 Rashba and Dresselhaus effect

The zero field spin splitting described in the introduction of this chapter is a consequence of the SOC and is typically described, in two-dimensional systems, by Rashba and Dresselhaus terms in the effective Hamiltonian of the system $H_{SOC} = H_R + H_D$, with:

$$H_R = \alpha\,(k_y\,\sigma_x - k_x\,\sigma_y) \tag{8}$$

$$H_D = \beta\,(k_x\,\sigma_x - k_y\,\sigma_y) + \gamma\,(-\sigma_x\,k_x\,k_y^2 + \sigma_y\,k_y\,k_x^2) \tag{9}$$

where α is the Rashba parameter, β and γ the Dresselhaus parameters [20, 41]. Both Rashba [42–45] and Dresselhaus [46] spin-splitting generate a contribution that is linear in the electron wave vector **k**; however, the Dresselhaus SOC adds also a cubic contribution in **k**.

The perturbative Hamiltonian terms described in Eqs. 8 and 9 find their origin in the perturbation of the lattice. In particular, both Rashba and Dresselhaus contributions arise from the breaking of the crystal symmetry.

If we consider a lattice composed of different atomic species, like in III-V systems, then microscopically the crystal is no more symmetric under a point inversion. An electron travelling within such lattice can encounter an atom of one type and close to it an atom of a different element. This different nature creates a local electric dipole and therefore a local electric field. The overall effect for the whole lattice can be described, via the SOC, as an effective magnetic field which lifts the spin degeneracy [11, 13, 14]. This kind of symmetry breaking of the lattice is known as bulk inversion asymmetry (BIA) and is associated to the Dresselhaus term.

In semiconductor quantum structures, the spin degeneracy can be lifted not only because of a BIA but also via a structure inversion asymmetry (SIA) of the confining potential, which is associated to the Rashba effect [11, 13, 14]. This potential can be intrinsic, if it arises from the structure itself, like in the case of asymmetrically doped structures. In this case, the asymmetry can be modulated

by adjustments at the growth stage by changing the doping concentration or by changing the distance between the doped layer and the active region via the introduction of a suitable undoped spacer. Additionally, the electric potential can also be external, like in the case of a bias applied to a p-i-n diode. The structural imbalance introduced in this way generates a gradient of an electric field across the whole structure. Through the SOC, this electric field is perceived as an effective magnetic field (Rashba field) that splits the spin-degenerated bands. The tunability via the doping as well as an external electric field can be exploited to manipulate the magnitude of the Rashba field, thus offering a practical tool for spintronics applications.

The linear Rashba and Dresselhaus terms split the spin degeneracy at the zone centre creating a band structure as schematically shown in Fig. 1a [17, 41]. When only SIA or BIA contribution is present, the energy dispersion is illustrated in Fig. 1b being the result of the revolution around the energy axis of two parabolas symmetrically displaced with respect to $\mathbf{k} = 0$. When SIA and BIA are present at the same time, the band structure consists of two revolution paraboloids with revolution axes symmetrically shifted in opposite directions with respect to $\mathbf{k} = 0$, see Fig. 1c. If we consider the projection on the $k_x k_y$ plane of the band structure at the Fermi energy, we obtain the spin orientation for both Rashba and Dresselhaus coupling that are shown by red arrows in Figs. 1d-g. For the SIA case, the electron spin is always perpendicular to the k-vector, see Fig. 1d. By contrast, for the BIA contribution, the orientation between the spin and the k-vector depends on the direction of $\mathbf{k}$, see Fig. 1e. In the presence of both SIA and BIA terms, their superposition generates a spin texture that is a weighted average of the two contributions. We have shown in Fig. 1f the case when BIA = SIA, while a more general situation, that is SIA $\neq$ BIA, is illustrated in Fig. 1g [17, 41].

An example of successful exploitation of the Rashba and Dresselhaus effect interplay was shown by Balocchi et al. [47] in GaAs QWs. In their work they properly adjusted BIA and SIA terms by changing the device structure as well as by applying an external electric field. This resulted in a fruitful effect on the spin

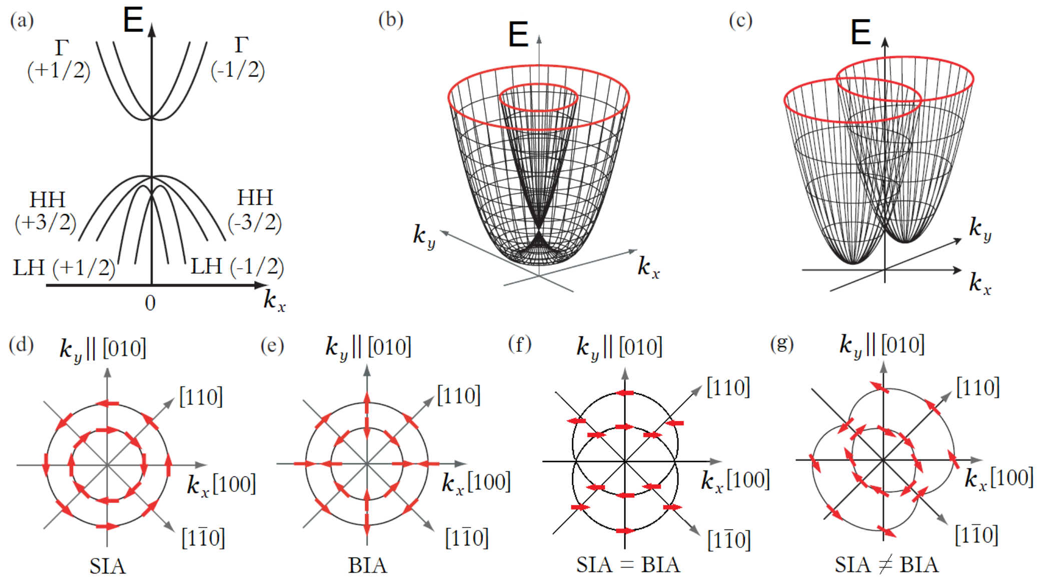

Figure 1: (a) SIA/BIA-induced spin splitting of the bands. Here ±1/2 or ±3/2 label the eigenstates with fixed spin components. (b) Schematic band structure for k-linear terms of the form of Eqs. 8 or 9 in the Hamiltonian. The energy E is plotted as a function of k_x and k_y in with only one type of inversion asymmetry (BIA or SIA) and in (c) for both BIA- and SIA-induced k-linear terms. (d-g) Distribution of spin orientations (red arrows) at the Fermi energy for different strengths of the BIA and SIA terms. Here we assumed in Eqs. 8 and 9 that $\alpha, \beta > 0$. Adapted from [17].

lifetime. In particular, they measured a (111)-oriented GaAs QW embedded in a p-i-n diode by TRPL and showed that under the application of an external bias the Rasbha field could balance the Dresselhaus field causing marked increase of the electron spin relaxation time from 0.5 to 30 ns when the electric field was changed from 20 (built-in electric field) to 55 kV/cm [47].

Quantum wells based on group IV elements do not possess the BIA because of their centrosymmetric crystal structure. This causes a negligible Dresselhaus term and thus also a suppression of the spin relaxation arising from this phenomemon. In this thesis we focus on the study of Ge QWs where only SIA can be present. This simplifies the study of the Rashba physics.

The role of the electric field on the electron spin polarization within Ge/ $Si_{1-x}Ge_x$ QW system remains mostly unexplored. Only Virgilio and Grosso in Ref. [48] theoretically investigated this effect using a tight-binding method. Their findings are shown in Fig. 2b where the spin polarization is calculated as a function of energy for different electric field intensities from 0 to 7.5×10^{-2} kV/cm.

An almost full polarization (96%) is found upon resonant excitation under no bias. In their work, the absorption coefficient of circularly polarized light is directly compared to the calculated spin polarization (S_0) of conduction-band (CB) electrons. In this way the relations between the feature of the polarization spectrum and the main transitions involving valence band (VB) and CB states at the zone centre are directly correlated. The maxima of S_0 are found at the HH1-cΓ1 (where HH stands for heavy-hole) and HH1-cΓ2 resonances, while minima are associated to the LH1-cΓ1, LH3-cΓ1, and SO-cΓ1 transitions. Additionally, they found out that regardless of the excitation energy, the electric field causes a loss of polarization which reduces the polarization by ten times in the investigated range. The origin of this loss of polarization is ascribed to the mixing of the orbital character of the wavefunction caused by the Rashba field. However, this effect has still not been confirmed from an experimental point of view.

With this in mind, Ch. 9 is devoted to the optical investigation of spin polarization in $Ge/Si_{0.15}Ge_{0.85}$ QWs embedded within a p-i-n diode structure. The

asymmetrical doping of the diode structure ensures the presence of the Rashba field and allows an external manipulation via an applied bias.

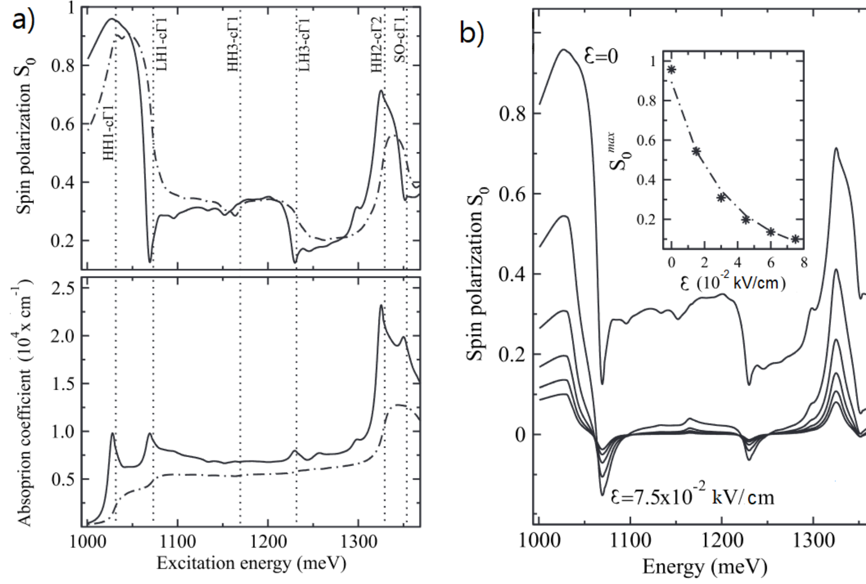

Figure 2: (a) In the upper panel: spin polarization S_0 as a function of the photon energy for conduction electrons optically excited by right-handed circularly polarized light. In the lower panel: corresponding absorption spectrum. Solid (dashed) lines represents the absorption spectrum when the excitonic contribution is (not) taken into account in the calculations. The threshold energies for the relevant interband transitions are indicated by vertical labels and dotted lines. (b) Spin polarization calculated as a function of energy at different electric field (ε) strength, ranging from zero to $7.5{\times}10^{-2}$ kV/cm. Adapted from Ref. [48].

2.2 Spin-Hall effect

Another fascinating effect originating from the SOC is the so called spin-Hall effect (SHE) [37, 38, 49, 50]. Without loss of generality, we deal from now on with spin-polarized electrons but the analogous discussion holds also for holes. It should be noted that in group IV materials the shorter spin lifetime and diffusion length of holes compared to electrons make the observation of SHE in the VB harder to achieve [51, 52].

Just like the classical Hall effect [53] where electron and hole trajectories are bent in an opposite transverse direction with respect to the motion due to Lorentz force, in the SHE carriers with opposite spins are scattered along opposite directions that are transverse to the carriers motion, even in the absence of an external magnetic field. This effectively yields a pure spin current, which can be thought as a combination of a spin-up current in one direction and a spin-down current in the opposite direction, resulting in a motion of angular momentum associated to no net charge displacement.

The SHE emerges in materials with large SOC where a longitudinal charge current ($\mathbf{j_c}$) is converted into a transverse spin current ($\mathbf{j_s}$) due to the velocity gained, for instance, by the electrons after spin-dependent scattering. The phenomenological relation describing the SHE is [13, 54]:

$$\mathbf{j_s} = \Theta_{SH}\,\mathbf{j_c} \times \mathbf{S} \tag{10}$$

where Θ_{SH} is the spin-Hall angle. The spin-Hall angle gives the efficiency of the conversion between charge current and spin current, thus $\Theta_{SH} = 1$ means that for a given charge current an equal pure spin current is generated perpendicularly.

The spin-dependent scattering mechanism can occur through two types of mechanisms. In the first, impurities with strong SOC scatter the travelling electrons with different spin projections towards opposite directions. This extrinsic mechanism originates from Mott scattering and side-jump mechanism and is at the core of the prediction of the SHE originally formulated by Dyakonov and

Perel in 1971 [37, 49]. The second mechanism, which is usually referred to as the intrinsic SHE, arises from spin-dependent distortion of electron trajectories due to the SOC of the material itself [55, 56].

In a structurally asymmetric heterostructure, the second mechanism might arise because of the Rashba-effect. In this case the Rashba effect modifies the velocity according to $\mathbf{v} = -(\alpha_R/\hbar)\,\mathbf{z} \times \boldsymbol{\sigma}$ where $\mathbf{z}$ is the propagation axis [16].

We want to highlight that the reverse process to the SHE can exist, namely the inverse spin-Hall effect (ISHE), where a pure spin current is transformed into a perpendicular charge current. Due to the Osanger reciprocity [57] we can write down that:

$$\begin{cases} \mathbf{j_s^{SHE}} = \Theta_{\mathrm{SH}} \left(-\frac{\hbar}{2e}\right) \mathrm{j_c}\,[\mathbf{z} \times \mathbf{S}] \\ \\ \mathbf{j_c^{ISHE}} = \Theta_{\mathrm{SH}} \left(-\frac{2e}{\hbar}\right) \mathrm{j_s}\,[\mathbf{z} \times \mathbf{S}] \end{cases} \tag{11}$$

where $\mathbf{j_s^{SHE}}$ and $\mathbf{j_c^{ISHE}}$ are the charge and spin current, respectively, $\mathbf{z}$ is the direction of the initial current and $\mathbf{S}$ the spin orientation of the spin current.

A simplified yet clear representation of the SHE and the ISHE is reported in Fig. 3.

The presence of SIA/BIA is fundamental for the observation of the (I)SHE. Indeed, the nonequilibrium spin density occurs as a consequence of an electric field and scattering-induced redistribution of carriers at the Fermi surface with a spin texture given by one of those shown in Figs. 1d-g. Under the application of an electric field along, e.g., the x axis, the Fermi contour is displaced by Δk (see Fig. 4a). As shown in Fig. 4b, owing to the momentum displacement the spins are no more completely perpendicular to their wavevector and start to precess around the local Rashba field, ultimately acquiring a spin component along +z for $k_y > 0$ and along -z for $k_y < 0$. The charge current applied along x thus results in a spin current along the y direction since carriers with antiparallel z-component of the spin are deflected along opposite directions.

A typical investigation of ISHE is performed on Hall bar devices where a cur-

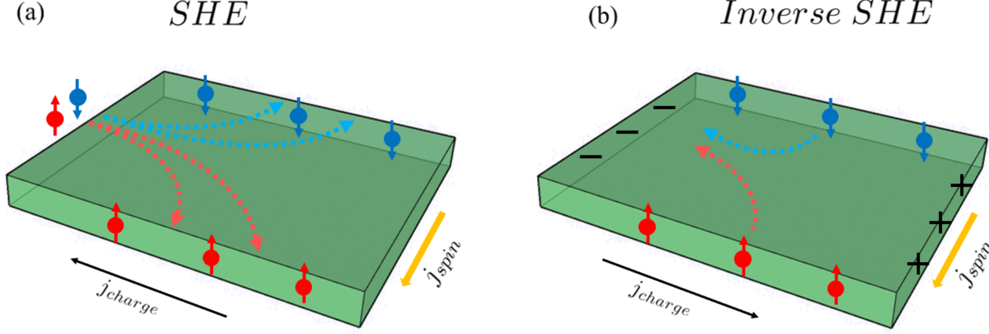

Figure 3: Schematic representation of the spin-to-charge interconversion phenomena. (a) Spin-Hall effect where charge current flowing through the device generates a separation of spin-up and spin-down carriers leading to a transverse spin current. (b) Inverse spin-Hall effect where a pure spin current generates a charge accumulation at the edges of the structure. Adapted from [50].

rent is sourced along the longitudinal (main) channel while shining a laser perpendicularly to the surface of the sample and measuring the photovoltage generated across the transverse (side) channel. In this framework optical spin orientation (discussed in Ch. 3) is a building block that is required for the generation of the out-of-equilibrium spin polarized population. These optically generated carriers travel through the Hall bar and experience the spin-dependent transverse deflection generating the ISHE [59–62].

The generated transverse voltage (V_T) is given by [62]:

$$V_T = \Theta_{SH}\, \rho_N\, w\, j_c\, P \tag{12}$$

where ρ_N is the resistivity of the sample, w the Hall bar width and P the carrier spin polarization[2] [62, 63].

The ability to create a robust pure spin current without magnetic materials is intriguing, and the simplicity and efficiency of this approach is desirable for

[2]We used that $\Theta_{SH} = \rho_{SH}/\rho_N$, $j_s = j_c\, P$ and $\mathbf{E}_\perp = \rho_{SH}\, \mathbf{j_s} \times \sigma$ where ρ_{SH} is the spin-Hall resistivity, $\mathbf{E}_\perp$ is the transverse electric field and σ is the spin polarization unit vector.

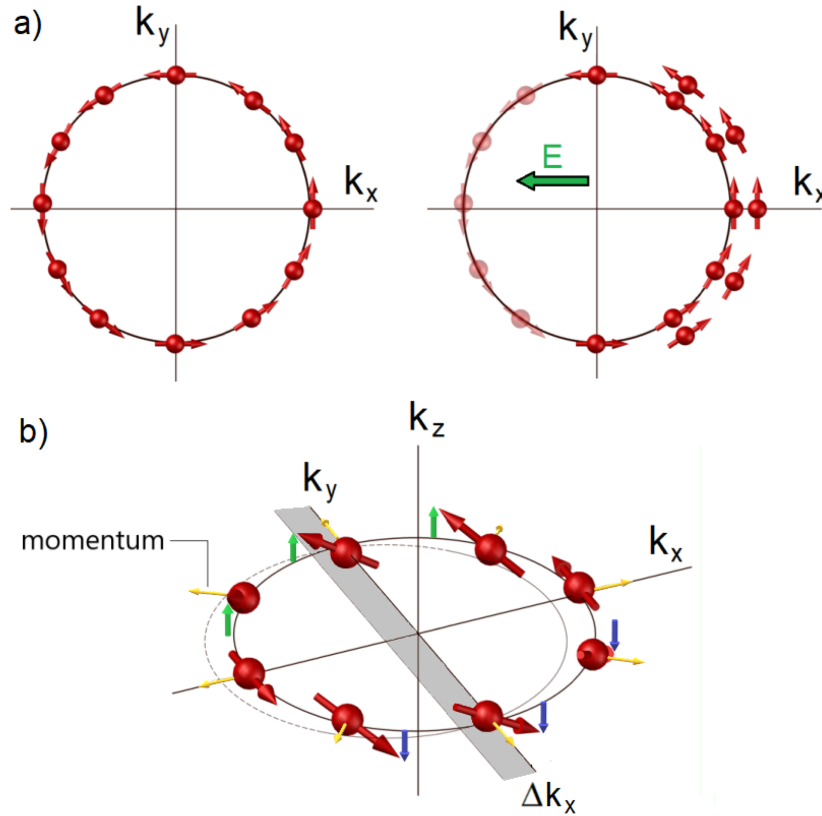

Figure 4: (a) Left panel: Rashba spin texture for states in equilibrium with zero net spin density. Right panel: nonequilibrium redistribution of carriers when an electric field is applied resulting in a nonzero spin density [50]. (b) Schematic representation of the generation of a pure spin current in a system with SIA. Here a shift of the Fermi contour by Δk is induced via the application of a current along the x axis. The spins (red arrows) are not perpendicular to the momentum (yellow arrows) and thus they start precessing around the local Rashba field. This causes the spin to acquire a component along +z for $k_y > 0$ (green arrows) and -z for $k_y < 0$ (blue arrows) that moves oppositely, generating a pure spin current along the y axis. Adapted from [58].

potential technological applications. A first observation of the SHE was done in III-V system by Bakun et al. in 1984 [64], yet a significant interest in this phenomenon was found only twenty years later after the publication of the works by Kato et al. in 2004 [65] and Wunderlich et al. in 2005 [66]. Controlling spin-related material properties by electronic means is a key step towards future spintronics technologies.

Some work has been done in the investigation of the SHE in various materials by evaluating the spin-Hall angle. The dependence of the SHE by the strength of the SOC has led people to study heavy metals such as Pt [67] or Ta [68]. Additionally, interesting results have also been demonstrated in GaAs [62]. Indeed, Okamoto et al. [62] showed that the application of an electric field to GaAs can lead to intervalley transitions selectively populating L and Γ-states. The former states have significantly stronger SOC than the latter, owing to the larger p-type character arising from stronger hybridization with the p-bands at finite wavevector. These results showed that an external electric bias can significantly modify the spin-Hall angle of materials through intervalley transitions, offering an alternative approach in the control of the spin-Hall angle. For reference, we report in Table 1 a list of values of the spin-Hall angle that are available in literature.

In this thesis we study the ISHE in a boron-modulation-doped $Ge_{1-x}Sn_x$/Ge QW. The doping layer provides the asymmetry required to the system to break the structural symmetry, inducing the band splitting. This system is intriguing under various aspects. The low dimensionality, the formation of a 2DHG, the stronger SOC of the Sn with respect to the Ge and the integrability in Si manifacture combined together make this heterostructure a novel playground for spintronics with a variety of parameters that can be tuned and exploited for fundamental research as well as for future applications.

Material	$\Theta_{SH} \times 10^{-4}$	Temperature [K]	Reference
Al	0.4-1	4.2	[69]
Au	35	N/A	[70]
Pt	40-800	300	[67]
Pd	64	N/A	[70]
Ta	2000	300	[68]
GaAs	5-200	300	[62]
Si	1	300	[63]
Ge	2-11	20 - 300	[71, 72]

Table 1: Spin-Hall angle for different materials. The temperature at which the spin-Hall angle is extracted is reported as well.

3 Optical spin orientation

The possibility to optically generate a spin polarized population in semiconductors arises from the light-matter interaction, as a result of the spin-orbit coupling. This phenomenon is a direct consequence of the conservation of angular momentum when circularly polarized light is absorbed by the medium. In this process, the momentum of light is transferred through the SOC to the photogenerated electron and hole pairs which eventually become spin polarized. Pioneer results on optical spin orientation in solids were obtained by Lampel in Si in 1968 [73] and since then the optical orientation has proven itself as a reliable method for studying spin physics in semiconductors. In this whole thesis the core technique exploited for the measurements is the so called optical spin orientation. We describe it in the following.

We define the propagation direction of a circularly polarized light along the z-axis. The projection of angular momentum along the propagation axis is therefore $L_z = \pm\hbar$, where the plus (minus) sign indicates a right (left)-handed helicity. A common convention is to use $\sigma^+(\sigma^-)$ for a right-handed (left-handed) circular polarization. Whenever a photon is absorbed ($E_{phot} \geq E_g$) the SOC allows the transfer of angular momentum to the carrier. This means that for transitions from the VB to the CB the following selection rule must be satisfied:

$$\Delta m = m_{j,f} - m_{j,i} \tag{13}$$

where m_j is the eigenvalue associated to L_z, while f and i refer to the final and initial states of the transition. It is clear that this process is affected by the nature of the bands involved.

For the sake of clarity, we restrict ourselves to the toy model developed for direct bandgap III-V compounds [20]. As shown later, this model works also for Ge at zone centre due to its quasi-direct nature [20].

This toy model uses a tight-binding approach that includes SOC, according to which VB can be described with 3 p-like levels all degenerate because of the

spin (see Fig. 5a). These levels are known as heavy-holes (HH), light-holes (LH) and split-off (SO) states. The CB, on contrary, can be represented as a single degenerate s-like level. All these states are described by the quantum numbers j and m_j in the form of $\left|j, m_j\right\rangle$[3]. A vertical transition between these states is associated to a matrix element $\langle f|\,\hat{p}\,|i\rangle$ where $\hat{p}$ is the dipole moment operator [74]. Here $\hat{p} = -e\bar{\mathbf{r}}$ where e is the electron charge and $\bar{\mathbf{r}}$ is a unit vector along the direction of the observation [13, 74]. The transition probabilities are given by [75]:

$$|\,\langle j+1, m_j+1|\,\sigma^+\,|j, m_j\rangle\,|^2 = \frac{1}{2}\,(j+m_j+1)(j+m_j+2)\,B \tag{14a}$$

$$|\,\langle j, m_j+1|\,\sigma^+\,|j, m_j\rangle\,|^2 = \frac{1}{2}\,(j-m_j)(j+m_j+1)\,A \tag{14b}$$

$$|\,\langle j-1, m_j+1|\,\sigma^+\,|j, m_j\rangle\,|^2 = \frac{1}{2}\,(j-m_j)(j-m_j-1)\,C \tag{14c}$$

$$|\,\langle j+1, m_j-1|\,\sigma^-\,|j, m_j\rangle\,|^2 = \frac{1}{2}\,(j-m_j+1)(j-m_j+2)\,B \tag{14d}$$

$$|\,\langle j, m_j-1|\,\sigma^-\,|j, m_j\rangle\,|^2 = \frac{1}{2}\,(j+m_j)(j-m_j+1)\,A \tag{14e}$$

$$|\,\langle j-1, m_j-1|\,\sigma^-\,|j, m_j\rangle\,|^2 = \frac{1}{2}\,(j+m_j)(j+m_j-1)\,C \tag{14f}$$

where we are using $\bar{\mathbf{r}} = x\,\bar{\mathbf{i}} + y\,\bar{\mathbf{j}} + z\,\bar{\mathbf{k}}$ and $\sigma^{\pm} = (x \pm iy)/\sqrt{2}$. A, B, C are constants defined by:

$$\begin{aligned} A &= \frac{|\,\langle j|\;|p|\;|j\rangle\,|^2}{j(j+1)} \\ B &= \frac{|\,\langle j+1|\;|p|\;|j\rangle\,|^2}{(j+1)(2j+1)} \\ C &= \frac{|\,\langle j-1|\;|p|\;|j\rangle\,|^2}{j(2j+1)} \end{aligned} \tag{15}$$

[3]Quantum numbers j and m_j are associated, respectively, to the total angular momentum operator $\hat{J}$ and to its projection, $\hat{J}_z$, along the light propagation direction.

The ratio between these probabilities dictates the ratio between spin-up ($n_\uparrow$) and spin-down ($n_\downarrow$) population densities that are photogenerated.

Both excitation and recombination processes follow these rules as the conservation of the angular momentum must be satisfied in both processes. In Fig. 5b and c we report all possible transitions involved in the absorption and recombination processes.

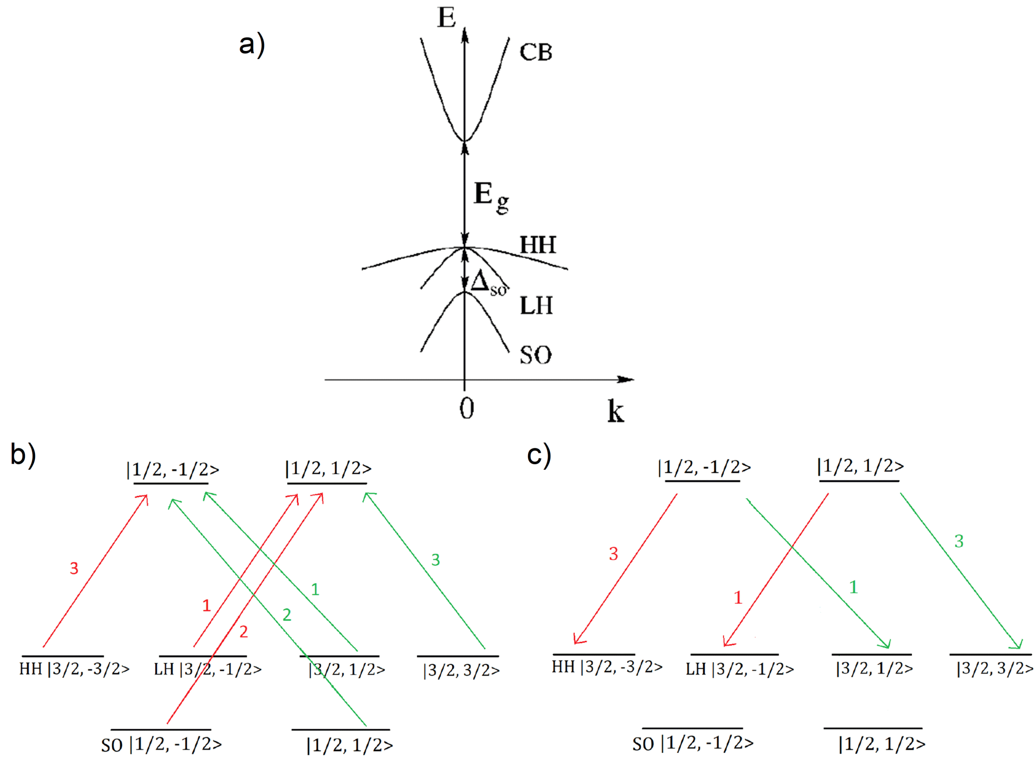

Figure 5: (a) Schematic band structure near the centre of the Brillouin zone, where E_g is the bandgap and Δ_{SO} the spin-orbit splitting; CB, conduction band; HH, heavy hole; LH, light hole; SO, split-off subbands. (b) Schematic representation of VB and CB states involved in the optical orientation and (c) in the optical recombination processes at the Γ point. Red (green) arrows in (b) highlight the allowed transitions upon σ^+ (σ^-) excitation, while in (c) the recombination processes are shown. The oscillator strength of each transition is reported as a number close to the arrows. Adapted from [76].

From now on, we restrict ourselves to the case of a right-handed circularly polarized excitation, therefore only transitions associated to red arrows in Fig. 5b will be considered.

Upon resonant excitation, i.e., $E_{phot} = E_g$, only LH and HH states contribute to the optical orientation since SO states lie at higher energies ($E_{SO} = E_g + \Delta_{SO}$). By evaluating the proper matrix elements, it can be shown that HH transitions have an oscillator strength that is three times bigger than LH ones thereby inducing a $n_\uparrow : n_\downarrow = 1 : 3$ ratio in the electron spin population. Since the average spin polarization of electrons promoted to CB is:

$$S_0 = \frac{n_\uparrow - n_\downarrow}{n_\uparrow + n_\downarrow} = \frac{1-3}{1+3} = -\frac{1}{2} \tag{16}$$

in a bulk material a circularly polarized excitation upon resonant condition can induce a total electron spin polarization of -50 %.

If we include transitions from the SO band, when $E_{phot} > E_g + \Delta_{SO}$, the spin-up and spin-down population densities are now equal ($n_\uparrow = n_\downarrow$), washing out the overall electron polarization. Pierce and Meier [77] in 1976 studied the spin polarization as a function of the energy of illumination in GaAs systems. In their work they exploited optical orientation to generate a spin polarized population. Then they exploited the photoemitted electrons to analyze the polarization via Mott scattering from an Au foil. They found that the electron polarization has a maximum of 40 % when energy of the photoemitted carrier is resonant to Γ transition and decreases to zero as emission from the SO band is mixed in, due to the opposite spin orientation.

The different contribution of each transition to the polarization suggests that by removing the state degeneracy of LH and HH at Γ, for example via quantum confinement or via strain engineering, a higher polarization can be achieved.

Since the optical orientation generates an out-of-equilibrium population, the time evolution of such population also requires to be taken into account. The nonequilibrium spins can eventually decay due to recombination or relaxation

processes. The dynamics is described by the following continuity equation for the average spin expectation value S [13]:

$$\frac{dS}{dt} = -\frac{S}{\tau_s} - \frac{S - S_0}{\tau} \tag{17}$$

where τ_s is the spin relaxation time and τ is the carrier lifetimes, respectively. The first term describes the spin relaxation processes occurring on the timescale of τ_s, while the second is related to the optical recombination and excitation.

In CWPL experiments the system reaches a steady-state situation where an equal number of carriers are generated and recombine. Under this approximation the left-hand side of Eq. 17 is null and a solution can be found as:

$$S = \frac{S_0}{1 + \tau/\tau_s} \tag{18}$$

This implies that whenever the spin lifetime is greater that the carrier lifetime ($\tau_s > \tau$), the recombination process yields circularly polarized emission of light (see Fig. 5c for all the possible transitions and the helicity of the emitted light). Therefore, a proof of the optical orientation in the material is obtained by measuring the helicity of the CWPL, which is quantified as the degree of circular polarization (ρ_{circ}):

$$\rho_{\text{circ}} = \frac{I_{\sigma^+} - I_{\sigma^-}}{I_{\sigma^+} + I_{\sigma^-}} \tag{19}$$

where I_{σ^+} (I_{σ^-}) is the intensity of σ^+ (σ^-) emission.

Due to the strong spin-orbit coupling of holes, the depolarization of holes is much faster than the one of electrons (for example in Ge $\tau_s^{\text{holes}} \sim 1$ ps [51, 52, 78]); therefore only electrons contribute to the polarization of the PL. Following the excitation with $E_{\text{phot}} < E_{\text{SO}}$ in a bulk semiconductor we thus have:

$$\rho_0 = \frac{(n_\uparrow + 3n_\downarrow) - (3n_\uparrow + n_\downarrow)}{(n_\uparrow + 3n_\downarrow) + (3n_\uparrow + n_\downarrow)} = \frac{\left(1 \cdot \frac{1}{4} + 3 \cdot \frac{3}{4}\right) - \left(3 \cdot \frac{1}{4} + 1 \cdot \frac{3}{4}\right)}{\left(1 \cdot \frac{1}{4} + 3 \cdot \frac{3}{4}\right) + \left(3 \cdot \frac{1}{4} + 1 \cdot \frac{3}{4}\right)} = -\frac{1}{4} \tag{20}$$

so that from $S_0 = -1/2$ we end up with an emission that has half the initial polarization, so that $\rho_0 = -1/4$. Eq. 18 becomes eventually:

$$\rho_{\text{circ}} = \frac{\rho_0}{1 + \tau/\tau_s} \tag{21}$$

when the steady-state condition is met.

Since out-of-equilibrium spin populations decay and reach thermodynamic equilibrium, we expect a transient time for which the polarization can be described as $\rho_{\text{circ}}(t) \sim \rho_0\, e^{-t/\tau_s}$. Differently from CWPL, TRPL provides a direct and convenient means to measure the spin relaxation time, offering insights into spin-dependent kinetics under the influence of different factors like lattice temperature, doping level and external fields.

It is important to recall that the toy model described above is valid only for centre-zone states because it does not consider the inherently mixed orbital character of the wavefunctions of carriers having nonzero momentum. We highlight that a comprehensive theory of spin-dependent optical transitions for edge states are presented in Ref. [79]. In that work, symmetries of wave functions and interactions are used to derive ratios between intensities of the right and left circularly polarized luminescence for each of the dominant phonon-assisted optical transitions.

In this thesis optical investigation has been selected for the study of spin physics. However, it is worth noticing that there exist various techniques, based for example on electrical measurements, that have been shown in literature to be a reliable approach towards the unveiling of spin-related phenomena [80].

4 Hanle effect

The application of a magnetic field along an axis different from the spin quantization axis induces a Larmor precession of the spin. This effect is maximum when the magnetic field and the spin quantization axis are perpendicular to each other. In this configuration, known as Voigt configuration, the time evolution of **S** is:

$$\frac{\partial \mathbf{S}}{\partial t} = \begin{pmatrix} \Omega_x \\ \Omega_y \\ \Omega_z \end{pmatrix} \times \begin{pmatrix} S_x \\ S_y \\ S_z \end{pmatrix} - \begin{pmatrix} \frac{S_x}{T_2} \\ \frac{S_y}{T_2} \\ \frac{S_z - S_{0z}}{\tau_s} \end{pmatrix} \tag{22}$$

where $\Omega_i = g\mu_b B_i/\hbar$ is the precession frequency, g is the electron Landé factor, μ_b the Bohr magneton. The spin relaxation time τ_s can be interpreted as the time required for the spin along the longitudinal field to reach equilibrium, in literature it is commonly referred to also as spin-lattice time or T_1. On the other hand, T_2 is the spin decoherence or spin dephasing time and is defined as the time required for transverse spins, initially precessing in phase about a longitudinal field, to lose their phase. This measures the decoherence time of the spin ensemble and takes into account inhomogeneous broadening effect of the precessing frequencies [81].

Under continuous illumination, the spin precession, together with the random character of carrier generation or diffusion, leads to the spin relaxation. This phenomenon is known as Hanle effect [82]. To obtain the dependence of **S** as a function of the magnetic field we can solve Eq. 22 where an additional term (**S** / τ) is introduced to take into account for carrier recombination:

$$\frac{d\mathbf{S}}{dt} = \Omega \times \mathbf{S} - \frac{\mathbf{S}}{\tau} - \frac{\mathbf{S} - \mathbf{S}_0}{\tau_s} \tag{23}$$

The solution is:

$$\mathbf{S}(B) = \frac{\mathbf{S}(B=0)}{1+(\Omega T_S)^2} \tag{24}$$

where T_S is the spin lifetime, defined as:

$$\frac{1}{T_S} = \frac{1}{\tau_s} + \frac{1}{\tau} \tag{25}$$

The overall effect of the precession is to reduce the projection of the spin along the observation direction leading to a spin depolarization. This translates into a reduction of the PL polarization that now assumes a form similar to Eq. 24:

$$\rho_{\text{circ}}(B) = \frac{\rho_{\text{circ}}(B=0)}{1+(\Omega T_S)^2} \tag{26}$$

This last expression means that the Hanle effect provides a method to determine the spin lifetime from CWPL measurements, without the requirement of a time-resolved apparatus. By measuring the full width at half maximum (ΔB) of the curve we obtain:

$$\Delta B = 2\frac{\hbar}{g\mu_B T_S} \tag{27}$$

therefore the spin lifetime can be extracted by inverting Eq. 27.

The Hanle effect has already been exploited in the field of III-V compounds, where electrical as well as optical detection were implemented over the last 50 years [83–86], whereas for group IV materials the study of the Hanle effect by means of optical techniques has been so far overlooked in group IV semiconductors due to the indirect bandgap nature.

In this thesis we have exploited for the first time the Hanle effect to study the spin dynamics of $Ge_{1-x}Sn_x$ alloys (see Ch. 10).

5 Spin-relaxation mechanisms

Spin polarized carriers do not retain their initial spin orientation once injected into a semiconductor. Indeed, spin relaxation mechanisms perturb the spin orientation of the population and tend to restore an equilibrium condition. The strength of each spin relaxation mechanism varies from semiconductor to semiconductor as well as with temperature. It may also depend on the quality of the materials or the doping level. Therefore, it is critical that the dominant spin relaxation mechanism is known before designing spintronics devices. Four major mechanisms can be identified: Elliott-Yafet (EY), Dyakonov-Perel (DP), Bir-Aronov-Pikus (BAP) and hyperfine interaction.

5.1 Elliott-Yafet mechanism

Intuitively, this process stems from the interplay between momentum relaxation and lattice-induced spin-orbit coupling [87, 88]. The electron wave function Ψ is hardly in a pure spin eigenstate but rather composed of a spin-up $|\uparrow\rangle$ and spin-down $|\downarrow\rangle$ mixture, so that:

$$\Psi_{\mathbf{k},n_\uparrow}(\mathbf{r}) = [a_{\mathbf{k},n}(\mathbf{r})\,|\uparrow\rangle + b_{\mathbf{k},n}(\mathbf{r})\,|\downarrow\rangle]\,e^{i\mathbf{kr}} \tag{28}$$

$$\Psi_{\mathbf{k},n_\downarrow}(\mathbf{r}) = [a^*_{-\mathbf{k},n}(\mathbf{r})\,|\downarrow\rangle - b^*_{-\mathbf{k},n}(\mathbf{r})\,|\uparrow\rangle]\,e^{-i\mathbf{kr}} \tag{29}$$

where a and b are complex lattice coefficients, **k** is the lattice momentum and n the band index.

The spin relaxation time for Elliott-Yafet (EY) mechanism is given by [89]:

$$\frac{1}{\tau_s} \simeq \left(\frac{\Delta_{\mathrm{SO}}}{\mathrm{E_g} + \Delta_{\mathrm{SO}}}\right)^2 \left(\frac{\mathrm{E_k}}{\mathrm{E_g}}\right)^2 \frac{1}{\tau_p} \tag{30}$$

where $\mathrm{E_k}$ is the kinetic energy of the carrier and τ_p is the time between two scattering events. It is clear from Eq. 30 that this mechanism is important for small bandgap semiconductors with strong spin-orbit splitting [87, 88]. Scatter-

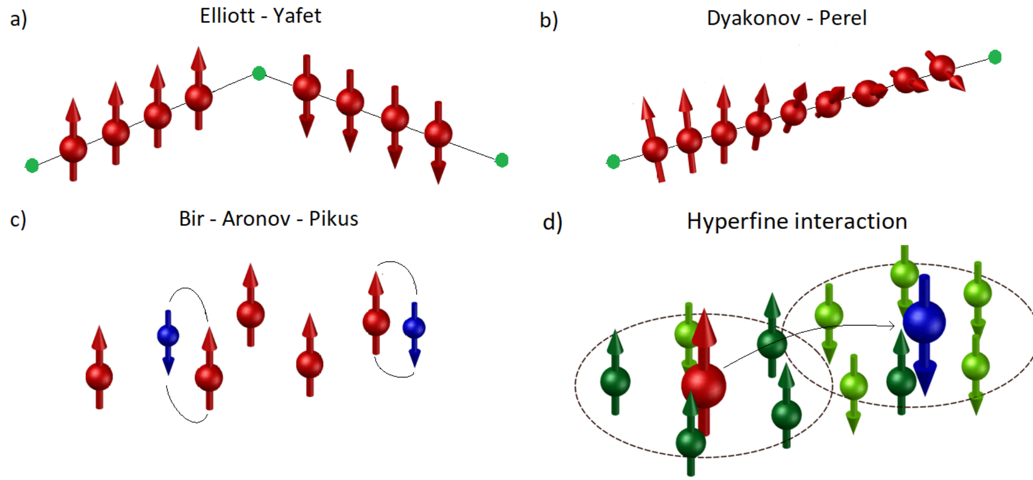

Figure 6: (a) Schematic representation of EY mechanism where the electron (red spheres) interacts with the scattering centre (green dots) and the renormalization of the carrier wavefunction during the scattering event causes a change in the spin polarization [11, 54]. (b) The DP mechanism is caused by the precession of the spin around a randomly-oriented local magnetic field, which causes the loss of the original spin orientation. Unlike EY, the DP mechanism occurs between two scattering events [11, 54]. (c) The BAP mechanism occurs when electrons and holes (blue spheres) have their wavefunctions overlapping. The exchange interaction swaps the spin of the two carriers causing a consequent loss of polarization. Here the interacting couple is highlighted using black curved lines. (d) If electrons wave functions are confined over a region (dashed circles) with many nuclear spins (light and dark green spheres), the hyperfine interaction couples electron and nuclear spins, causing spin relaxation [11, 54].

ing events with phonons (high temperatures) or impurities (low temperatures) also contribute to this mechanism as they result in the renormalization of the wavefunction and eventually in a spin-flip, see Fig. 6a. In the case of scattering with phonons, the electron spin relaxation time becomes proportional to the inverse frequency of a typical thermal phonon, thus weakening at low temperatures [11, 54]. Dislocations density plays an important role as a higher number of dislocations causes scatterings to occur more frequently, thus shortening the spin relaxation time [11, 89].

About 10^5 scattering events are commonly needed before the carrier loses its initial spin orientation [11] and, obviously, the faster the momentum scattering rate, the faster the occurrence of spin flip events. This mechanism is found to be significant for all our devices, as shown in Chs. 9 and 10, when the temperature of the device is increased.

5.2 D'yakonov-Perel mechanism

Bulk inversion asymmetry is the cause of the DP mechanism, that is the main depolarization in III-V compounds as well as in $Si_{1-x}Ge_x$, $Ge_{1-x}Sn_x$, $Si_{1-x-y}Ge_xSn_y$ alloys [49]. The lifting of the degeneracy of the spin sublevels can be regarded, from the point of view of the individual spin-polarized electron, as an effective k-dependent magnetic field B(**k**) around which the spin rotates. During the diffusion, the electron experiences a magnetic field varying both in intensity and direction. The spin precession around this randomly changing field results in a loss of polarization. For a given momentum **p**, $\Omega(\mathbf{p})$ is the spin precession frequency in this field. The effective magnetic field changes in time because the direction of **p** varies due to electron collisions. Thus the correlation time is on the order of the time between subsequent collisions and is described by [13]:

$$1/\tau_s = \Omega^2 \tau_p \tag{31}$$

Unlike the EY mechanism, where spin relaxes during the momentum scattering event, the DP mechanism causes spin to relax between two momentum scattering events, see Fig. 6b. Due to this feature, the major difference between EY and DP mechanism is in their dependence on the electron momentum scattering rate. In particular, a faster momentum scattering rate strengthens the effectiveness of the EY process while it suppresses the DP mechanism.

5.3 Bir-Aronov-Pikus mechanism

An additional spin relaxation mechanism originates from the electron-hole exchange interaction, namely the BAP mechanism [90]. This interaction becomes relevant when electron and hole wavefunctions overlap, thus making confined system, doped materials and high injection regimes the suitable conditions for observing it. The exchange interaction between the wavefunctions allows the exchange of spin between the carriers leading to an overall electron depolarization, see Fig. 6c for reference. This effect was found to be significant in Ge/$Si_{1-x}Ge_x$ QWs (see Ref. [91]) where high optical pumping excitation and quantum confinement create the proper conditions for the BAP mechanism to arise. In this work we find out that the BAP mechanism is sizeable also in $Ge_{1-x}Sn_x$/Ge QW (see Ch. 10.2). In the low temperature regime the BAP mechanism is most likely dominating in heavily p-doped materials, whereas when temperature rises it loses relevance in favour of the DP mechanism independently of the doping due to the increased importance of DP for large electron energies [11, 90].

5.4 Hyperfine interaction

Electron and nuclear spins can couple each other via hyperfine interaction. Therefore non-null nuclear spin isotopes introduce an additional source of spin relaxation. In comparison with III-V compounds, Si and Ge possess a lower fraction of spin-bearing isotopes and refinement process can be performed to reduce even further their presence, improving significantly the spin-coherence lifetime. Hyperfine interaction becomes an important mechanism when electrons are localized in confined structures, such as in quantum dots. In these systems, the electron wave function is possibly spread over a region containing non-null nuclear spins, ultimately causing spin relaxation (see Fig. 6d). In our samples the contribution from the hyperfine interaction is considered to be negligible as no investigation is carried out in quantum dot systems.

6 Materials: Si, Ge, Sn and their alloys

In this chapter we describe the structural and electronic properties of the group IV materials that are of relevance for this thesis. In particular we treat Si, Ge, Sn and their alloys.

6.1 Structural properties

Si, Ge and α-Sn, the cubic-like allotrope of tin, are group IV materials that exhibit the diamond crystalline structure, which consists of two interpenetrating face-centred cubic Bravais lattices displaced along the diagonal of the cubic cell by one quarter of the length of the same diagonal. The unit cell contains eight atoms, each bounded to four nearest neighbour forming a tetrahedron, as shown in Fig. 7a.

At room temperature (RT) the lattice constant of these elements are a_{Si} = 0.54310 nm [92], a_{Ge} = 0.56575 nm [92] and $a_{\alpha-Sn}$ = 0.64892 nm [31] for Si, Ge and α-Sn, respectively.

From the point of view of applications, the additional degree of freedom offered by alloying is a desirable feature that brings in new possibilities. The structural properties of an alloy, like the lattice parameter, as well as its electronic properties, such as band structure or the SOC, acquire an intermediate character that can be tuned by changing the materials molar fraction, thus generating intriguing new physics. With this in mind, in this thesis we investigate the properties of two alloys: $Si_{1-x}Ge_x$ and $Ge_{1-x}Sn_x$.

A complete solubility exists between Si and Ge in liquid and solid state as shown in the equilibrium phase diagram in Fig. 8. At room temperature the two elements form a stable continuous series of solid solutions which crystallize in the diamond-like lattice with gradually varying properties.

The lattice constant ($a_{Si_{1-x}Ge_x}$) follows an almost linear behaviour from the one of Si to the one of Ge. The crystalline structure of $Si_{1-x}Ge_x$ remains diamond-like in the whole composition range. Dismukes et al. [94] carried out a comprehensive

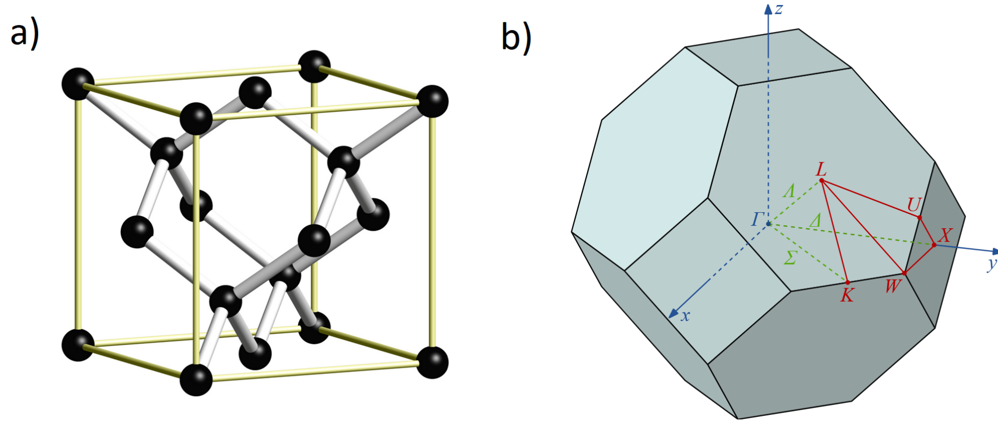

Figure 7: (a) Diamond-like crystal structure. (b) First Brillouin zone of a face-centered cubic cell reporting the high symmetry points of the reciprocal lattice. K is located in the middle of an edge joining two hexagonal faces, L is the centre of a hexagonal face, U is in the middle of an edge joining a hexagonal and a square face, W is a corner point while X is the centre of a squared face.

determination of the $Si_{1-x}Ge_x$ lattice constants and observed a small deviation from linearity. By using the values given in [95], a second order polynomial law as a function of the Ge molar fraction (x) has been suggested [95–97]:

$$a_{\mathrm{Si_{1-x}Ge_x}} = 0.5431 + 0.01992\,\mathrm{x} - 0.002733\,\mathrm{x}^2 \quad [nm] \tag{32}$$

In Fig. 9a we show the $Si_{1-x}Ge_x$ lattice constant according to Eq. 32.

At a variance from the $Si_{1-x}Ge_x$ case, obtaining $Ge_{1-x}Sn_x$ binary alloys has been a task that only in the last decade has found successful solutions. The large lattice mismatch between Ge and Sn, induces the nucleation of defects during the growth more easily than for the $Si_{1-x}Ge_x$ alloy. Additionally, the low equilibrium solubility of the two elements limits the fraction of Sn that can be incorporated at a maximum value of 1.1 % [31], yielding Sn clusterization and surface segregation. The Ge-Sn equilibrium phase diagram, shown in Fig. 10, is dominated by two-phase mixtures, namely, (Ge)+L (solid $Ge_{1-x}Sn_x$ with $x < 0.01$ and liquid β-Sn) and (Ge)+(β-Sn) (solid $Ge_{1-x}Sn_x$ with $x < 0.01$ and solid β-Sn) above and below

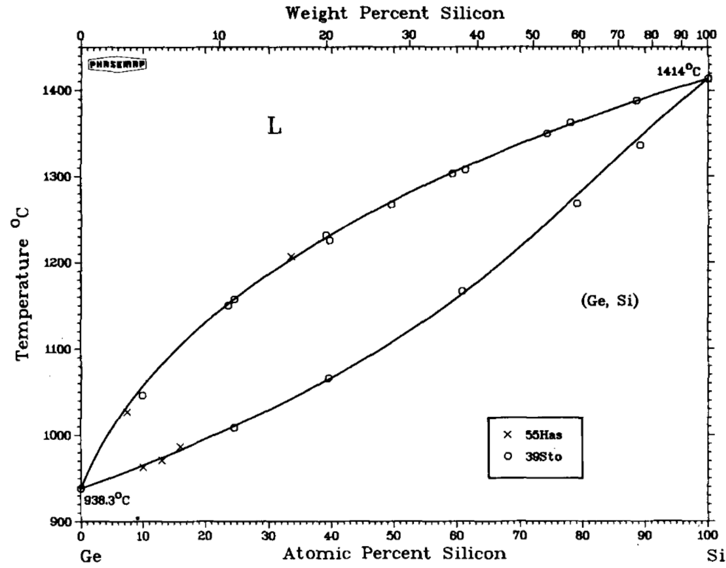

Figure 8: Phase diagram of $Si_{1-x}Ge_x$ at equilibrium [93]

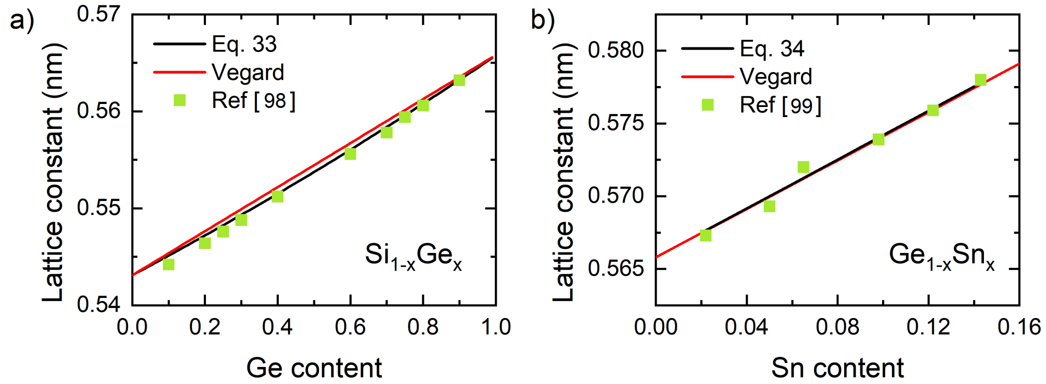

Figure 9: Lattice constant of (a) $Si_{1-x}Ge_x$ as a function of Ge content [94]; green squares represent experimental data [98]. Lattice constant of (b) $Ge_{1-x}Sn_x$ alloy as a function of Sn; green squares represent experimental data [99]. All data are obtained at room temperature.

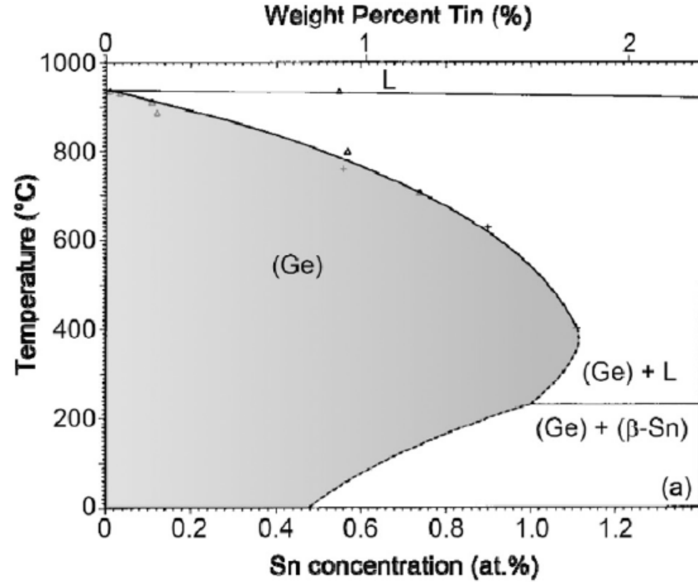

Figure 10: Phase diagram of $Ge_{1-x}Sn_x$ at equilibrium [100]. (Ge) indicates the solid diamond-like phase of $Ge_{1-x}Sn_x$, (Ge) + L indicates solid $Ge_{1-x}Sn_x$ with liquid β-Sn and (Ge) + (β-Sn) indicates solid $Ge_{1-x}Sn_x$ and solid β-Sn.

the melting temperature of Sn (231.1 °C), respectively [31, 100].

Due to these challenges in the synthesis of bulk ingots, great efforts have been put into the development of a reliable epitaxy of this alloy. Only recent advances in out-of-equilibrium crystal growth techniques have yielded epitaxial stabilization of $Ge_{1-x}Sn_x$ films with a good crystal quality and a Sn content grater than 1 % [31, 101, 102]. The first commercially suitable CVD process for the growth of $Ge_{1-x}Sn_x$ materials was published by Taraci et al. in 2001 [103]. However, high-quality epitaxial films with a Sn fraction up to 8 % were reported only in 2011 from the group of IMEC (Vincent et al. [104]).

Due to the difficult conditions required for the growth, only few data are available for the determination of the lattice parameter. Within the range so far studied, that is shown in Fig. 9b, the lattice parameter ($a_{Ge_{1-x}Sn_x}$) can be described by [99]:

$$a_{Ge_{1-x}Sn_x} = 0.56575 + 0.08405\,x + 0.00088\,x^2 \quad [nm] \tag{33}$$

6.1.1 Heteroepitaxy and strain

The heteroepitaxial growth is the deposition of a layer on a crystalline substrate that is made of a different material. This allows for a well-controlled transition from one material to another within a single crystalline solid [105]. The deposition process is affected by the mutual interaction between substrate and the epitaxial layer [106, 107] and so are the resulting crystal quality and properties. Whenever the lattice constants of the two layers are not identical, a lattice mismatch (f) is imparted to the epitaxial film:

$$f = \frac{a_0 - a_s}{a_0} \tag{34}$$

where a_0 and a_s are the lattice constants of the top layer and of the substrate, respectively. Despite the different lattice constants, it can happen that the deposited material matches the substrate lattice in the so called pseudomorphic growth. In that case, the epilayer lattice parameter in the growth plane $a_{\|}$ is the one of the substrate a_s, giving rise to an in plane strain equal to the misfit f. In this condition, two possibilities can occur: the top layer is under a compressive (if $a_0 > a_s$) or a tensile (if $a_0 < a_s$) strain. In both situations the strain is in the xy-plane of the layer ($\epsilon_{xx} = \epsilon_{yy} = \epsilon_{\|}$), where we choose a reference system with z along the growth direction and x and y two in-plane orthogonal directions. The deformation of the lattice in the xy plane does not leave the lattice unperturbed in the perpendicular direction. As predicted by the elastic theory, for small distortions a perpendicular strain ($\epsilon_{\perp}$) is indeed generated [97]:

$$\epsilon_{\perp} = \epsilon_{zz} = -2\frac{C_{12}}{C_{11}}\epsilon_{\|} \tag{35}$$

where C_{11} and C_{12} are the stiffness constants. A schematic representation of pseudomorphic growth with the top layer compressive or tensile strained is reported in Figs. 11a-d.

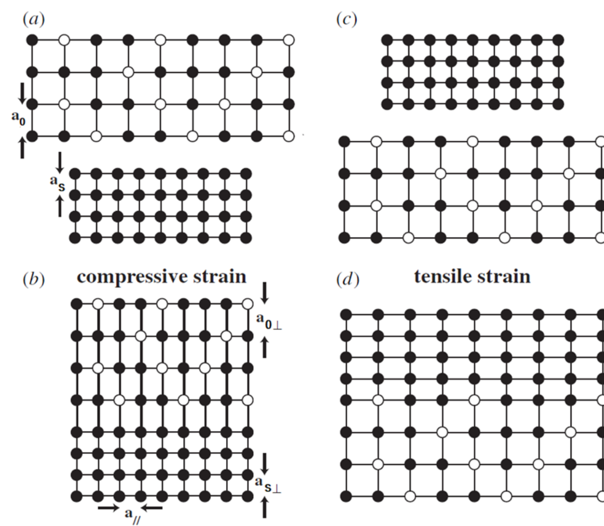

Figure 11: (a) Sketch of the bulk lattice parameter (a_0) of a thin film of material A to be grown on top of bulk material B with bulk lattice parameter a_s, here $a_0 > a_s$ [97]. (b) Sketch showing the tetragonal lattice distortion when the two films from (a) are joined. The top film A is under compressive strain. (c) Sketch diagram of the situation described in (a) when $a_0 < a_s$. (d) Schematics of the two films in (c) joined together with the top film under tensile strained [97].

6.2 Electronic properties

Si is the most studied group IV material. It possesses an indirect bandgap with the top of the VB located at the centre of the first Brillouin (FB) zone (Γ-point). For Si, the CB absolute minimum lies at 1.12 eV from the top of the VB and is located at about 0.85 from the zone boundary along the Δ-direction. The first Γ state is found higher in energy, i.e., at 3.4 eV from the VB [108].

Ge is another indirect bandgap semiconductor whose band structure is reported in Fig. 12b. Its VB maximum at the Γ-point is degenerate and consists of HH and LH states, while the SO band lies 290 meV below the top of the VB [108]. The CB absolute minimum is located at the L-point at ~0.660 eV above the top of the VB and it possesses a fourfold degeneracy. The remaining CB minima are found at Γ and X points and are higher in energy by about 136 meV and 200 meV with respect to the L-point absolute minima, respectively [109]. The close proximity of the direct and indirect transitions make Ge a quasidirect semiconductor.

Sn lies a row below the Ge in the periodic table. It undergoes a phase transition from its α-Sn phase with diamond cubic lattice structure to a metallic phase (β-Sn) with a body-centered tetragonal structure. This transition occurs at 13.2°C [98] and leads to a volume change of approximately 26% [110]. Interestingly, Sn possesses a peculiar band structure that results in a gapless material [111, 112]. In particular, the Groves–Paul model (GP) [113] describes α-Sn as a semi-metal with overlap between the conduction and valence band, which lead to a negative bandgap of -0.41 eV [31, 113].

It has been reported that α-Sn shows an inversion of the CB and VB bands at zone centre, due to the negative bandgap [33, 114, 115]. This effect causes α-Sn to show topological insulating properties in thin epilayer, opening new fascinating possibilities [116–118].

By comparing results shown in Figs. 12a-c, Δ_{SO} increases from Si (44 meV) to Ge (290 meV) to Sn (> 600 meV [33]). Considering the nature of the SO band, a greater separation is a direct consequence of the stronger SOC of Sn with respect

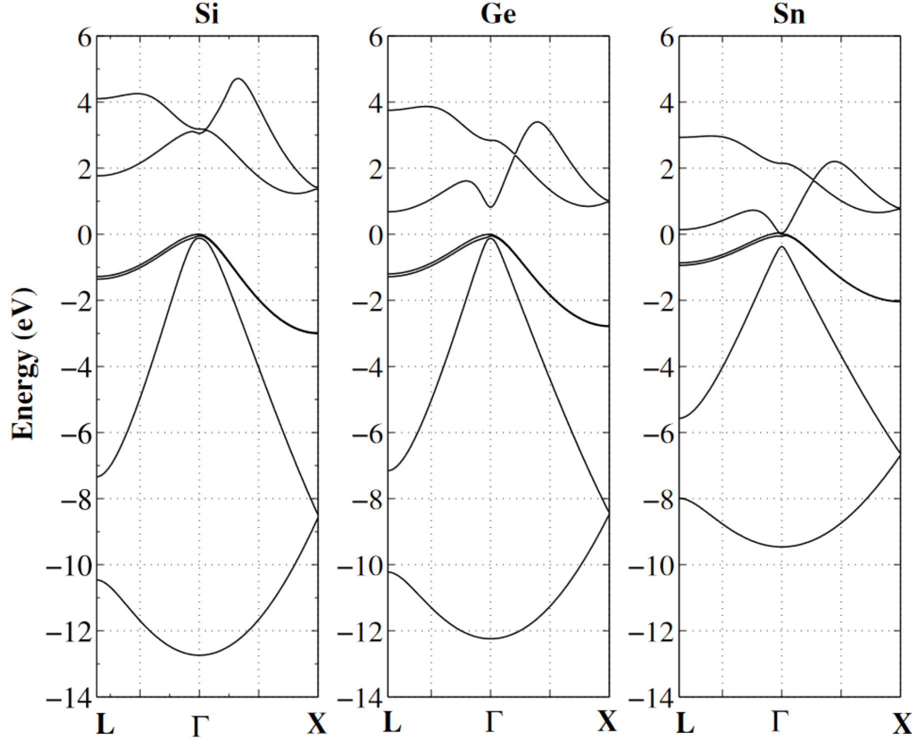

Figure 12: Calculated band structures of Si, Ge and α-Sn at room temperature with a self-consistent pseudopotential method [119].

to both Ge and Si, which can be ultimately ascribed to its higher atomic number.

Like Si and Ge, $Si_{1-x}Ge_x$ is an indirect bandgap semiconductor. The top of the VB lies always at the zone centre, however the location of the CB minimum changes from the Δ valleys at Ge molar fraction $x < 0.85$ (Si-like character) to the L valleys (Ge-like character) for $x \geq 0.85$ [120]. In Figs. 13a and b we report the indirect and direct excitonic bangap as a function of the Ge content of the alloy [120]. The behaviour can be described by the following equations (expressed in eV) [120]:

$$E_{direct} = 4.185 - 3.296\,x \tag{36}$$

$$E_{indirect} = \begin{cases} 1.155 - 0.43\,x + 0.206\,x^2 & if\ x < 0.85 \\ 2.010 - 1.27\,x & if\ x \geq 0.85 \end{cases} \tag{37}$$

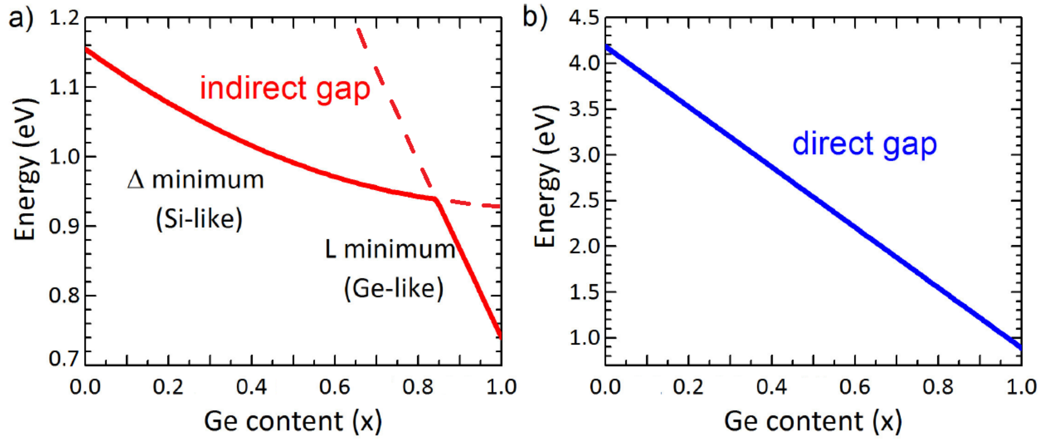

Figure 13: (a) Indirect and (b) direct bandgap in $Si_{1-x}Ge_x$ alloys [120].

The kink that is visible along the straight line of Fig. 13a originates only from the change in the character of the minimum. No change in the crystalline structure is found at that composition since the diamond-like structure holds for the entire composition range.

The increasing of the SOC with the atomic mass can be exploited to engineer spin-dependent phenomena. For instance, by alloying Sn with Ge we expect to have an effective degree of freedom to further enrich the already interesting spin physics of Ge. Furthermore, $Ge_{1-x}Sn_x$ are appealing materials thanks to the tunable bandgap that lies in the short-wavelength infrared range, a technologically useful window for various applications such as environmental- and bio-sensing [121, 122].

One of the most appealing properties that characterize this alloy is the predicted transition from indirect to direct bandgap [32, 33, 123, 124]. Over the years, the calculations restricted the Sn concentration required for the transition within the range of 6-11 % [32, 123, 124] for the case of unstrained $Ge_{1-x}Sn_x$.

The direct bandgap nature could enable the realization of efficient emitting devices for optoelectronics on Si, which are so far limited by the inefficient second order recombination processes of the indirect nature of elemental group IV ma-

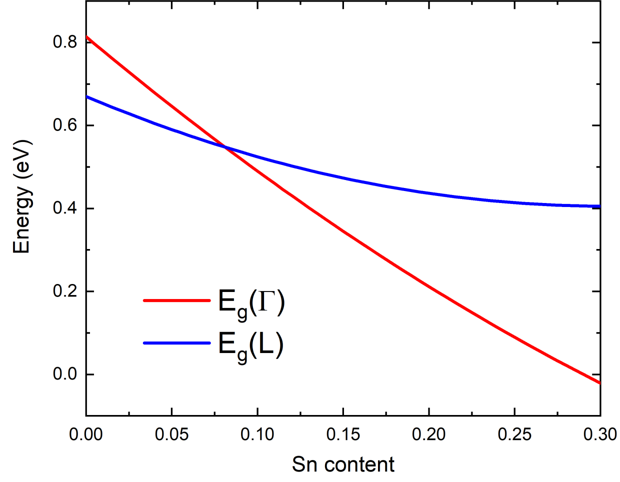

Figure 14: Bandgap dependence of $Ge_{1-x}Sn_x$ as a function of the Sn composition x at room temperature is presented as solid lines for the Γ point (red) and L valley (blue) [33]. The curves are obtained from Eq. 38.

terials. Only in 2015 PL measurements and optically stimulated lasing action on partially relaxed $Ge_{1-x}Sn_x$ samples with $0.08 \leq x \leq 0.126$ grown on Ge-buffered Si (001) substrates provided indeed a compelling experimental demonstration of a true indirect-to-direct crossover [34].

Recently, lasing [125, 126] and competitive photodetection efficiencies [127, 128] have been demonstrated for various $Ge_{1-x}Sn_x$-based devices, moving forward the integration of optical devices into the well-established Si-based technology.

The Γ and L bandgap dependence with Sn composition has been described by a 30-bands **k·p** method adopted by Song et al. [33]:

$$\begin{cases} E_g(\Gamma) & = 0.814 - 3.467\,x + 2.277\,x^2 \\ E_g(L) & = 0.670 - 1.74\,x + 2.862\,x^2 \end{cases} \tag{38}$$

In Fig. 14 we have reported the curves described by Eq. 38 showing the Γ-L crossover [33].

7 Heterostructures

In this thesis we focus on quantum wells since this two-dimensional system offers a way to investigate the Rashba physics emerging in group IV heterostructures. Here we provide some basic descriptions of QW and we introduce some notable properties that are inherent to low-dimensionality structures.

7.1 Band alignment

A fundamental property offered by the realization of heterostructures is the opportunity to manipulate the behaviour of electrons and holes through band engineering. Within the band engineering, a core problem consists in the way in which the CB and the VB of the barrier and well align with respect to each other.

Consider a heterojunction between two materials A and B, with $E_g^A < E_g^B$. The simplest theory to describe the how the band structure align at the interface between material A and B is given by the Anderson's rule [129]. This is based on the electron affinity χ of the materials, the energy required to take an electron from the bottom of the conduction band E_c to the vacuum level where it can escape from the crystal. Anderson's rule states that the vacuum level of the two materials of a heterojunction should be lined up, as in Fig. 15. This shows immediately that $\Delta E_c = E_c^B - E_v^A = \chi^A - \chi^B$. Although it is easy to measure the difference in band gap, it is much more difficult to find out the correct positioning of the individual bands [129]. Nevertheless, three possible configurations can occur:

- Type-I: the narrower bandgap is completely enclosed within the wider bandgap as shown in Fig. 16a. In this condition both electrons and holes are confined within the same region. From an optical point of view the confinement significantly increases the overlap of the electron-hole wavefunctions. This causes a higher recombination efficiency with respect to bulk system as well as type-II alignment [130];

- Type-II: this situation is well described in Fig. 16b. Here only one type or

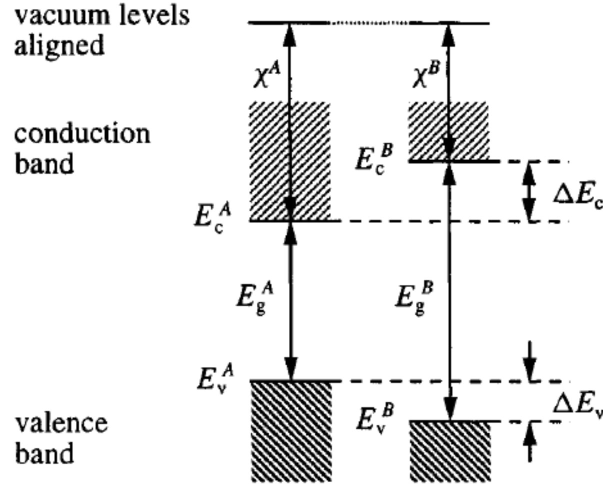

Figure 15: Schematic representation of the alignment of the bands at a heterojunction between materials A and B following the Anderson's rule, based on the alignment of the vacuum levels [129]. χ^A and χ^B are the electron affinities of the materials A and B, respectively, while ΔE_c (ΔE_v) is the difference between the minimum (maximum) of the CB (VB) in the two materials.

carrier is confined in one material and the other is energetically favoured to end up in the other one. It is clear that in this case the overlap of the electron-hole wavefunctions is reduced with respect to previous case with a consequently reduced recombination efficiency;

- Type-III: in this case the CB of one material overlaps with the VB of the other, as illustrated in Fig. 12c. Electrons and holes therefore can transfer freely from VB to CB [129].

The electronic properties of $Si_{1-x}Ge_x/Si_{1-y}Ge_y$ for any x and y Ge concentrations are thoroughly discussed in various reviews and their results are reported in Figs. 17a and b [97, 131–134]. In particular, Reference [131] provides a complete description of VB and CB band alignments. By changing the x and the y Ge compositions (see Fig. 17b) we can distinguish four regions. In region (i) and (iv) the band alignment results in a type-II, in region (iii) the band alignment belongs to

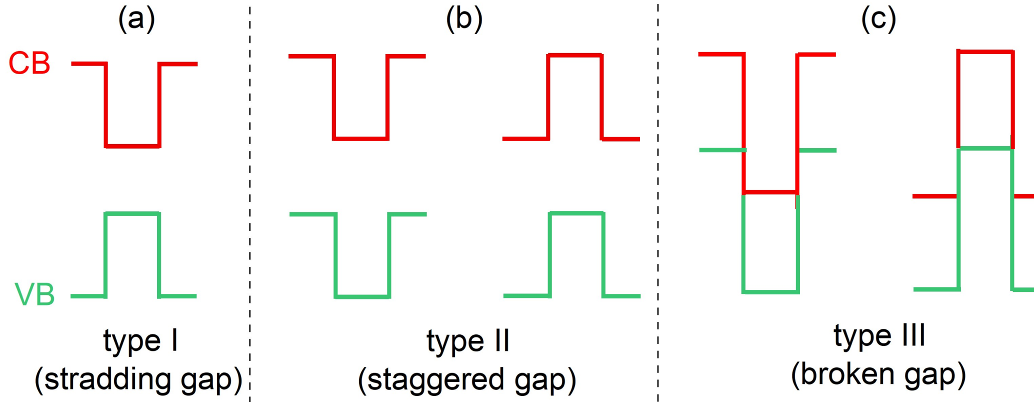

Figure 16: Pictorial representation of (a) type-I, (b) type-II and (c) type-III band alignments in heterostructures.

type-I and finally in region (ii) no confinement is expected in the well.

Since type-I is suitable for optoelectronic application, as already pointed out before, various experimental works investigated the electronic/optical properties of this system [135–138]. Likewise, our investigation is carried out on Ge QWs embedded in Ge-rich (85 %) $Si_{1-x}Ge_x$ barriers. This ensures that the devices fall in region (iii) of Fig. 17b, where a type-I alignment is present. Thus, we can exploit the positive effects on the optical recombination process offered by this type of carrier confinement.

On the other hand, the nature of the band lineups in $Ge_{1-x}Sn_x$/Ge heterojunctions is still facing open questions. Different works agree on a type-I alignment for at the zone centre for a Sn content up to 9 % in $Ge_{1-x}Sn_x$/Ge junctions [139–143].

A significant difference is found when considering the L states of the QW. In particular, the results of the calculations presented in Refs. [139, 141, 142] predict a type-I alignment for the Ge band edge states and the confining potential changes depending on the Sn content and the strain level. For example, in Ref. [142] for pseudomorphic (1.3 % compressive strain) $Ge_{0.92}Sn_{0.08}$/Ge QW they calculated a confining potential for L states of approximately 150 meV while in Ref. [139]

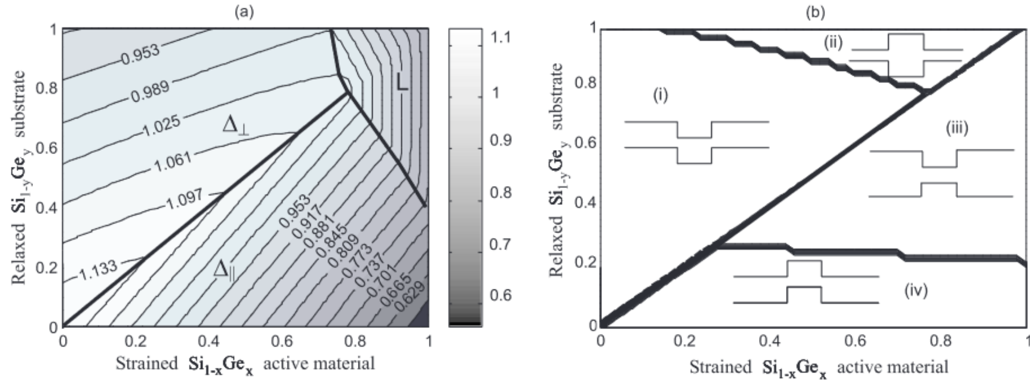

Figure 17: (a) Calculated bandgap for different Ge concentration (x and y values) of a $Si_{1-x}Ge_x$ layer grown on (001)-oriented $Si_{1-y}Ge_y$ buffer. (b) Band profiles showing four regions with different band alignment. Energies are in eV. Adapted from Ref. [131].

for pseudomorphic (0.6 % compressive) $Ge_{0.95}Sn_{0.05}$/Ge QW they found a much shallower confinement of approximately 10 meV; moreover in Ref. [141] for unstrained $Ge_{1-x}Sn_x$/Ge QW the potential was found to be approximately 50 meV at Sn content of 5 as well as 12.6 % and reducing to approximately 20 meV when the 12.6 % QW was fully compressively strained. On the other hand, for similar values of strain and Sn content there are literature results that suggest a type-II alignment [143]. This uncertainty can be ascribed to the parameters used in the various simulations; notably there are no experimental confirmations to corroborate any of the proposed alignments for the L-states. A complete knowledge of these states is important both for the obtaining reliable simulations of the band structure as well as for developing a proper description of carrier dynamics to determine electrical and optical properties of this compound. Our results, presented in Ch. 10.2, provide an experimental evidence supported by a theoretical description that suggest the achievement of a type-II band alignment in fully strained (~ 1 %) $Ge_{0.91}Sn_{0.09}$/Ge QW.

7.2 Strain effects on energy band

The band structure is greatly affected by the strain introduced in the epitaxial layer. All the investigated samples in this thesis are under strain. For our p-i-n diode the stack of 50 Ge/$Si_{0.15}Ge_{0.85}$ QW adapts its lattice constant to underneath $Si_{0.10}Ge_{0.90}$ substrate resulting in a compressively strained well and a tensile strained barriers. This condition is suitably chosen so that the average lattice constant of the whole well-barrier stack matches that of the substrate reducing the overall strain and allowing for the growth of a 2-μm-thick region with a good optical quality.

Likewise, for our $Ge_{0.91}Sn_{0.09}$/Ge QW the well layer adapts to the barrier lattice, resulting in compressively strained layers due to the pseudomorphic growth.

The strain description used so far can be manipulated and rewritten in a such a way that the total strain is decoupled into two components [144]: the hydrostatic strain (ϵ_{hyd}), corresponding to the fractional volume change, and the uniaxial strain (ϵ_{uni}). We obtain:

$$\epsilon_{\mathrm{hyd}} = \epsilon_{\mathrm{hh}} + \epsilon_{\mathrm{kk}} + \epsilon_{\mathrm{zz}} \tag{39}$$

$$\epsilon_{\mathrm{uni}} = \epsilon_{\perp} - \epsilon_{\parallel} \tag{40}$$

This representation turns out to be useful when describing the optical properties such as bandgaps, electronic level shifts and energy level splitting. In general the hydrostatic strain affects the position of the band, shifting it to higher or lower energy. The uniaxial strain typically removes the degeneracy between HH and LH, giving rise to two subbands that are separated in energy. In Fig. 18 we illustrate a typical behaviour of these two strain components on energy level.

The evolution of direct ($\mathrm{E}_{\Gamma}^{\mathrm{s}}$) and indirect ($\mathrm{E}_{\mathrm{L}}^{\mathrm{s}}$) gap energy for a strained group IV material can be described by the following formulas [34, 147, 148]:

$$\mathrm{E^s}_{\Gamma} = \mathrm{E^u}_{\Gamma} + (a_C^{\Gamma} - a_V)(2\epsilon_{\parallel} + \epsilon_{\perp}) + b_s(\epsilon_{\perp} - \epsilon_{\parallel}) \tag{41}$$

$$\mathrm{E^s}_{\mathrm{L}} = \mathrm{E^u}_{\mathrm{L}} + (a_C^{\mathrm{L}} - a_V)(2\epsilon_{\parallel} + \epsilon_{\perp}) + b_s(\epsilon_{\perp} - \epsilon_{\parallel}) \tag{42}$$

where $\mathrm{E^u}_{\Gamma}$ and $\mathrm{E}_{\mathrm{L}}^{\mathrm{u}}$ are the energy gap of the unstrained materials, $a_C^{\Gamma,\mathrm{L}}$, a_V are the

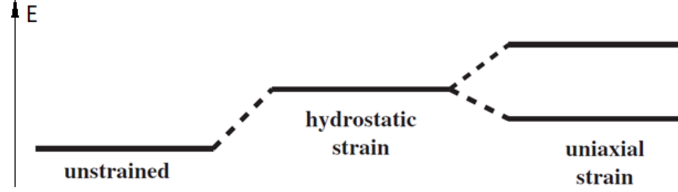

Figure 18: Hydrostatic and uniaxial strain effects on a doubly degenerate band. Hydrostatic strain shifts the band edge either to higher or lower energy, while uniaxial strain removes the degeneracy of the bands [97].

	Si [eV]	Ge [eV]	Sn [eV]
E_{Γ}^{u}	4.185	0.80	-0.41
E_{L}^{u}	1.65	0.66	0.09
a_{C}^{Γ}	1.98	-8.24	-6.00
a_{C}^{L}	-0.66	-1.54	-2.14
a_{V}	2.46	1.24	1.58
b_{s}	-2.1	-2.9	-2.7
C_{11}	165.8	128.5	69.0
C_{12}	63.9	48.2	29.3

Table 2: Si [145], Ge [145] and Sn [146] deformation potentials at room temperature.

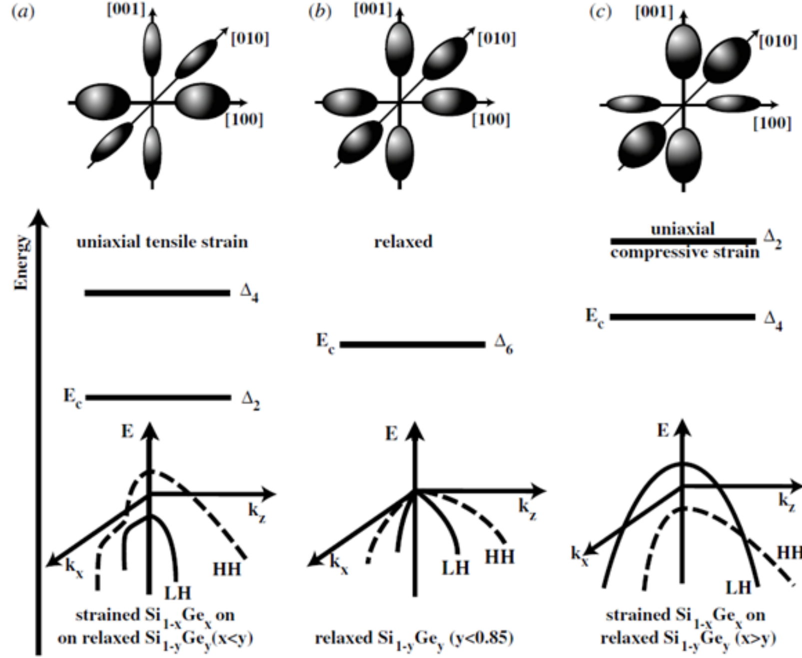

Figure 19: The conduction band, valley structure and valence band splitting of (a) uniaxial tensile strained Si or $Si_{1-x}Ge_x$ grown on a (100) $Si_{1-y}Ge_y$ substrate with $x < y$, (b) bulk Si and relaxed (100) $Si_{1-x}Ge_x$ with $x < 0.85$ and (c) uniaxial compressively strained (100) $Si_{1-x}Ge_x$ grown on a $Si_{1-y}Ge_y$ substrate with $x > y$ [97].

hydrostatic deformation potentials and b_s is the shear deformation potential. The relevant parameters of Eqs. 41 and 42 for Si, Ge and Sn are reported in Tab. 2. The effect of strain in $Si_{1-x}Ge_x$ alloys is schematically shown in Fig. 19.

Strain plays an important role also in the band structure of $Ge_{1-x}Sn_x$ alloys where the same equations hold. Different calculations performed with non-local pseudopotential method (Ref. [32]) as well as 30 band **k·p** method (Ref. [149]) unveiled that tensile strain results in reduction of the energy separation between L and Γ conduction band valleys; effect qualitatively similar to increase the Sn content. This raises an interesting possibility of employing tensile strained $Ge_{1-x}Sn_x$

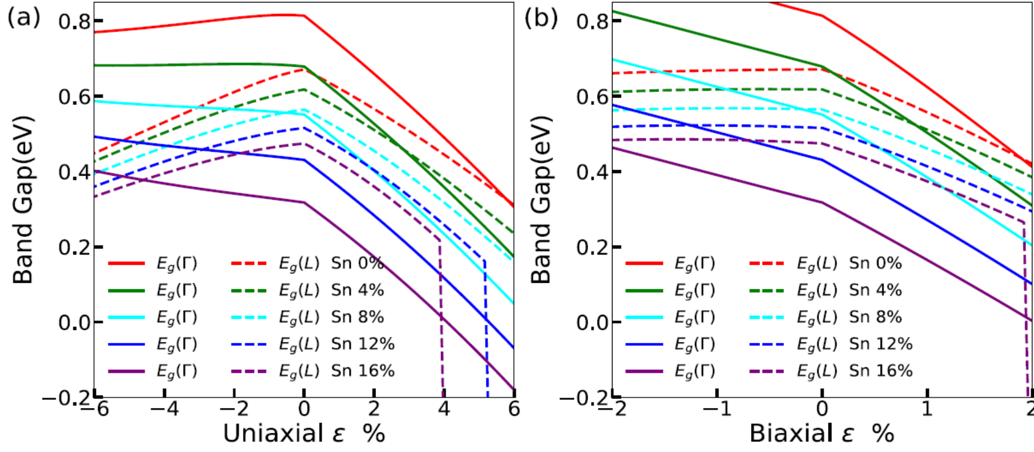

Figure 20: Bandgaps at the Γ-valley (solid) and L-valley (dashed) of $Ge_{1-x}Sn_x$ alloy with different Sn compositions versus (a) uniaxial strain and (b) biaxial strain along the <100> direction [149].

alloys for achieving a direct bandgap material. Indeed, a combination of strain and Sn alloying, may be able to relax the requirements on both the amount of Sn as well as the tensile strain needed for inducing indirect to direct bandgap crossover, thereby facilitating towards the achievement of a direct bandgap material.

The bandgaps at Γ and L-valley as a function of the uniaxial and biaxial strain along (100) direction for a range of Sn compositions are shown in Figs. 20a and b, respectively. The bandgap at L-valley decreases with the increase of strain while at Γ-valley we observe a monotonic behaviour throughout the range of uniaxial strain, regardless of the compressive to tensile nature [149]. For the biaxial strain, however, the bandgap at L-valley hardly changes under the influence of the compressive strain as shown in Fig. 20b. For both uniaxial and biaxial tensile strain, the decreasing rate of the Γ-valley is faster than that of the L-valley bandgap as shown in Figs. 20a and 20b. At a fixed Sn composition, tensile strain can also push the minimum of the CB at Γ-valley across with the maximum of the VB, causing the tensile-strained $Ge_{1-x}Sn_x$ alloy to have zero bandgap at the centre of the Brillouin zone. When this occurs, the CB and VB reverse in energy and it becomes meaningless to continue referring to the bandgap in L-valley (thus the

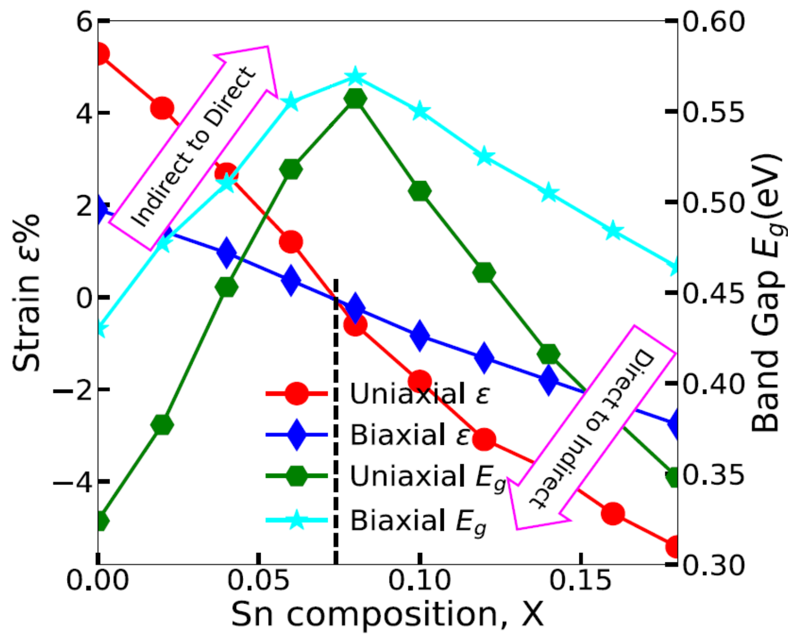

Figure 21: Uniaxial (red) and biaxial (blue) tensile strain required to induce in $Ge_{1-x}Sn_x$ an indirect-to-direct bandgap transition. The green and light blue curves show the bandgap of $Ge_{1-x}Sn_x$ alloys under uniaxial and biaxial strain, respectively. The dashed line highlights the indirect-to-direct transition point. All results have been obtained from a 30 band **k·p** simulation [149].

vertical dashed lines in Figs. 20a and b) [149].

A clearer picture is offered by Fig. 21 where we can see from blue and red data that tensile strain yields a lower Sn requirement for the direct-to-indirect transition, regardless of the uniaxial or biaxial strain, compared to the unstrained case that is marked by the vertical dashed line [149]. On the contrary, a compressive strain pushes the transition to a higher Sn content. For example, if we consider a biaxial strain of 1 % we find that a Sn molar fraction of ~3.8 % is required for the tensile strained material to become direct bandgap while it becomes ~10 % for the case of compressive strain.

Recent investigations showed that in a $Ge_{0.94}Sn_{0.06}$ sample grown on Ge, which inherently possessed a compressive strain of -0.32 %, a tensile strain could be applied by using a SiN_x stressor layer [150]. The application of 1.45 % tensile strain to these structures caused a transition into a direct bandgap alloy [150]. This demonstrates that strain engineering in this system can give appealing results and possibilities towards the fabrication of a device with tunable properties.

In this thesis all $Ge_{1-x}Sn_x$ samples are made from either partially-relaxed or compressive strained material and thus all possess an indirect bandgap.

7.3 Quantum wells

QWs are two-dimensional heterostructures in which electrons and holes are spatially confined in a region characterized by a thickness comparable to their de Broglie wavelength. Typically, carrier confinement is achieved by embedding a layer of a lower bandgap semiconductor with a thickness in the nanometer range, which defines the well region, into a matrix of a higher bandgap semiconductor, dubbed barrier (see Fig. 22a).

QW have attracted a great interest in the scientific community over the years since they offer the possibility to strongly modify the bulk electronic structure to achieve better optical performances. The localization of carriers in a spatially-reduced region can lead to an increased efficiency of the radiative recombination, thus enhancing, i.e., the PL signal [130].

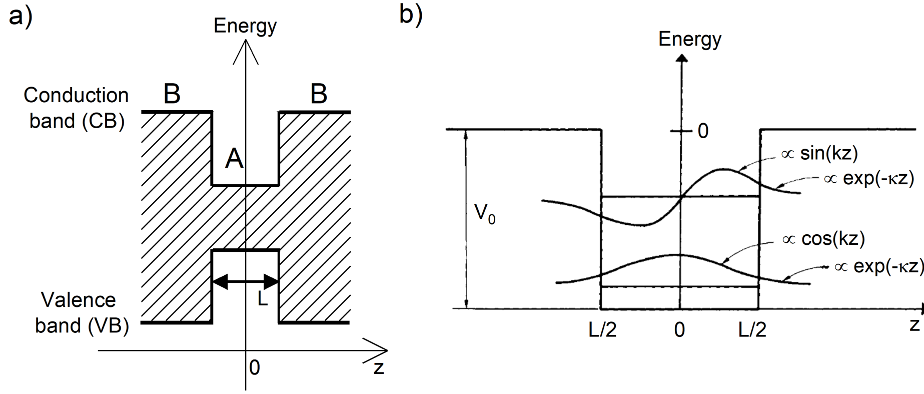

Figure 22: (a) Sketch of a single quantum well system. Material A constitutes the well, material B the barrier. (b) Finite-height quantum well where we show the first two confined levels and the corresponding wavefunctions. V_0 is the confining potential and L is the width of the well. Adapted from [76].

The energy levels can be calculated in the approximation of the envelope wave function [151–153] using a Kane model [154] for describing the electron and hole states. This model requires the following assumptions: the interface potential is strongly localized at the A-B interface, which means that the interface potential is delta-like when compared to the scale of variation of the envelope wave function and it does not mix the band-edge wave functions but only shifts them. It can then be shown that the wavefunction $\psi(z)$ can be written in the form [151]:

$$\psi(z) = \sum_{\mathrm{A,B}} e^{i\mathbf{k}_{\perp}\cdot\mathbf{r}}\, u_{n,\mathbf{k}}^{\mathrm{A,B}}(\mathbf{r})\,\chi_n(z) \tag{43}$$

where z is the growth direction, $\mathbf{k}_{\perp}$ is the transverse electron wave vector, $u_{c,\mathbf{k}}^{\mathrm{A,B}}(\mathbf{r})$ is the Bloch wave function in material A or B and $\chi_n(z)$ is the envelope wavefunc-

tion, determined by the Schrödinger-like equation:

$$\left(-\frac{\hbar^2}{2\,m^*}\nabla^2 + V_n(z)\right)\chi_n(z) = \epsilon_n\,\chi_n(z) \tag{44}$$

where m^* is the effective mass of the A or B material, $V_n(z)$ represents the potential introduced by a perturbation such as the potential profile of the well and ϵ_n is the energy of the carriers.

To solve Eq. 44 we must satisfy the continuity of the wavefunction $\chi(z)$ at the interface as well as the conservation of the particle current, that is $\frac{1}{m^*(z)}[\partial\chi(z)/\partial z]$.

We can now focus for on the CB, shown in Fig. 22b, by simply considering that an analogous treatment can be done for the VB. For any real case we have $V_n(z) = V_0 < \infty$. From symmetry considerations we get:

$$\chi_n(z) = \begin{cases} A\,cos(kz) & \text{if } -L/2 < \text{z} < L/2 \\ B\,e^{-\kappa\,(z-L/2)} & \text{if z} > L/2 \\ B\,e^{+\kappa\,(z+L/2)} & \text{if z} < -L/2 \end{cases} \tag{45}$$

with eigenvalues:

$$\epsilon_n = \begin{cases} \dfrac{\hbar^2 k^2}{2\,m_A^*} & \text{within the well} \\ V_0 - \dfrac{\hbar^2\kappa^2}{2\,m_B^*} & \text{within the barrier} \end{cases} \tag{46}$$

By applying both continuity conditions, we end up with:

$$A\,cos(k\,L/2) = B \tag{47}$$

$$A(k/m_A^*)\,sin(k\,L/2) = \kappa B/m_B^* \tag{48}$$

which can be combined into:

$$(k/m_A^*)\,tan(k\,L/2) = \kappa/m_B^* \tag{49}$$

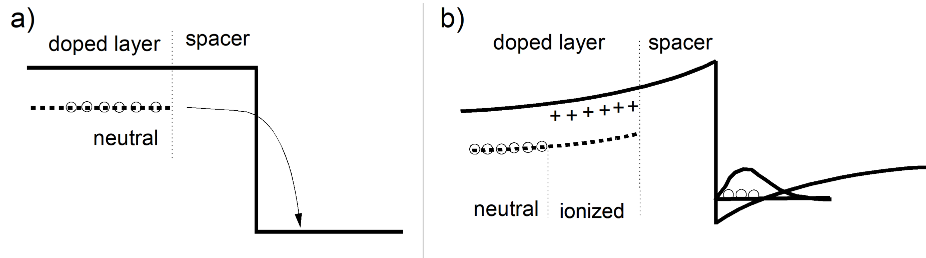

Figure 23: Schematic of the conduction band close to the interface of a modulation-doped heterostructure showing how electrons are separated from their donors. (a) Represents the moment the heterojuntion is made while (b) shows what happens to the carriers and the bandedge at the equilibrium after the charge transfer [129].

This equation can be solved numerically to obtain the number of bound states in the well.

7.3.1 Modulation doping

A low-dimensional system on its own is not enough to study the Rashba physics since the breaking of inversion symmetry is required, as described in Ch. 2. In our devices we achieve SIA via an asymmetric modulation doping.

It is worth noticing that advancements in high-performance transport devices were made by Dingle et al. [155] through the introduction of n-type modulation doping. Their device was composed of a GaAs-Al$_x$Ga$_{1-x}$As heterojuntion where only the higher bandgap layer was doped, while the GaAs layer remains nominally undoped. The underlying idea is that, at equilibrium, charge transfer occurs across a heterojunction to equalize the chemical potential on both sides [156]. The charge-transfer effect, which is schematically shown in Fig. 23 for the case of electrons in CB, makes possible to obtain conducting electrons in a high-purity, high-mobility semiconductor channel spatially separated by potential scattering centres. Since then, this technique has become a common practice in various semiconductor devices [142, 157–159].

The impressive development of the subject is due to the applicability both to basic science (two-dimensional physics [158], quantum Hall effect [142, 157]) and to very high-performance devices, e.g. HEMT (high-electron-mobility transistor), TEGFET (two-dimensional electron-gas FET) [160], SDHT (selectively doped heterostructure transistor), and MODFET (modulation-doped FET) [161].

7.3.2 Magnetotransport in 2D systems

By exploiting a modulation doping technique it is possible to achieve a high mobility in the QW and the formation of a 2DEG or a 2DHG. One way to determine the formation of a 2DEG is by performing transport measurement in a magnetic field as the Hall effect exhibits qualitatively new features. In the following we deal with the case of 2DEG; however, the whole discussion holds also for a 2DHG.

The Hall effect appears when a conductor is placed in a magnetic field, as shown in Fig. 24a. The charge carriers flowing through the conductor are deflected due to the Lorentz force (F_L) causing a transverse, or Hall voltage (V_{xy}), between the sides of the material, perpendicular to both the magnetic field and the direction of the current (I). The Hall voltage is linearly proportional to the magnetic field (B), while the longitudinal voltage (V_{xx}) is magnetic field independent. Therefore when measuring the longitudinal (ρ_{xx}) and the Hall (ρ_{xy}) resistivity the same behaviour is found, as shown in Fig. 24b with black and red lines respectively. These are the classical Hall effect signatures in semiconductors.

However, in presence of a 2DEG, the integer quantum Hall effect is observed [162]. In this case, ρ_{xy} changes in steps with plateau structures occurring as the magnetic field is increased, as shown in Fig. 24c with red line. At the same time, when a plateau is observed, ρ_{xx} drops to zero creating an oscillatory behaviour shown in Fig. 24c as black line. These features are know as the Shubnikov-de Haas oscillations of the longitudinal magnetoresistance [162].

For a magnetic field (B) along the z direction the energy spectrum of the elec-

trons can be described as:

$$E_l = \frac{\hbar^2 {k_z}^2}{2m_e} + \hbar\omega_c\ (l + 1/2) \tag{50}$$

where E_l is the l-th quantized level, $\omega_c = eB/m_e$ is the cyclotron frequency and l is a positive integer number. These levels, known as Landau levels, are further split by the Zeeman energy. The cyclotron and Zeeman energies are linearly proportional with B, thus moving to higher energy as B is increased. Each energy level depopulates as it passes through the Fermi energy, causing a measurable oscillation in the longitudinal resistivity. Since thermal energy can promote electrons from one level to another, such phenomena emerge when measurements are conducted at low temperature, typically in the range of hundreds of mK [162].

7.3.3 Quantum-confined Stark effect

In a confined system, the electric field causes an effect on the energy levels and carriers wavefunction known as the quantum-confined Stark effect (QCSE) [76, 164].

If we restrict ourselves to the case of QW centered at z = 0 with a type-I band alignment. Whenever an electric field (E_z) is applied along the growth direction of the QW, the potential energy of a confined electron changes according to:

$$\Delta E_e = e\,z\,E_z \tag{51}$$

where ΔE_e is the energy shift from the unperturbed case and e is the electron charge. The potential energy, thus, gains a linear term as a function of distance along the z axis.
This gives rise to different effects:

- the variation of the confining potential causes the CB and VB to tilt. This changes the QW from a square to a triangular profile causing a renormalization of the wavefunctions as well as a change in the positioning of the

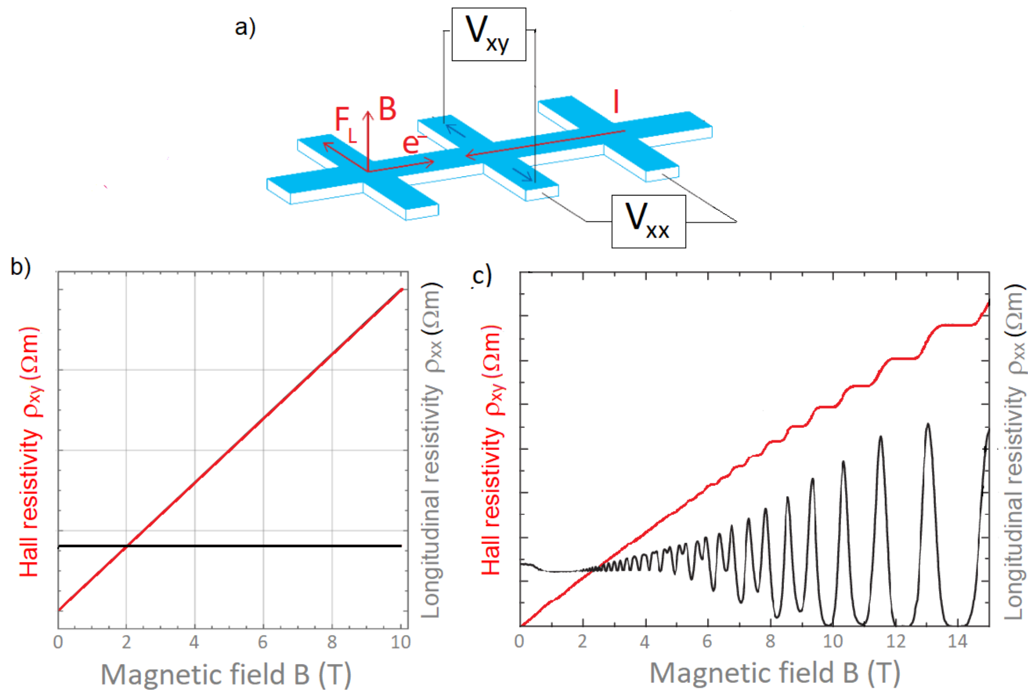

Figure 24: (a) Schematic showing the Hall effect measurement setup in a standard Hall bar geometry with arbitrary sizes. V_{xx} and V_{xy} voltages are measured along and perpendicular to the current flow. The conventional current I flows along the main channel. The Lorenz force F_L is perpendicular to the magnetic field (B) and the charge carrier motion. In the lower panels we show the ρ_{xx} and ρ_{xy} plotted as a function of B. (b) Classical Hall effect behavior, where ρ_{xy} is proportional to B while ρ_{xx} is constant. (c) Typical signatures of the quantum Hall effect where ρ_{xy} shows plateaus, with ρ_{xx} going to zero at the same time. Adapted from [163].

energy levels [129]. The overall effect of the electron and hole level repositioning is a reduction of the bandgap (see Fig. 25a and b);

- the electric field pushes the electrons and holes in opposite directions. The concomitance of this effect with the triangular profile of the well causes the new wavefunctions to be no more symmetric with respect to the centre. In particular, the maximum of the wavefunctions of electron and hole are found in opposite direction with respect to the centre and closer to the interface between the well and the barrier (see Fig. 25b);

- when considering the zero field case the electron-hole overlap[4] is high since the maxima are both found at the centre of the well. On the contrary, the wavefunction shift caused by the electric field reduces the overlap (see Fig. 25b).

There exist no analytical way to determine the wavefunctions of a finite-height well. Therefore a numerical simulation is required if we want to study the QCSE in real systems. However, for the purpose of understanding, in the following we exploit the exact solution found for infinite barriers. Perturbation theory in this case gives the shift (ΔE) to the first level in a small electric field as [165]:

$$\Delta \mathrm{E} = -24\left(\frac{2}{3\pi}\right)^6 \frac{e^2 \mathrm{E_z}^2 m^* d^4}{\hbar^2} \tag{52}$$

where e is the electron charge, $\mathrm{E_z}$ is the electric field, m^* is the effective mass and d is the well width. Equation 52 predicts a negative shift which means that the bandgap shrinks with the electric field. Notably, for infinite barriers the reduction scales quadratically with the electric field.

[4]The electron-hole overlap is defined as $M_{nn'} = \int_{-\infty}^{+\infty} \Psi^*_{en'}(z)\Psi_{hn}(z)dz$ where n and n' are the nth hole state and the n'th electron state, $\Psi^*_{en'}$ the electron wavefunction in the n'th state and Ψ_{hn} the hole wavefunction in the nth state. $M_{nn'}$ describes how much the two wavefunctions are spatially superimposed with important implication in band-band transitions [76, 129].

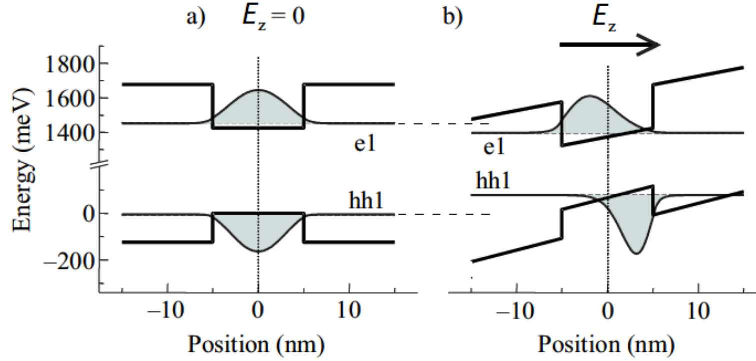

Figure 25: (a) Schematic of the QW under no applied bias. (b) Manifestation of the quantum-confined Stark effect. Upon application of an electric field (E_z) we observe the tilt of the bandedges, with a consequent reduction of the bandgap, as well as the shift of the wavefunctions baricentres to opposite directions [76]. In the figure e1 (hh1) is the first confined state in the CB (VB). The horizontal dashed lines are a guideline to highlight the reduction of the bandgap.

Of interest in this thesis, the QCSE can be observed with a PL measurement as it affects the optical transitions of a device. For example, the bandgap reduction caused by the electric field can be observed as a redshift of the emission. Additionally, the reduced overlap of the wavefunctions has a negative impact on the intensity of the PL signal. As a matter of fact, the overlap describes the probability of the transition between two states, thus expecting a loss of emission intensity when the overlap becomes smaller.

In this thesis we will consider $Ge/Si_{0.15}Ge_{0.85}$ QW embedded in a p-i-n diode, as the type-I band alignment of this system (see Fig. 26) offers a suitable platform to observe the QCSE. In this device the external electric field can additionally tune the total electric field across the heterostructure, thus allowing for a precise investigation.

Application wise, the QCSE is routinely used in high-performance QW modulators for telecommunications [138, 167, 168]. It possesses a number of attractive properties that allow for integrable modulators with only micrometres of path length [169], as well as devices at telecommunications wavelengths of ~ 1.55 µm

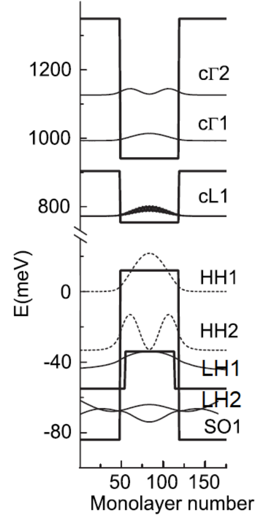

Figure 26: Calculated band offsets and square modulus of the wavefunctions of electron and hole in confined states in a 10-nm-thick Ge/$Si_{0.15}Ge_{0.85}$ QW [166].

[170]. Kuo et al. [138] were the first to demonstrate in 2005 a clear quantum confinement effects in the absorption spectra of Ge QWs, associated with zone centre transitions, and in addition a clear and strong QCSE. The two peaks found in the absorption coefficient of Fig. 27a are assigned to HH1-cΓ1 (0.88 eV at 0 V) and LH1-cΓ1 (0.91 eV at 0 V) transitions. With a reverse bias from 0 to -4V, both peaks are redshifted by the QCSE. The HH1-cΓ1 moves from 0.88 eV (0 V) to 0.85 eV (-4 V) and remains visible even at the maximum reverse bias of -4 V, while the LH1-cΓ1 washes out for bias greater than -3 V. The strong modulation is found to be comparable to III-V materials (see Ref. [171]) at similar wavelengths despite the indirect nature of Ge. A theoretical modeling from Virgilio and Grosso supported the experimental results by calculating the electronic structure of the system through first-neighbor tight-binding Hamiltonian with $sp^3d^5s^*$ orbitals and spin-orbit coupling (details on the model can be found in Ref. [172]). The agreement between the theory (Ref. [172]) and the experiment (Ref. [138]) is very good confirming also the quadratic dependence of the QCSE on the field strength as proposed in Eq. 52.

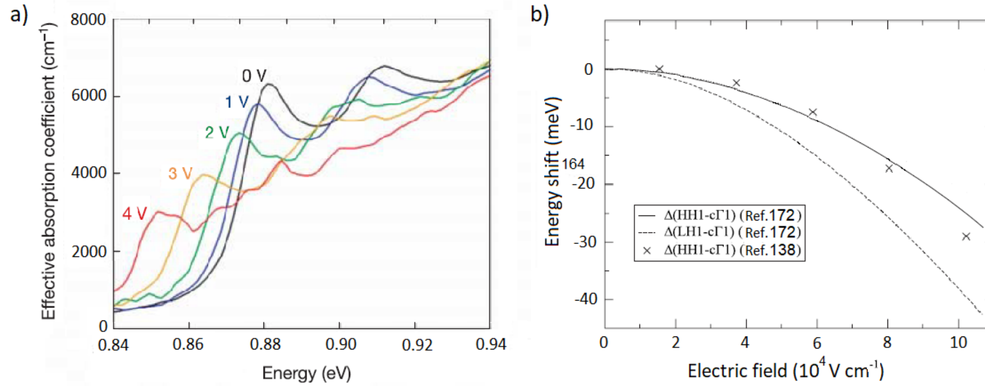

Figure 27: (a) Absorption coefficient measured at room temperature in $Ge/Si_{0.15}Ge_{0.85}$ quantum wells. The reverse bias is changed from 0 to 4 V [138]. The peak at 0.88 eV at 0 V is attributed to the HH1-cΓ1 transition and the peak at 0.91 eV at 0 V to the LH1-cΓ1 transition. (b) Stark shift calculated for HH1-cΓ1 and LH1-cΓ1 transitions though first-neighbor tight-binding Hamiltonian [172]. Experimental points from Ref. [138] are reported as crosses.

Successive studies have confirmed that group IV materials can be successfully exploited for applications such as silicon-based electro-absorption modulators [137, 173].

8 Chemical vapour deposition

Our samples are heteroepitaxially grown by means of chemical vapour deposition (CVD). CVD is a widely-used materials processing technology in which thin films are formed on a heated substrate via a chemical reaction of gas-phase precursors. CVD offers tunable deposition rates as well as high-quality products with excellent conformality since it relies on controllable chemical reactions. Usually, CVD does not require ultra-high vacuum environments, making it a popular technology for different fields such as electronics, optoelectronics and surface modification applications [174].

In the CVD growth the process consists of the following steps (Fig. 28). First, a mass-controlled reactant gas flows into the reactor. These reactant gases either form intermediate reactants and gaseous by-products or diffuse directly to the substrate. In both cases, the reactant gases and the intermediate reactants are adsorbed onto the heated substrate surface and then diffuse. These continuous reactions at the gas–solid interface lead to a thin film formation via nucleation, growth and coalescence as well as formation of reaction by-products. Finally, any gaseous species (both products and unreacted precursors) desorb and are removed from the reaction zone.

Many different CVD versions have been developed for different purposes. For example the operating pressure can be changed, such as ultra-high vacuum (UHV) or reduced-pressure (RP) CVD, or the chemical reaction can be favoured by additional components, such as for plasma-enhanced (PE) or photo-assisted (PA) CVD, or can be used for specific purpose, such as metal-organic (MO) for the growth of III-V compounds or oxidative CVD for polymer films [174, 175]. For the scope of this thesis only the relevant low-energy plasma-enhanced (LEPE) and RP CVD processes are described.

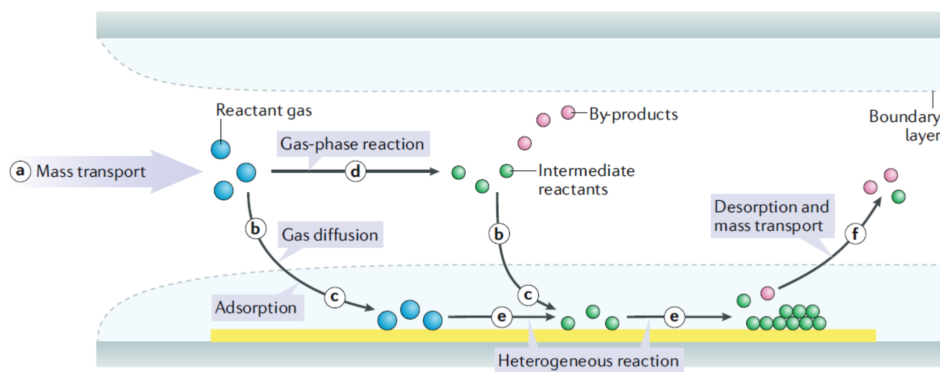

Figure 28: Schematic of the general elementary CVD processes [174]. In the first step (a) the reactant gases flow into the reactor. Then, there are two possibilities for the reactant gases: direct diffusion and adsorbtion onto the substrate (b and c); or formation of intermediate reactants and by-products via the gas-phase reaction (d) and deposition onto the substrate by diffusion (b) and adsorption (c). Surface diffusion and heterogeneous reactions (e) take place on the surface of substrate before the formation of thin films or coatings. Finally, by-products and unreacted species are desorbed from the surface and forced out of the reactor as exhausts (f) [174].

8.0.1 Low-energy plasma-enhanced CVD

In this thesis the Ge/$Si_{0.15}Ge_{0.85}$ QW are grown via LEPECVD. The LEPECVD is a technique that is suitable for the growth of $Si_{1-x}Ge_x$/$Si_{1-y}Ge_y$ heterostructures and benefits from a high growth rate and low substrate temperature [176–178]. Conventional CVD techniques are limited by the exponential suppression of the growth rate with the substrate temperature [179], that causes the desorption of the H from the surface. In LEPECVD process an arc current of 20-80 A is struck between the source and the chamber, generating an arc voltage of less than 30 V to sustains the plasma. This implies that the ion energy is low enough (10 eV) not to cause any damage to the crystal structure. A magnetic field drives the plasma onto the substrate which is thermally regulated by a graphite heater. Precursor gases like SiH_4 and GeH_4 are used for the materials growth, while PH_3 and B_2H_6 are diluted in Ar and used for doping. H_2 can be introduced as well to clean the surface or to change the mobility of adatoms, regulating the growth dynamics. This technique makes the growth rate and film composition independent of the substrate temperature. The magnetic field strength, the gas flow as well as the plasma arc current can be tuned to vary the growth rate between 0.1 nm/s up to 10 nm/s with substrate temperature of 450-750 °C [180, 181].

8.0.2 Reduced-pressure CVD

In this thesis the $Ge_{1-x}Sn_x$ samples have been grown by RPCVD. In the RPCVD a lower pressure is used to decrease any unwanted gas phase reactions, and also increases the uniformity across the substrate. This technique is used for the growth of $Ge_{1-x}Sn_x$ alloy since it offers the possibility to obtain proper nonequilibrium conditions required to overcome the low solid solubility of Sn in Ge [182, 183]. As described in Ch. 6, one of the main issue for the growth of Sn-rich $Ge_{1-x}Sn_x$ epilayers is the Sn segregation since Sn has a comparably low free surface energy [184, 185]. To prevent segregation, the temperature must be kept as low as possible, since a low growth temperature reduces the mobility of Sn adatoms, hin-

dering the Sn clusterization. The RPCVD allows for the growth to be performed at a relatively low substrate temperature of in the range of 250-350 °C [186–189].

The CVD sources that are normally used in synthesis of Si-based semiconductors are the hydrides SiH_4, GeH_4, Si_2H_6 and Ge_2H_6. The analogous compounds of Sn, stannene (SnH_4) and distannene (Sn_2H_6), are unstable at room temperature because of the significantly lower Sn–H bond energy [103]. The availability of stable precursors prevented the development of CVD-grown $Ge_{1-x}Sn_x$ alloys for a long time. First trials were performed by using $C_6H_5SnD_3$ [103] and SnD_4 [190], however it was only in 2011 when Vincent et al. introduced $SnCl_4$, in combination with Ge_2H_6, that the epitaxy of $Ge_{1-x}Sn_x$ alloy started to become accessible [104]. $SnCl_4$ is a stable and commercially available precursor that is used in glass industry for SnO_2 coatings [31]. One of the most important achievements enabling high quality CVD-grown $Ge_{1-x}Sn_x$ alloys with Sn > 3 % was the development of high quality Ge virtual substrate (VS), that is a thick layer deposited onto Si and used as a substrate for the growth of successive layers, [191–193] representing a convenient alternative to the expensive and brittle Ge(001) substrates. Using Ge VS instead of growing directly on Si has significantly reduced the lattice constant mismatch between substrate and epilayer and, thus, improved the crystalline and optical quality of $Ge_{1-x}Sn_x$ alloys leading, among other things, to enhanced optical properties and lasing action [143, 194–196].

The growth of $Ge_{1-x}Sn_x$ epilayer as well as QW samples investigated in this thesis was performed with an ASM Epsilon 2000 Plus RPCVD epitaxial deposition system. The Epsilon is a horizontal flow, load-locked reactor, featuring a lamp heated silicon carbide coated graphite susceptor in a cold wall quartz chamber.

9 Ge/$Si_{0.15}Ge_{0.85}$ multiple QWs p-i-n diodes

As described in Ch. 2.1, the manipulation of the spin by means of an electric field is an appealing possibility in the spintronics field. In group IV materials this opportunity is offered by the Rashba field, which is established in structures that possess the SIA. In this chapter we focus on p-i-n diode structures that embeds 50 Ge QW in $Si_{0.15}Ge_{0.85}$ barriers. The presence of the Rashba field is ensured by the intrinsic asymmetry of the p-i-n structure and the metal contacts offer the possibility to investigate the electrical manipulation of the spin. In this chapter, at first the electrical response is studied and then we present the optical investigation of the spin-dependent properties.

9.1 The Ge/$Si_{0.15}Ge_{0.85}$ p-i-n devices

The samples investigated in this chapter are p-i-n diodes grown by LEPECVD where the intrinsic region is made of 50 Ge/$Si_{0.15}Ge_{0.85}$ multiple QWs (MQWs). On a Si (001) substrate, a 13 μm $Si_{1-x}Ge_x$ graded buffer is deposited by linearly increasing Ge concentration from 0 to 90 % with a step of 7 %/μm; then a fully relaxed 2 μm constant composition $Si_{0.10}Ge_{0.90}$ layer is deposited. A 200 nm p-type (4×10^{19} cm^{-3} with B as dopant) $Si_{0.1}Ge_{0.9}$ contact and a 200 nm $Si_{0.1}Ge_{0.9}$ spacer are then grown. The growth continues with a stack of 50 Ge MQWs with a thickness of 17 nm sandwitched between 23 nm of $Si_{0.15}Ge_{0.85}$ barriers. Finally, a 250 nm $Si_{0.1}Ge_{0.9}$ spacer and a 100 nm n-type (2×10^{19} cm^{-3} with P as dopant) contact are grown to finalize the p-i-n structure. During the growth the chamber pressure is kept at approximately 2×10^{-2} mbar. A chemical etching is then performed consisting of 22 Bosch cycles to realize cylindrical mesa. On each chip, 4 diodes are realized with different diameters of the mesa, namely 200 μm, 300 μm, 400 μm, 500 μm. A 1-μm-thick aluminum contact is realized on both p- and n-contact through a final lithographic step. A schematic layout of the device is presented in Fig. 29, while a typical optical image is shown in Fig. 30. The growth, the lithography are carried out by the L-NESS group at Politecnico di

Milano. X-ray diffraction (XRD) measurement, needed to determine the well and barrier thickness, are reported in Fig. 31.

A good optical quality is ensured by the graded buffer which reduces the effect of the lattice mismatch between the Si substrate and the Ge-rich layers yielding to a threading dislocation density of about 4-5×$10^6 cm^{-2}$ in the relaxed $Si_{0.10}Ge_{0.90}$ layer [197]. This value is two orders of magnitude lower than the typical threading dislocation density of Ge layers directly grown on Si [198–200]. In order to adapt the well and barrier lattice parameter to that of the relaxed $Si_{0.10}Ge_{0.90}$ layer, wells and barriers experience compressive and tensile strain, respectively. Therefore, to avoid the nucleation of defects that can arise from the growth of a µm-thick stack, the thickness and composition of the well and barrier are carefully chosen to give a null mean strain. We thus have:

$$a_S = \frac{d_W\, a_W + d_B\, a_B}{d_W + d_B} \tag{53}$$

where d is the layer thickness, a is the lattice parameter, while S, W and B refer to substrate, well and barrier, respectively. The strain compensation achieved in this way further consolidate that the material possesses a good optical quality.

9.2 Electrical investigation

Since all the devices have similar electric response, we present here only the results obtained for the device with a diameter of 500 µm (the investigation for the other devices is reported in Appendix C). The dark current is recorded at different temperatures, i.e., from 300 K to 4 K. The results are shown in Fig. 32a where we plot the absolute values of the current. At room temperature the device possesses a typical diode response with the forward bias measuring a higher current than in the reverse regime. When the device is cooled down to 4 K, the rectifying behavior is less pronounced. In particular, the forward regime has a stronger reduction in the current than the reverse one so that at 4 K the direct and reverse branches are similar in magnitude. This is attributed to two dominating contributions. The

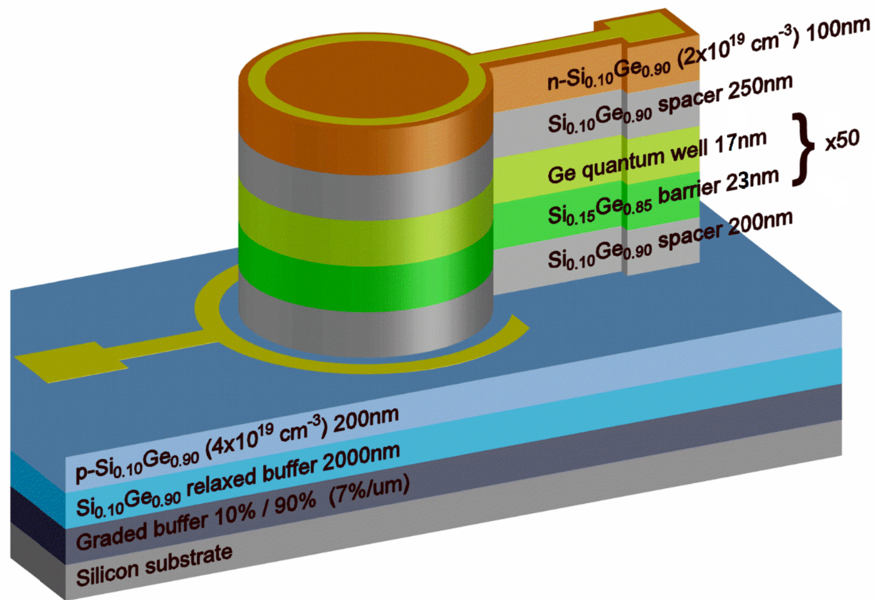

Figure 29: Sketch of the p-i-n device studied in this thesis.

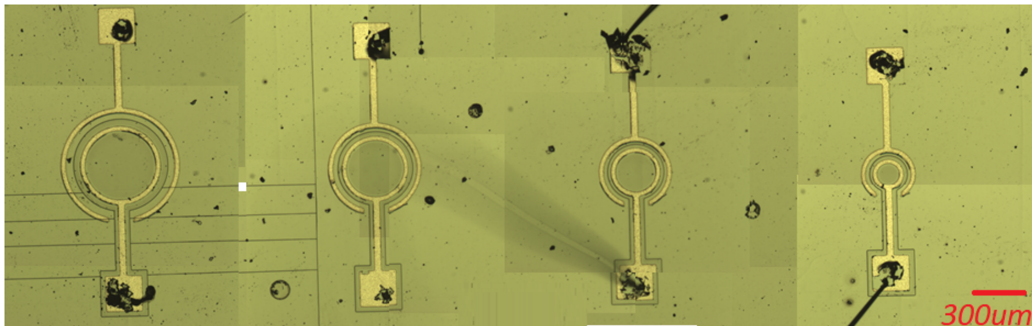

Figure 30: Optical image of the Ge/$Si_{0.15}Ge_{0.85}$ QW p-i-n chip. Four cylindrical diodes are patterned with different mesa diameters. From left to right: 500 µm, 400 µm, 300 µm, 200 µm.

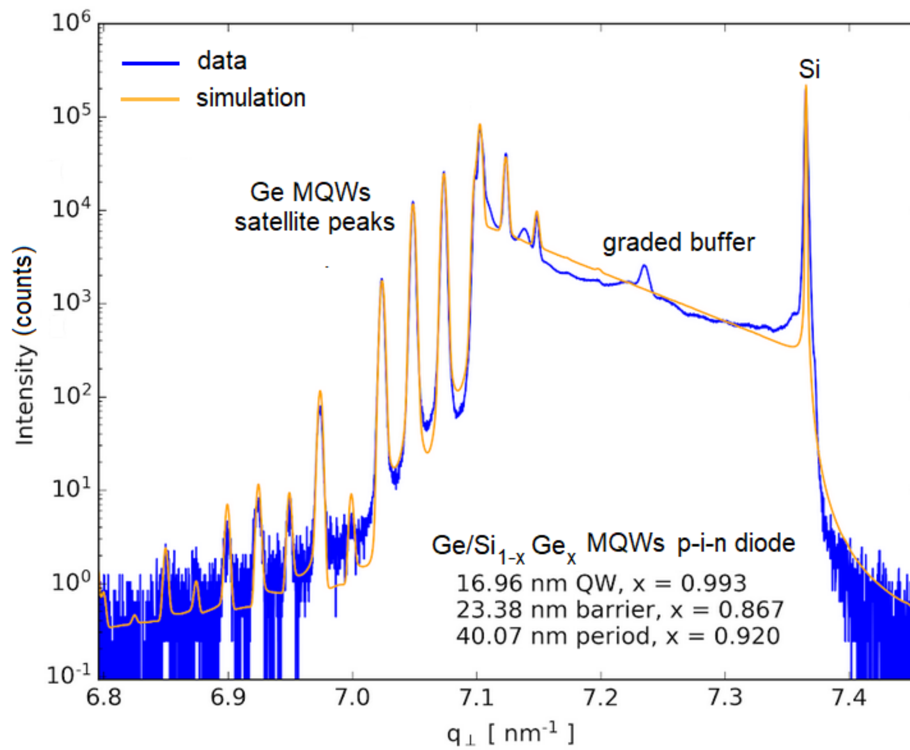

Figure 31: XRD scan of the Ge/$Si_{0.15}Ge_{0.85}$ MQWs. It is possible to see features from the underneath Si, graded buffer [201] and satellite peaks of the Ge MQWs stack. Angular coordinate has been converted to reciprocal space coordinate. Blue line represents the data while the yellow one is a simulation.

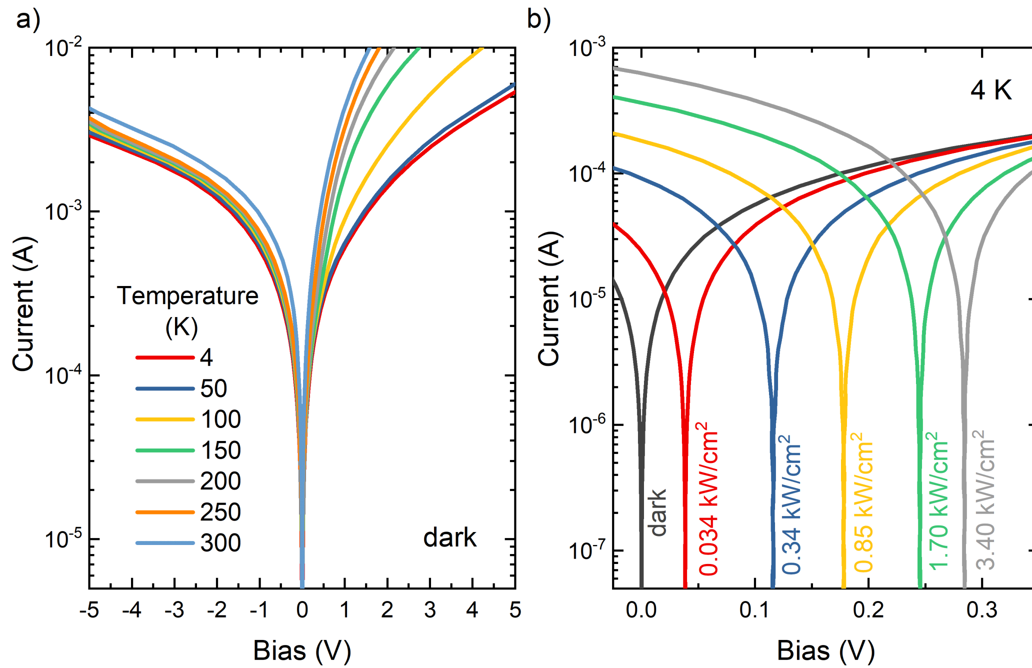

Figure 32: (a) I-V characteristics at dark in the temperature range 4-300 K. (b) I-V characteristics at 4 K under an excitation from a 1.16 eV CW laser with a spot diameter of 50 µm by varying the illumination power density.

first is the increase of the material bandgap that occurs when the temperature is lowered, causing a higher tunneling barrier for the majority carriers with a consequent suppressed recombination current. The second contribution arises from the thermal freezing of carriers that are less mobile, causing a reduction of the generation current.

The device is also investigated under different illumination conditions, as reported in Fig. 32b. By increasing the illumination the open circuit voltage (V_{OC}) shifts as expected to higher values.

The electrical response discussed here proves that the diode well behaves although it is not yet optimized in terms of leakage currents.

9.3 Device simulation

The device is simulated using the *nextnano* software package [202] following two methods. For the states at the centre of the Brillouin zone, we exploited an 8-bands **k**·**p** calculation, while for the zone edge states we used an effective mass approximation (the code is reported in Appendix D). The bandedges of Γ, L, LH and HH levels are calculated over the whole structure at low temperature (4 K) and the results are reported in Fig. 33a. The simulation confirms the type-I band alignment described in Ch. 7.1.The asymmetric doping of the device causes the emergence of a built-in bias of approximately 0.86 V. We then turned on the external polarization and sweep the bias from -10 to +10 V. We report these extremal cases in Fig. 33b and Fig. 33c, respectively. In the direct polarization, we observe that the potential barrier from the n- to the p-doped layer is reduced, favoring the current that flows from the n-side to the p-side. On the contrary, in the indirect polarization the potential barrier increases, hindering the tunneling probability and leading to a reduced recombination current.

A magnification of one QW is presented in Fig. 34a and 34b for the cases of no bias and -8 V, respectively. We include the first level of each state together with the calculated probability density ($|\Psi|^2$). The choice of the levels is dictated by the observed transitions in the PL spectrum (see Ch. 9.4). Three arrows representing the fundamental transition energies are also reported, namely cL1-HH1 occurs at 0.752 eV, cΓ1-HH1 at 0.956 eV and cΓ2-HH2 at 1.060 eV. The excitonic contribution has been neglected in the calculation.

The application of the external field causes a noticeable bending of the band edges along the growth direction as well as a shift of the electron and hole probability densities in opposite directions towards the barrier/well interface. The confinement energy withing the well is perturbed in a way that the separation between the levels is reduced causing the transitions to be redshifted by few meV. As explained in Ch. 7.3.3, all these aspects are a hallmark of the QCSE.

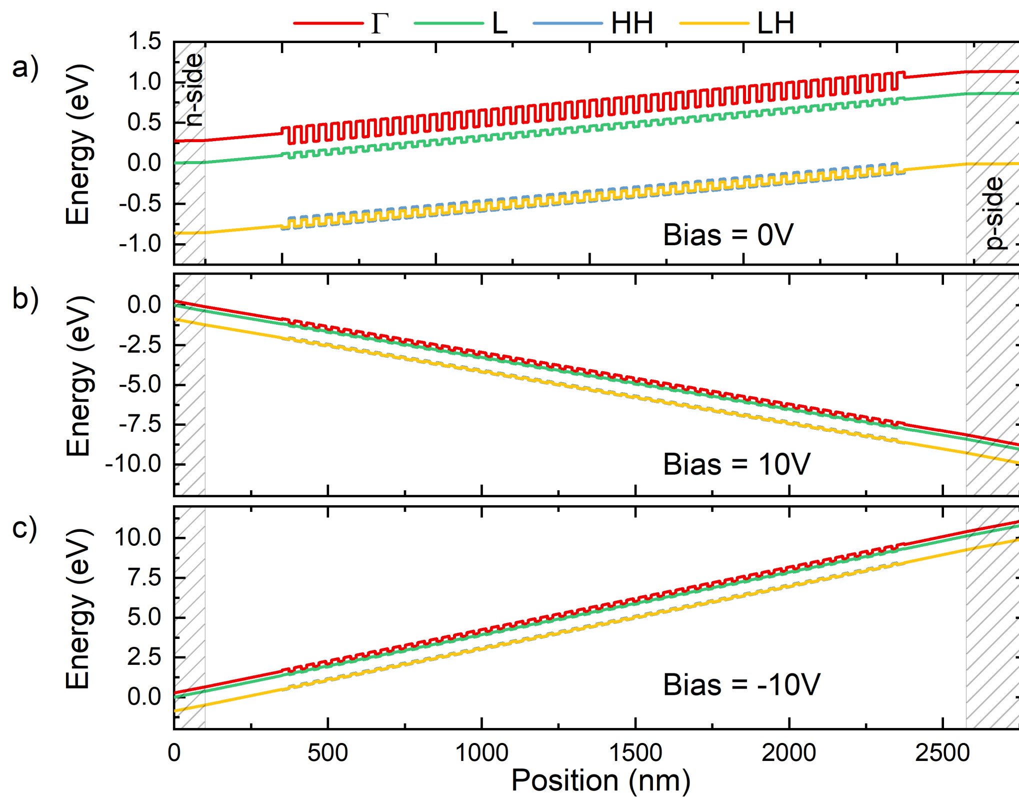

Figure 33: Calculated bandedges of Γ, L, HH and LH states of the overall structure at 4 K with an external bias applied of: (a) 0 V, (b) -10 V, (c) +10 V. The dashed areas represent the n- and p-doped regions.

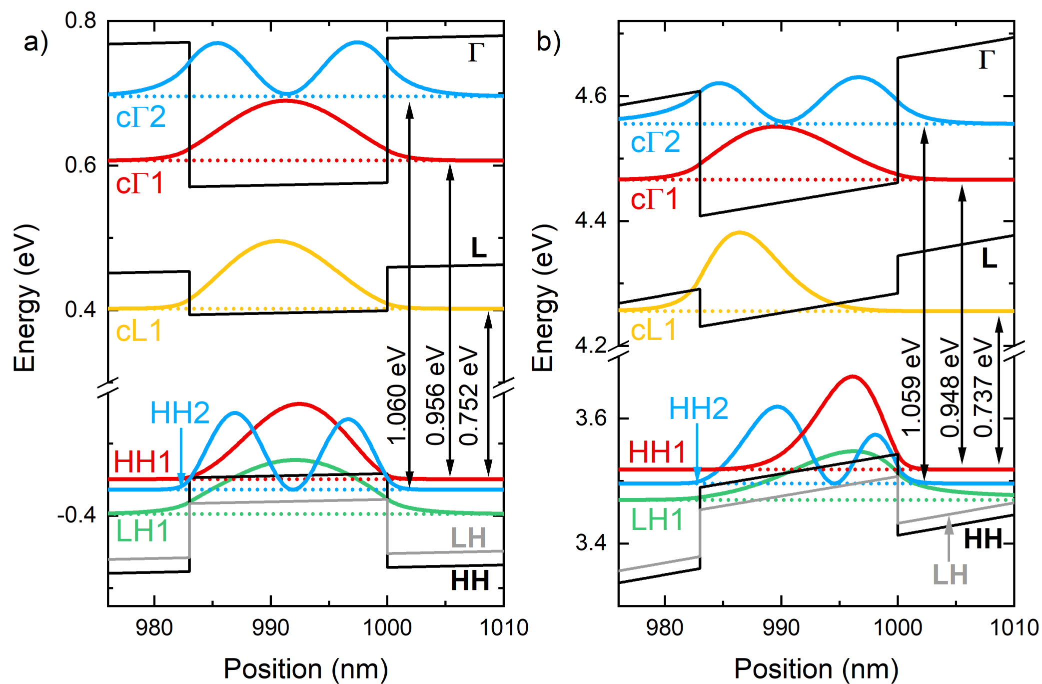

Figure 34: Simulation of the main states obtained using *nextnano* with a 8-bands **k**·**p** method for the states at the zone centre. For L-states we exploited an effective mass approximation. We report also the first energy levels of each state with the corresponding $|\Psi|^2$ for a 4 K temperature. The arrows indicate the main transitions that are observed in the PL spectrum with the corresponding calculated energy. The external bias is set to (a) 0 V, (b) -8V. No excitonic contribution is taken into account.

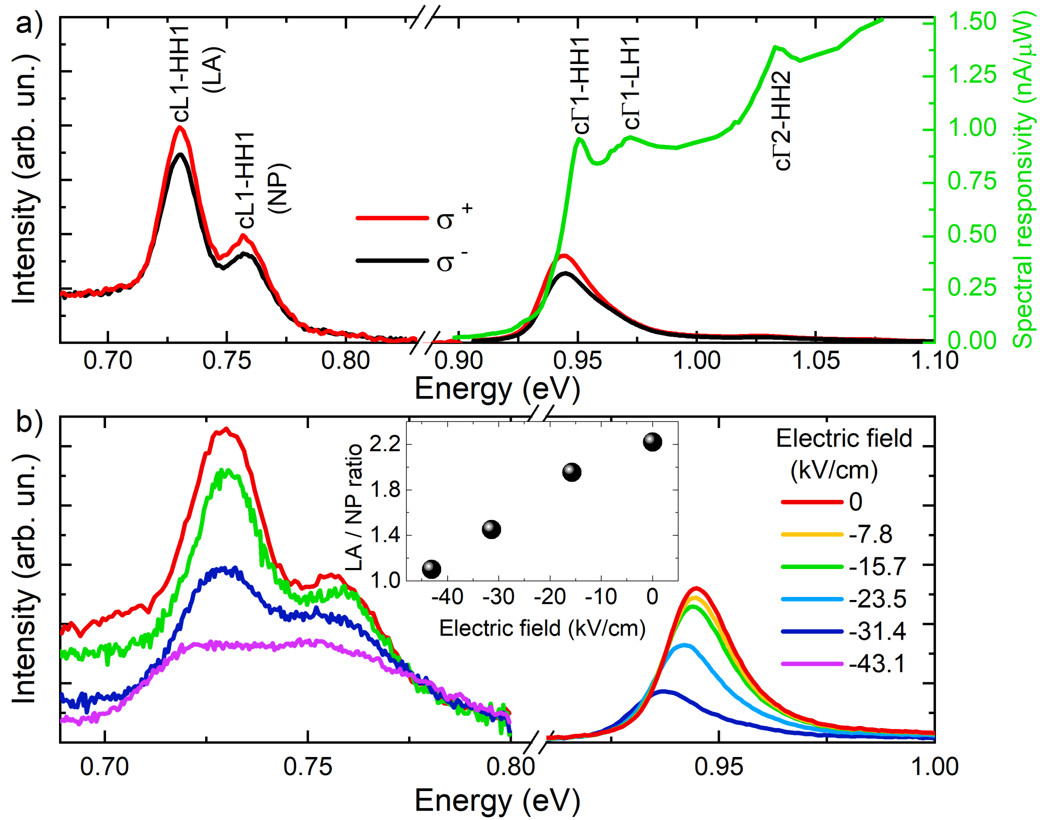

Figure 35: (a) Low temperature (4 K) PL of the $Ge/Si_{0.15}Ge_{0.85}$ QW p-i-n device. The excitation is performed by a 1.165 eV laser with a power density of 3.40 kW/cm^2 (the spot diameter is 50 μm). The right-handed circularly polarized (σ^+) PL component is reported as a red line, whereas the left-handed one (σ^-) is shown as a black line. The PL spectrum is obtained by merging data from a linear InGaAs array (> 0.83 eV) and an extended InGaAs single channel detector (< 0.83 eV). The spectral responsivity of the p-i-n diode is shown as a green line. (b) Right-handed spectra of QWs under 3.40 kW/cm^2 illumination for different applied electric fields (in our case 1 V = 3.9 kV/cm). In the inset we show the ratio between the LA and NP peak intensity as a function of the electric field (see the main text for additional details).

9.4 Optical investigation

The diodes are measured at 4 K and the PL spectrum obtained at zero external bias is shown in Fig. 35a. Two different detectors are used for covering the whole spectral region and the results are merged together (see Ch. A.1). In this way, both direct and indirect radiative emissions are shown simultaneously, while ensuring the best possible signal-to-noise ratio. Indeed, the InGaAs array detector used for probing the direct emission has a cut-off at approximately 0.77 eV, thus limiting the investigation of the indirect emission due to the poor quantum efficiency below that energy threshold. On the other hand, the InGaAs single channel detector has a cut-off energy at approximately 0.52 eV and possesses a quantum efficiency that is higher in the spectral region of the indirect transition than in the direct one (see Ch. A.1 for details on the detectors), thus offering a way to investigate the low energy window.

Two main regions can be observed in the PL spectrum and the simulated energies allow for an easier attribution of the origin of the special features. All of them arise from the Ge QWs: the peak at 0.945 eV can be attributed to the cΓ1-HH1 recombination, whereas at lower energies the peak at 0.757 eV can be associated to the no-phonon (NP) cL1 – HH1 transition and is accompanied by a longitudinal-acoustic-phonon (LA) replica redshifted by about 27 meV [136, 166]. The low-energy tail of the indirect transition stems from the contribution of the broad emission of defects, chiefly dislocations [166]. At the high energy side of the cΓ1 – HH1 peak a small contribution can be seen at approximately 1.027 eV. The **k·p** calculation suggests that its origin can be found in the recombination involving the cΓ2 and HH2 energy levels.

Additionally to the **k·p** calculation, our identification of the direct transitions is further supported by spectral responsivity (SR) measurements, reported as a green line in Fig. 35a. For this measurement the sample is illuminated by a tunable supercontinuum laser over a wavelength range of 1150-1450 nm with a step of 2 nm. A chopper allows for an intensity-modulated analysis coupled with a lock-in amplifier for the detection of the photocurrent signal. The zero-bias photocurrent

is then normalized by the power of the laser at the corresponding wavelength. The small blueshift (~7 meV) of all the SR structures compared to the associated PL arises from the structural fluctuation of the QW thickness, commonly referred to as Stokes shift phenomenon [166, 203]. Possibly a superimposed effect can be the thermal shrinkage of the bandgap due to the higher pump power (roughly 500 times) used for the PL analysis.

The excitation for the optical investigation is obtained with a right-handed circularly polarized laser with an excitation energy of 1.165 eV and a spot diameter of 50 μm. The spectra resolved for co- (σ^+) and counter-circular (σ^-) polarization with respect to the excitation are reported in Fig. 35a as red and black lines, respectively. A sizeable intensity imbalance in observed in the polarized PL components demonstrating the successful generation of an out-of-equilibrium spin population through optical means.

Figure 35b shows the QW transitions at 4 K and at a fixed excitation power density of 3.40 kW/cm^2. A field-induced monotonous reduction in the emission intensity is observed in the direct transition being accompanied by a redshift of the peak. This experimentally confirming the presence of QCSE [137, 164, 204]. When the electric field varies from 0 to -31.4 kV/cm (-8 V) the resulting energy shift is of about 6 meV. By changing the illumination power density no significant change is found in the peak shift due to the QCSE, although a monotonic redshift in the peak position is visible as the power is increased (Fig. 36a). This effect stems from the bandgap shrinkage originating from laser-induced heating. We extract the peak shift from our calculation and compare it with our experimental results, finding a satisfactory agreement (see Fig. 36b). For comparison results from tight-binding calculations are shown as well in Fig. 36b (gray line) [172]. The temperature effects on the peak position and on the QCSE are shown in Appendix C where results from 4 to 125 K are reported.

The study of the QCSE on carriers dwelling at the zone edge poses interesting and fundamental questions on how the electric field couples to phonon-mediated transitions. This process presently remains mostly unexplored from an experi-

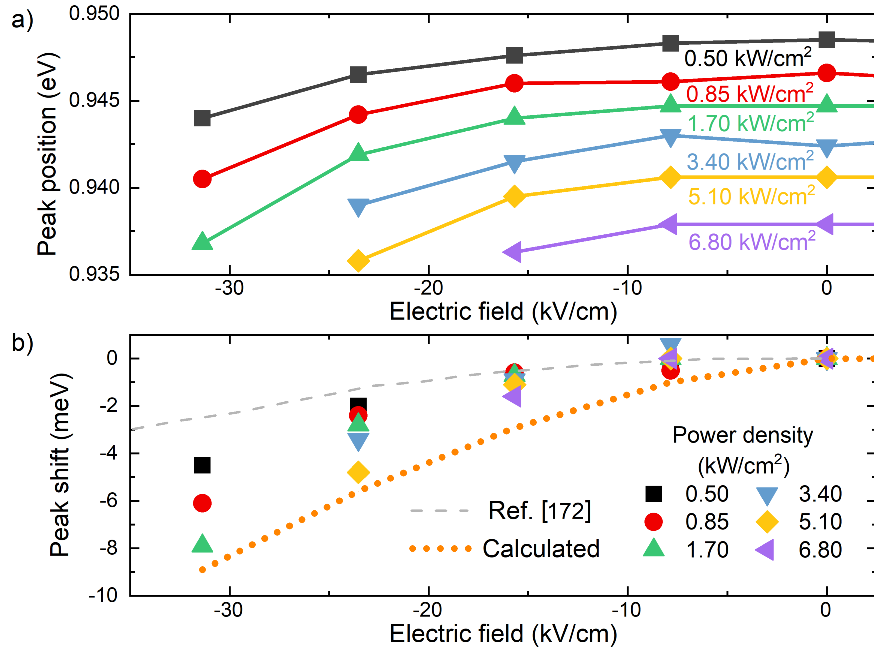

Figure 36: (a) PL peak position as a function of the electric field for different illumination power densities. (b) Shift of the peak with respect to the value extracted at 0 kV/cm for each illumination condition. The orange dashed line represents the outcome of the simulation while the gray line represents the calculation performed on a similar device with a tight-binding approach [172]. In our case 1 V = 3.9 kV/cm. A 1 meV error bar can be considered a reliable estimation of the positioning error of the peaks.

mental and a theoretical point of view. We observe in Fig. 35b that the electric field causes a loss of PL intensity both for the LA and for the NP indirect transitions. Additionally, also the defects tail undergoes a loss of the spectral weight, which anticipate a suppression of the carrier recombination rate from the defects states.

Due to the presence of the defect tail we first perform a linear fit of such contribution between 0.675 and 0.820 eV and remove it from the spectrum; then the ratio between the two components is evaluated and reported in the inset of Fig. 35b. Surprisingly, we find that the bias suppresses more easily the emission from

the LA replica than the NP emission (see inset of Fig. 35b). This suggests that the electric field plays an important role in the momentum conservation of transitions involving phonons [cL1–HH1 (LA)] rather than structural imperfections [cL1–HH1 (NP)]. We can explain such phenomena as two concomitant effects: the enhancement of the NP transition due to shift of the electron wavefunction towards the interfaces, superimposed to the depopulation of L-valley states. This second effect arises from the bias-reduced confining potential at the band-edge states (see Fig. 34b) which favours the tunneling of carriers out of L valley.

The indirect emission additionally shows another unexpected behaviour that is then fact that no energy shift of the peak is found in both LA and NP transitions. All these findings do not find correspondence in the well-established literature of QWs based on III-V compounds and call for the need of a dedicated theoretical and experimental analysis to explore the physics of electron-phonon interactions under the perturbation of an electric field.

As described in Ch. 2.1, the application of an external electric field can result in the tuning of the Rashba field with interesting consequences on the spin degree of freedom. For this purpose we leverage optical orientation to generate an out-of-equilibrium spin population, then via polarization-resolved PL we gather access to the impact of an external bias on the spin-dependent properties.

We now focus on the ρ_{circ} analysis (see Ch. 3) and begin the discussion with the direct gap transition under CW excitation when the illumination power density is varied.

For the case of zero external bias (red squares in Fig. 37a) we observe that the increment of the pump power results in an upsurge of ρ_{circ}, which is then followed by a very smooth decrease for power densities higher than 2 kW/cm^2. This last effect is ascribed to the activation of the spin-relaxation mechanism due to electron-hole exchange interaction [25], namely Bir-Aronov-Pikus mechanism, as well as a laser-induced thermal heating of the sample. This slight loss of polarization is found also for the indirect transitions (open marks in Fig. 37a) in the high-power regime, thus suggesting that similar mechanisms occur for the two

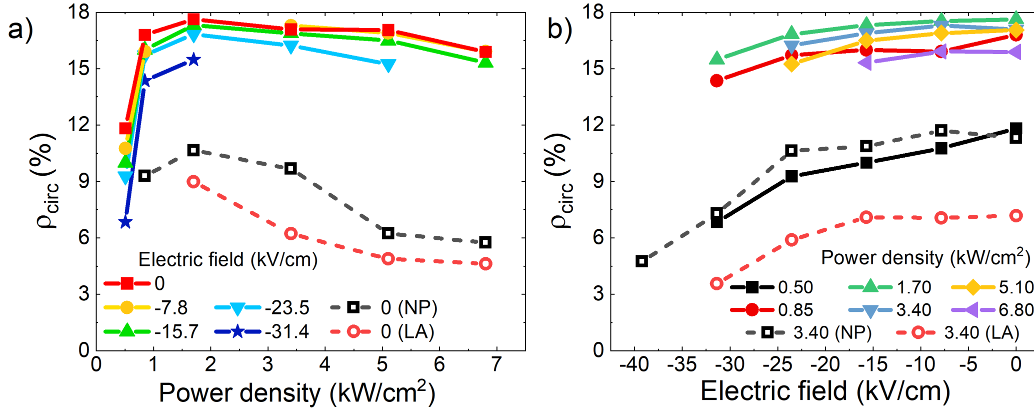

Figure 37: (a) Degree of circular polarization (ρ_{circ}) for different illumination conditions and biases. (b) Degree of circular polarization at different electric fields when a specific illumination condition is selected. Full marks are for the direct transition while open marks are for the indirect transitions. All data are obtained at 4 K. Here 1 V = 3.9 kV/cm. The uncertainty of ρ_{circ} data is 0.5 %.

spin-polarized populations at Γ and L valleys. Due to the presence of the defect tail that extends into the spectral region of the indirect peaks (see Fig. 35a), the same baseline subtraction as described above is performed before evaluating the ρ_{circ} of the indirect transition. Due to the low signal-to-noise ratio no investigation was possible in the low power regime for the zero-phonon transition and its LA replica. In the high illumination regime, the indirect emission shows a faster loss of polarization when compared to the direct transition. This can be ascribed to the fact that, according to Eq. 21, ρ_{circ} depends on the ratio τ_s/τ. Consequently, for a given τ_s, the longer τ of the indirect transition compared to the direct one causes a faster depolarization.

As pointed out above, the cΓ1-HH1 direct transition manifest a surprising increment of the polarization in the low power regime. This can be attributed to the modulation of the Rashba field by the interplay between the built-in potential of the p-i-n device and a potential arising from the photogenerated carriers. Indeed at dark, SIA introduces a Rashba field, whose magnitude is determined by the gradient along the growth direction of the static potential generated by the

asymmetric doping of the device. When light is turned on, a vast majority of the photogenerated electrons at the direct gap scatters out of the Γ valley thanks to the strong electron-phonon coupling and accumulates at the L valleys [205, 206]. On the contrary, holes are left behind at the zone centre, since the Ge VB has a single maximum at Γ. Here, holes eventually thermalize via the fast intravalley scattering within the HH band, which occur on a timescale of approximately 600 fs [207]. It should be noted that the built-in voltage separates the charge carriers causing a reduced recombination probability, as the overlap between the carrier wavefunctions is reduced. As a result, the long carrier lifetime in the L valley typical for the indirect nature of the bandgap of Ge [136], favours the accumulation of charges withing the heterostructure. Eventually, such L-valley electrons screen the built-in electric field experienced by the Γ-valley electrons responsible for the polarization of the cΓ1-HH1 transition. By increasing the power density of illumination, that is by changing the number of piled-up carriers, the effectiveness of this process can be tuned. In our case the increased power density of illumination leads to a stronger screening of the Rashba field. This results in a reduced mixing of the orbital character of the wavefunctions and, thus, into a higher polarization of the cΓ1-HH1 emission [48]. The monotonic rise of the ρ_{circ} in the low optical pump regime resembles the field dependence of ρ_0 originally calculated for asymmetric Ge/$Si_{1-x}Ge_x$ QWs in Ref. [48].

It is worth noting that the ρ_{circ} derived from the direct cΓ1 – HH1 PL peak is known to be determined by spin-polarized electrons occupying the CB Γ levels [208]. Indeed, the contribution from HH spins can be neglected because of the fast depolarization caused by parity-conserving scattering from higher-energy LH states [78, 208].

As described by Eq. 21, the polarization is proportional to the polarization at the instant of photoexcitation (ρ_0) and depends on the ratio between the electron lifetime and the spin relaxation time. For this purpose, the direct transition can be leveraged as a convenient tool to assess ρ_0. This is possible since the fast intervalley scattering driven by electron-phonon interactions, being of hundreds of

femtoseconds [30], turns out to be vanishingly small compared to the electron spin relaxation (τ_s ~ few μs [25]). Consequently, the variation in the direct cΓ1–HH1 polarization is not affected by the electric field modulation of τ_s, but rather offers a way for unveiling the impact of the electric field on the optical spin orientation process [48].

To measure the direct effect of the electric field on the polarization we fix the excitation pump and measure the ρ_{circ} when an external bias is applied (see Fig. 37). By increasing the electric field from 0 to ~30 kV/cm we observe a reduction of the polarization both for the direct as well as the indirect transition, which is in line with the theoretical prediction of Ref. [48]. Interestingly, we see from Figs. 37a and b that the dominant factor that modifies the polarization is the photo-injection of carriers and not the application of an external bias. Such optical effect demonstrates to be robust in the investigated bias range, i.e., over more than ~ 30 kV/cm. These results proves the possibility of dynamically control the spin and orbital mixing of the electron wavefunction induced by the Rashba effect, thus providing an active way to optically engineer the spin population.

Owing to the relatively long carrier lifetime of the NP cL1–HH1 transition, we can further investigate the carrier dynamics by performing TRPL analysis. In Fig. 38a we report the polarization-resolved decay curves of the NP peak measured at 4 K and at different excitation densities. Each co-polarized curve is normalized and superimposed to the laser pulse curve (see Fig. 38b). The latter is obtained by measuring the decay at an energy of 0.945 eV, that is the energy of the cΓ1-HH1 direct transition. The faster dynamics at the zone centre with respect to the laser pulse width (~ 15 ns) prevents us from studying the dynamics of the carriers in such valley, yet it can be exploited as a probe for the characteristic of the laser pulse.

For each curve of Fig. 38a, no single exponential behaviour is found but two components are required for the description of the decay curves. We find a decay characterized by a short effective lifetime (τ_{indirect}) of approximately 14 ns. By comparing our results with literature data we ascribe this transient feature to the

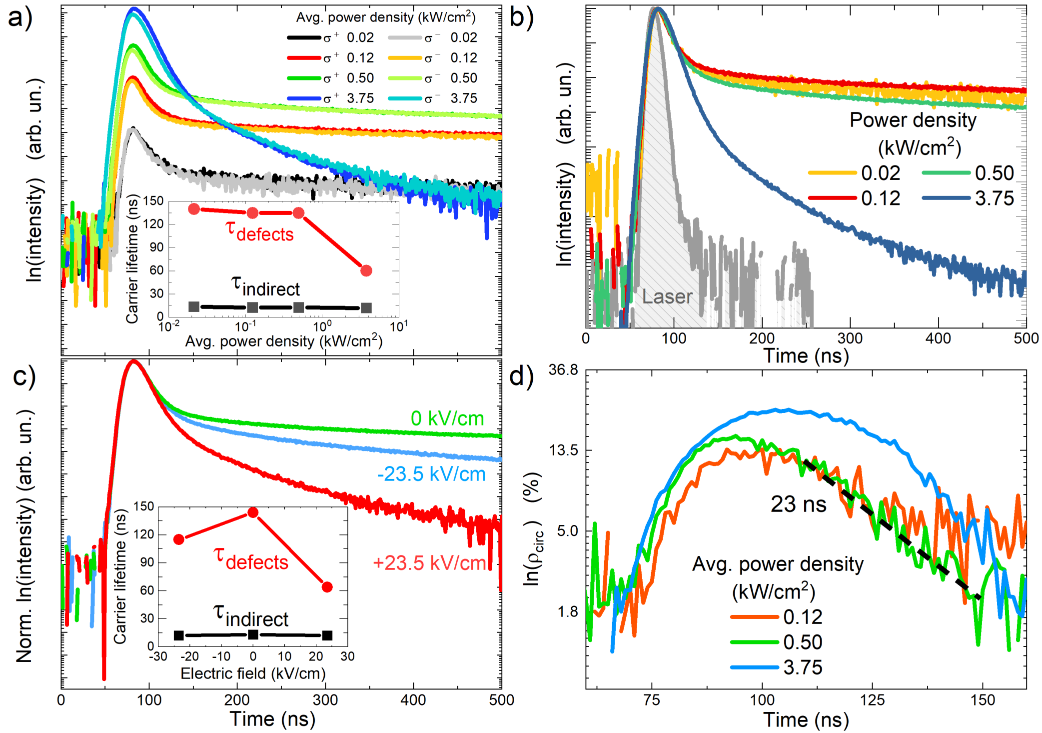

Figure 38: (a) Right (σ^+) and left (σ^-)-handed circularly polarized decay curves measured at 0.758 eV (1636 nm) at null external bias. Different power densities of the excitation are reported. In the inset we report the extracted carrier lifetimes from indirect and defects transitions obtained from double exponential fits performed on the average of σ^+ and σ^- curves for each illumination condition. (b) σ^+ decay curves at different power densities. The laser shape reported is obtained by measuring the decay at the energy of the direct transition where the dynamics is limited by the laser pulse width of approximately 15 ns. (c) σ^+ decay curve at various field applied under an illumination of 0.50 kW/cm^2. (d) Decay curves of ρ_{circ} extracted for each power density. The lowest excitation is not reported for clarity as no polarization is found. A tentative linear fit for the 0.50 kW/cm^2 case is reported with an extracted spin relaxation time of 23 ns.

recombination processes occurring via the indirect gap [136]. A slowly decaying term emerges as the first component loses intensity after few tens of ns from the laser pump. The origin of this tail can be found in the slower recombination processes of the defects states, which are characterized by a lifetime (τ_{defects}) of approximately 150 ns. Aside from the expected increased intensity, the pump power strongly affects only this second component, resulting in a significant shortening of τ_{defects} down to roughly 60 ns (see Fig. 38a and its inset). On contrary, the indirect transition remains unperturbed by the illumination condition.

No trivial explanation can be made for this unexpected acceleration of the kinetics. However relying on the dislocation barrier model [209] we can put forward the following explanation. Changes in the electrostatic potential between the charged defects and the encapsulating matrix can be either caused by an external electric field or by any redistribution of the charge density upon illumination. Such a mechanism can modify the local confining potential in the neighboring of the defect site and can inhibit its function as a recombination pathway. We point out that the present findings do not allow us to discriminate whether such phenomenon can be due to a reduced capture cross-section of the defects rather than the activation of non-radiative Auger recombination following a rapid filling of the density of states of the traps. We can nevertheless find reassurance of the proposed physical picture from the study of the PL decay when an electric field between the contact leads is established. Figure 38c shows that also in this case, τ_{defects} consistently decreases upon the application of an external bias, whereas τ_{indirect} remains unaffected.

The helicity-resolved analysis presented in Fig. 38a offers also an additional information on the spin-dependent phenomena developing in our QWs system. Within the investigated range a stronger illumination resulted in a widening of the gap between the two polarization-resolved components, indicating the formation of a more polarized electron spin population. This effect is consistent with the extracted polarization degree as shown in Fig. 38d. Due to the negligible polarization for the lowest power pump, we have not reported the data at 0.02 kW/cm^2.

Remarkably, the maximum of ρ_{circ} increases from 13 to 22%. Due to the simultaneous presence of two decaying channels, the unpolarized contribution from the defect tail can be detrimental for the extracted value of the polarization for the indirect transition. However we expect such term to be minor at the initial phase of the decay dynamics and thus not to significantly modify the maximum value of the polarization. The transient curves of ρ_{circ} consistently unveil a non-trivial decay, possibly due to the concomitant contribution from the defect states. This prevents us from properly modeling the spin evolution in order to extract reliable values of the spin relaxation time. A complex activation of the underneath contributions is also the cause of the maximum shift observable in Fig. 38d. Neverthless, we tentatively fit our cleanest curve obtaining τ_s of about 23 ns at zero bias under an excitation power density of 0.50 kW/cm^2 (dashed line associated to the green curve of Fig. 38d)

The results are in full agreement with the optical modifications of ρ_0 inferred from the steady-state measurements of the cΓ1-HH1 polarization (Fig. 37). This further supports our analysis and makes a stronger case for the suggested optical control of the Rashba Hamiltonian of asymmetric Ge/$Si_{1-x}Ge_x$ QWs, thus opening new perspectives for spin control in future semiconductor spintronic devices.

10 Emergent SOC phenomena in $Ge_{1-x}Sn_x$ heterostructures

Alloying Ge with Sn can further enrich the spin physics of germanium, since tin possesses a stronger spin-orbit coupling and it offers a new degree of freedom to tune SOC. Up to now, very little is known about the spin properties of $Ge_{1-x}Sn_x$ alloys. Some results have been obtained by electrical transport measurements [35, 36] but very few optical investigations are found in literature [196]. The main limiting factor is the infrared optical window of the material which is difficult to investigate via means of time-resolved optical techniques due to the lack of efficient detectors at those wavelenghts. Time-correlated single-photon counting using a superconducting nanowire detector is the core method for this kind of measurement. To our knowledge the record investigated wavelength is 2065 nm, in Ref. [196]. This is manifested in the inability of achieving an easy and direct access to the carrier and spin dynamics alike. Another technique that can be exploited for the study of narrow bandgap semiconductors is the time-resolved up-conversion spectroscopy [210–212]. This method uses nonlinear optics to mix the emission signal to a pump laser, generating an output at a frequency that is given by the sum of the frequencies. This could in principle bring the $Ge_{1-x}Sn_x$ signal in a more accessible spectral window, where it can be coupled to a time-resolved apparatus to study the carrier kinetics. Nevertheless, to avoid expensive equipment, complex techniques and to widen the optical window to longer wavelengths we have focused our efforts towards a continuous-wave method by fruitfully applying the magneto-optical technique described in Ch. 4.

This chapter presents an all optical study of $Ge_{1-x}Sn_x$ alloys that exploits CWPL. In particular, the first part focuses on undoped epilayer samples where we investigated the spin lifetime by means of the Hanle effect (see Ch. 4). Then we move to modulation-doped $Ge_{0.91}Sn_{0.09}$ QW where we performed a more fundamental study due to the novelty of the system.

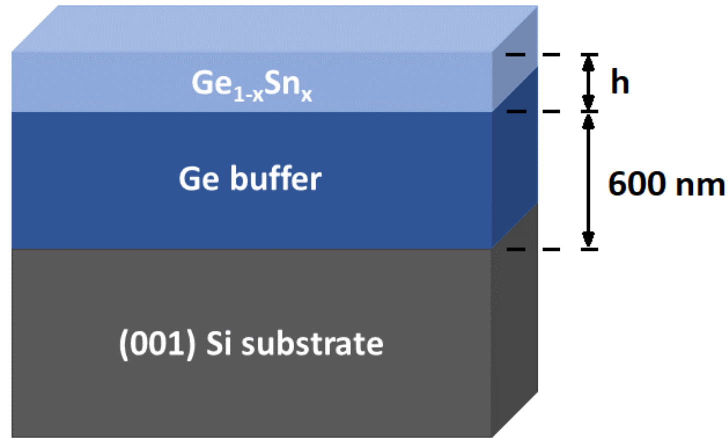

Figure 39: Schematic representation of the $Ge_{1-x}Sn_x$ epilayer samples. The $Ge_{1-x}Sn_x$ thickness h is reported in Table. 3.

10.1 Recombination dynamics in $Ge_{1-x}Sn_x$ epilayers

In this part of the thesis we investigated six $Ge_{1-x}Sn_x$ samples that have been grown with increasing the Sn content from 2 to 10 %. An additional Ge buffer layer sample was also added to the set as a reference sample.

The first step of the growth consists in the deposition of a strain-relaxed germanium buffer layer on Si (100) with a thickness of 600 nm. $Ge_{1-x}Sn_x$ films are grown on the Ge buffer layer at a temperature of approximately 270 °C using $SnCl_4$, Ge_2H_6 as gas precursors in an H_2 atmosphere. A schematic representation of the sample is shown in Fig. 39. The Sn content and the epilayer thickness are measured by XRD and are reported in Table 3. Growth and XRD are carried out by the Nano-Silicon research group of The University of Warwick.

At first, $Ge_{1-x}Sn_x$ epilayers are studied by means of CWPL at 10 K. The illumination is performed by a circularly polarized Nd:YVO_4 laser (1.16 eV) with an optical power density of 3.46 kW/cm^2. The obtained spectra are shown in Fig. 40 after normalizing the intensity. All curves, except for the gray one, are taken in co-polarization with respect to the excitation.

The reference Ge buffer layer shows a high-energy PL peak at ~0.85 eV (black

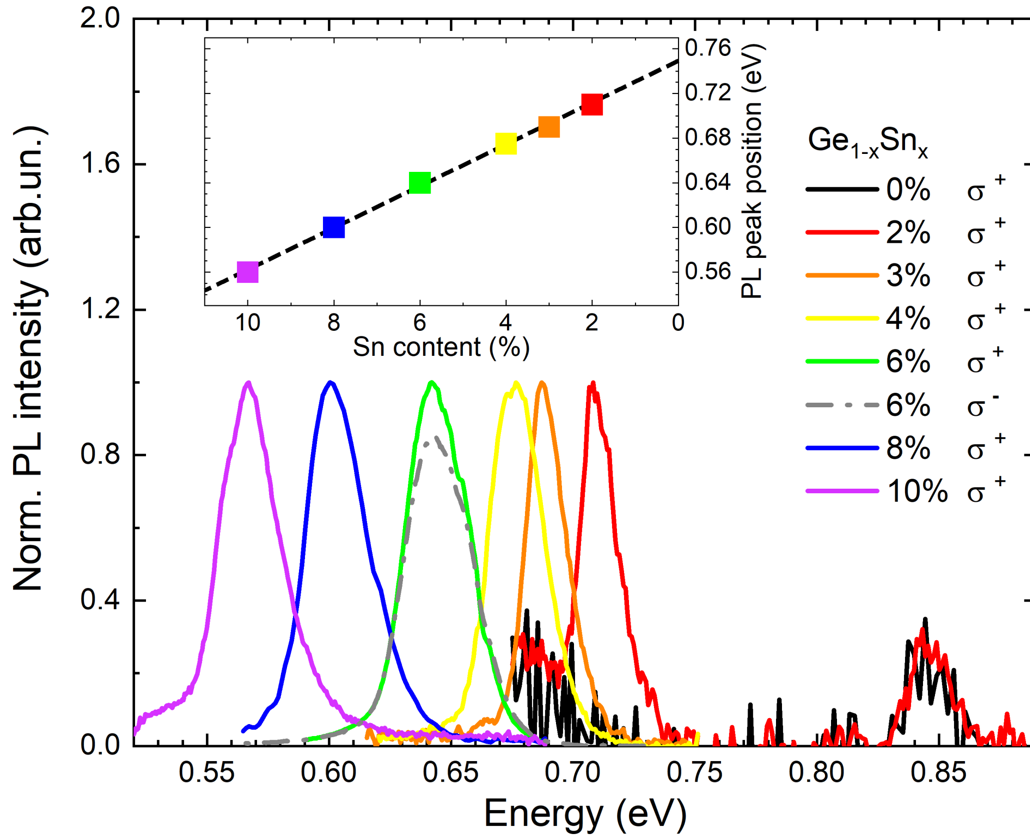

Figure 40: PL spectra obtained at 10 K of $Ge_{1-x}Sn_x$ with x ranging from 0 (Ge buffer, black curve) to 0.10 (violet curve) in the co-polarization configuration under a 1.16 eV laser excitation with a power density of 3.4 kW/cm^2 and a spot diameter of 50 µm. The gray dash-dotted line is obtained from σ^- emission counter-polarized to the excitation and normalized for the same value of the σ^+ counterpart. This shows that optical spin orientation can be achieved. The inset shows the energy of PL-peak maximum as a function of the Sn content. The dashed line is a linear fit of the data. The uncertainty is smaller than the symbols size. Adapted from [213].

Sn content (%)	h (nm)
2	150
3	45
4	35
6	70
8	40
10	40

Table 3: Structural properties of $Ge_{1-x}Sn_x$ layers grown coherently on the almost relaxed Ge buffer, whose residual biaxial tensile strain stems from the difference in the thermal expansion coefficient with respect to the Si substrate. The thickness h of each layer have been experimentally determined from XRD data.

line), corresponding to the direct bandgap recombination [214–216]. This feature is still observable in the sample with 2% of Sn (red curve) but an additional structure emerges at approximately 0.71 eV. This peak is attributed to band-to-band recombination events and it shows a redshift by increasing the Sn content reaching 0.56 eV for $Ge_{0.90}Sn_{0.10}$, as expected from alloying Ge with Sn as well as by increasing the compressive strain in the epilayer [217, 218]. In the inset of Fig. 40 this reduction of the bandgap is extracted and plotted. A linear fit is outlined (dashed curve). This gives an intercept at about 0.75 eV at $x = 0$, which is consistent with the energy expected at low temperature for the optical transition through the indirect bandgap of bulk Ge [219]. This suggests that all the observed peaks of our coherent $Ge_{1-x}Sn_x$ films originate from the indirect-band-gap recombination. This interpretation is also in line with the Γ-L hybridization of the conduction-band edge pointed out in Ref. [220, 221] as well as with the presence of the compressive strain due to the pseudomorphic growth which pushes further the indirect-to-direct transition. We point out that, despite maintaining the indirect nature, our samples manifest the presence of the direct transition. Indeed, the PL signal shows a monotonic broadening of the peak which can be attributed to the approaching of the direct transition as Sn content is increased. This effect is in line with what observed in literature [222].

Optical spin orientation is then leveraged to achieve a out-of-equilibrium spin population, enabling the investigation of the spin-related properties via polarization-resolved PL (see Ch. 3). In Fig. 40 the cyan (solid) and gray (dash-dot) lines are an example of the recorded spectra for the $Ge_{0.94}Sn_{0.06}$ in co- and counter-polarization with respect to the excitation. To show the different PL intensity between the two configurations both curves are normalized by the maximum value of the co-polarized curve. The extracted ρ_{circ} for all samples is found to be approximately 12 %, demonstrating successful optical spin orientation.

To extract fundamental information on the spin dynamics a time-resolved measurement is the ideal choice since it gives direct access to the lifetime. However, we have to consider that the PL emission range of our samples is in a challenging infrared window (~2 μm), where time-resolved techniques are hard to be applied due to the lack of efficient and affordable detectors. Therefore, the direct measurement of carrier and spin lifetime is difficult to be implemented and other approaches would be desirable for the study of the kinetic parameters. As we have seen in Ch. 4, the Hanle effect can be exploited with CWPL to extract the spin lifetime information. Here we introduce this technique in the context of group-IV materials, which have been so far overlooked due to their indirect bandgap nature.

To perform the measurements, we set the magnetic field perpendicular to the spin quantization axis in the so-called Voigt configuration. We analyze data spanning the magnetic field from 0 to 110 mT and the results are shown in Fig. 41a (a color-coded map of the PL intensity profile, from which we extracted ρ_{circ} via Stokes analysis, is shown in Appendix C). All data are normalized and then mirrored to negative values to better emphasize the Lorentzian shape of the curve. We observe that the width of the curve is narrowest for the $Ge_{0.94}Sn_{0.06}$ sample where the depolarization occurs at about 20 mT. On the contrary, the widest one is found for $Ge_{0.90}Sn_{0.10}$ (the sample with the highest Sn content investigated) where the explored field range is not sufficient to wash out the polarization.

The sizeable ρ_{circ} observed for all the samples under nonresonant excitation and in absence of the external magnetic field implies that $\tau_S > \tau$ and hence, from

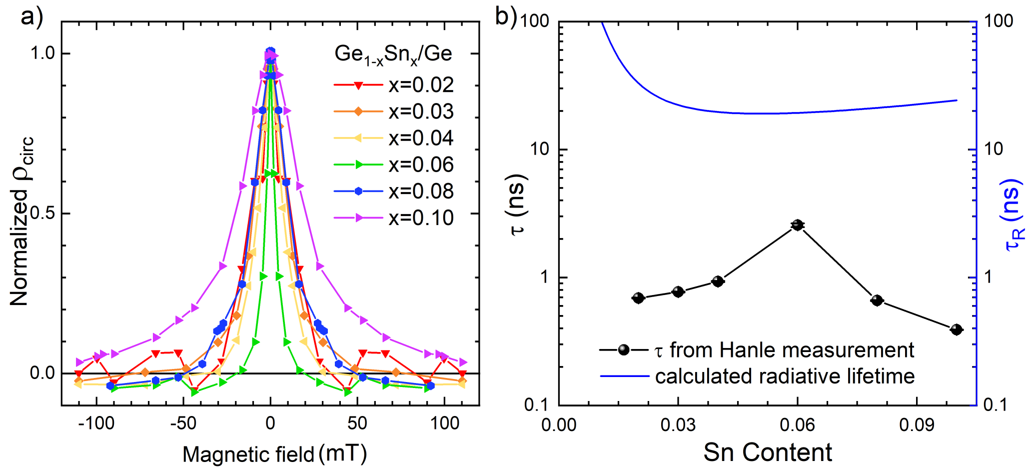

Figure 41: (a) Low temperature (10 K) circular polarization degree ρ_{circ} as a function of a transverse magnetic field (Hanle curve). Data are normalized with respect the maximum ρ_{circ} of each sample and mirrored to negative magnetic fields to better emphasize the Lorentzian character. Measurements are carried out under a 1.16 eV laser excitation with a power density of 3.4 kW/cm^2 and a spot diameter of 50 μm (b) Carrier lifetime τ as a function of Sn content (black data), obtained by assuming $g = 1.48$ for all samples (see the text for more details on this assumption) and $T_S \simeq \tau$, where T_S and τ are the spin and the carrier lifetime, respectively (see Eq. 25) [196]. The error bar is obtained by propagating the error of approximately 0.2 mT, associated with measurement of the magnetic field, from Eq. 27. The blue curve shows the direct radiative lifetime τ_R estimated via the model theoretical calculation outlined in the Supplementary Information of Ref. [213].

Eq. 25, that $T_S \simeq \tau$ [223]. This assumption was verified experimentally in a $Ge_{0.95}Sn_{0.05}$ sample exhibiting spin relaxation time $\tau_s = 10$ ns and carrier lifetime $\tau = 2$ ns [196]. It is worth noticing that all the $Ge_{1-x}Sn_x$ samples examined are grown pseudomorphically on the Ge-on-Si substrate and thus possess a built-in compressive strain. The optical transitions observed in our PL experiments thus allow us to gain access to the dynamics of spin-polarized electrons dwelling within the L valleys.

Equation 27 can thus be used to extract the carrier lifetime by measuring the FWHM of all curves. The results of the carrier lifetime are reported as black dots in Fig. 41b. In the estimation we assumed a constant g-factor value of 1.48, which is the only available data in literature for $Ge_{0.95}Sn_{0.05}$ alloy [196]. Actually, this value is expected to smoothly decrease with Sn content from the pure-Ge system of 1.6 [25, 224–226]. However, it is most likely that the variation of the g-factor is small over the studied Sn range. This ensures that our assumption does not introduce significant changes and also suggests that the bell-like shape observed can not be ascribed to variations of the g-factor alone. Therefore, this bell-like shape can be ultimately ascribed to effects on the carrier lifetime due to the alloying with Sn.

The effective carrier lifetime lies in the order of hundreds of picoseconds and rises to 2 ns in the $Ge_{0.94}Sn_{0.06}$ sample. Remarkably, this result compares well with the lifetime value extracted from TRPL investigation [148, 196, 227] as well as with the temperature-dependent PL characteristics reported in Ref. [34], as shown in Fig. 42. This supports the effectiveness of our approach showing that CWPL coupled to the Hanle effect can be reliably applied to the investigation of the carrier dynamics within group IV materials.

To further unveil information of the dynamics we have to take into account that the measured carrier lifetime τ encapsulates both radiative (τ_R) and non-radiative (τ_{NR}) contributions according to [228]:

$$\frac{1}{\tau} = \frac{1}{\tau_R} + \frac{1}{\tau_{NR}} \tag{54}$$

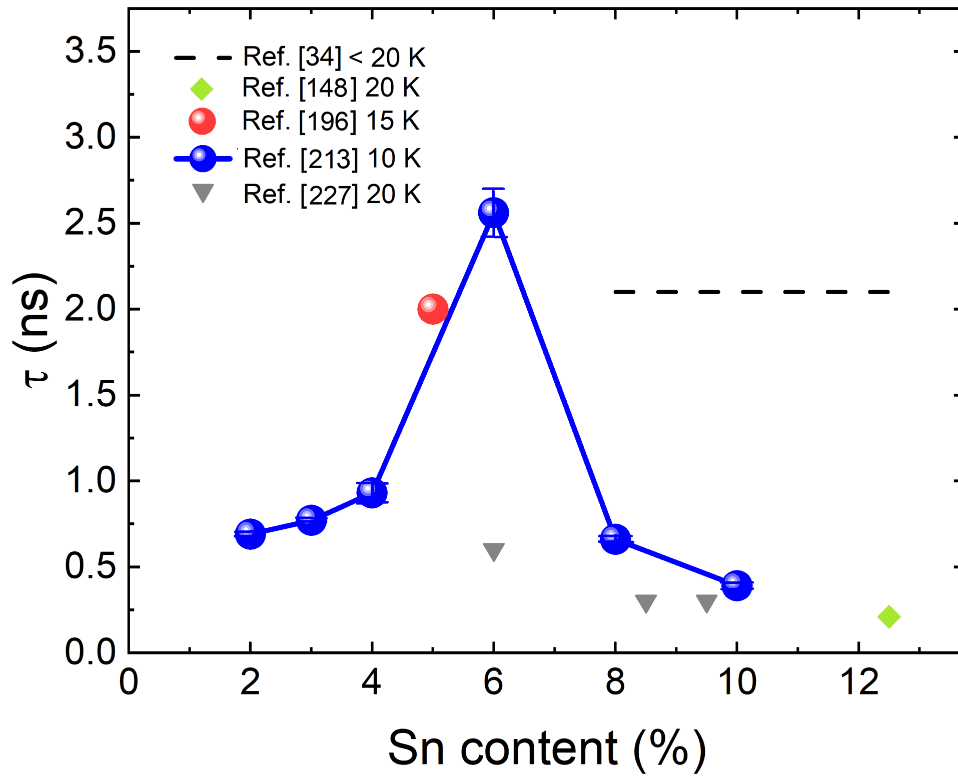

Figure 42: Summary of the carrier lifetime of $Ge_{1-x}Sn_x$ epilayer as a function of Sn content reported in literature. Connected blue dots are our results [213] while other marks are available data in literature from Refs. [34, 148, 196, 227]. The error bar is obtained by propagating the error of approximately 0.2 mT, associated with measurement of the magnetic field, from Eq. 27.

As the Sn content is increased we expect to observe a greater Γ-like character of the bandgap with a corresponding monotonic decrease of τ_R. To understand the measured behaviour of our experimental results, a collaboration with the Tyndall National Institute provided a theoretical model that was exploited to describe Sn-induced Γ-L mixing using a model Hamiltonian parametrized via atomistic alloy-supercell electronic structure calculations (details are reported in Supplementary Information of Ref. [213]). The results are illustrated in Fig 41b by the blue line. The estimation of the τ_R decreases with Sn content reaching a minimum of 19.1 ns for the case of $Ge_{0.95}Sn_{0.05}$. The model has not taken into account electron-hole recombination or emission and absorption of phonons. Since the inclusion of such effects would in any case increase the lifetime, the theoretical estimation has to be considered a lower bound on the radiative lifetime. As can be seen, the calculated radiative lifetime is approximately one order of magnitude larger than the measured values, thus suggesting that the limiting factor are the non-radiative recombination processes that are fast enough to dominate the carrier kinetics.

Since Auger recombination is ruled out by the low excess carrier density that is generated by the illumination [229], the bell-like shape is attributed to the crystal quality of the $Ge_{1-x}Sn_x$ layers and to the challenge of minimizing crystal defects during the CVD growth of the epitaxial thin film. As explained previously, the low solubility of Sn in Ge requires strong-out-of equilibrium conditions to grow $Ge_{1-x}Sn_x$ with $x > 1$ %. As Sn tends to segregate, low temperatures in the range of 200-300 °C and high growth rates are required to suppress surface diffusion and incorporate high Sn content. However, in diluted-Sn regimes the temperature has to be increased as the optimal Ge growth temperature is approximately 600 °C. A further complication arises from the fact that the compressive strain in our samples further reduces the Sn incorporation [230, 231]. If proper growth conditions are not met, point defects and Sn clustering are to be expected, thus lowering the crystal quality. Different contributions from these effects result in a non-trivial behaviour and the best condition matches at Sn content $x = 0.06$. A better optical quality results in a lengthening of the effective carrier lifetime for this particular

h (nm)	R (%)	δ (μm^{-1})
40	0	0
50	0	0.2
60	0.6	0.59
80	6	2.28

Table 4: Structural data of $Ge_{0.92}Sn_{0.08}$ epilayer on Ge-on-Si substrate with different layer thickness h. The relaxation (R) is experimentally determined from XRD data, and the linear dislocation density δ is derived from TEM images [213].

Sn fraction, causing the observed upsurge of τ and, consequently, the bell-shaped curve of Fig 41b.

To further investigate the role of the strain on the carrier dynamics, a second set of samples with varying thickness is analysed. This gives access to non-radiative recombination pathways introduced by the nucleation of dislocations due to plastic strain relaxation. For this purpose four samples with a Sn content of 8% and an active layer thickness (h) varying from 40 to 80 nm are studied. The samples are characterized via XRD, reported in Fig. 43, for the thickness measurement and transmission electron microscopy (TEM) images for the estimation of linear dislocation density (δ). The results are summarized in Table 4. Since the strain relaxation of the 50-nm-thick sample is below the experimental sensitivity, we estimated δ from the quadratic fit of the TEM results. This is shown in Fig. 44 where we reported the TEM data in blue dots, the parabolic fit as a gray line and the extracted value as a red square.

In the inset of Fig. 45a we show low-temperature PL spectra. We find that the PL intensity scales inversely with the epilayer thickness, so the 80-nm-thick film manifests the weakest PL signal. The suppression of the emission unveils the emergence of non-radiative recombination channels ascribed to the nucleation of dislocations at the GeSn/Ge interface. By increasing δ, that is by increasing the epilayer thickness, we observe a broadening of the Hanle curves reported in Fig. 45a which implies a reduction of the effective carrier lifetime τ as illustrated

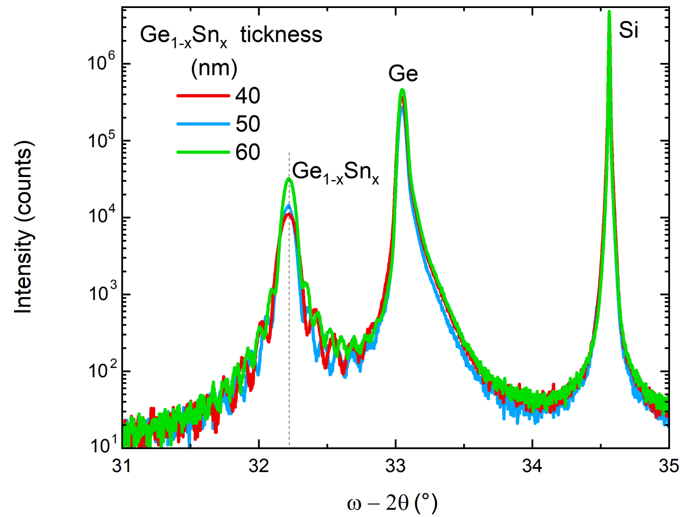

Figure 43: High-resolution XRD $\omega - 2\theta$ scan of $Ge_{1-x}Sn_x$ epilayers with three different thicknesses: 40 (red), 50 (blue) and 60 nm (green). The well-defined interference pattern of the peak at approximately 32.2° indicates that the $Ge_{1-x}Sn_x$ epilayer is fully strained.

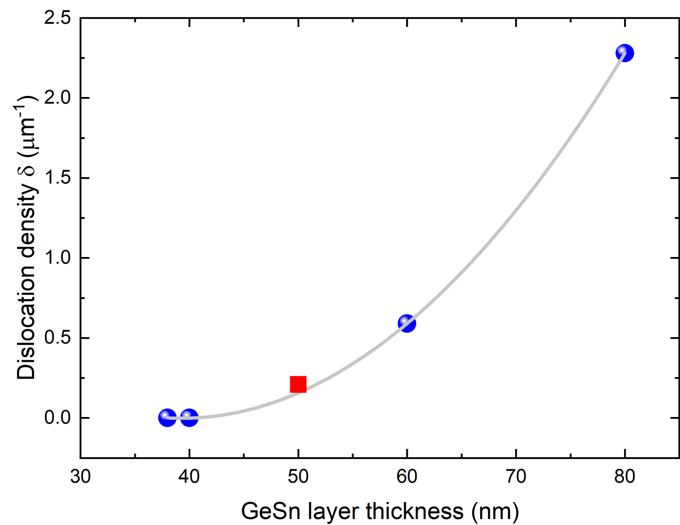

Figure 44: Linear dislocation density as a function of layer thickness for $Ge_{0.92}Sn_{0.08}$ samples. Blue dots are the TEM-measured values that show a quadratic increase with thickness, as depicted by the parabolic fit (grey line). The red square is the estimation of δ for the 50-nm-thick $Ge_{0.92}Sn_{0.08}$ sample.

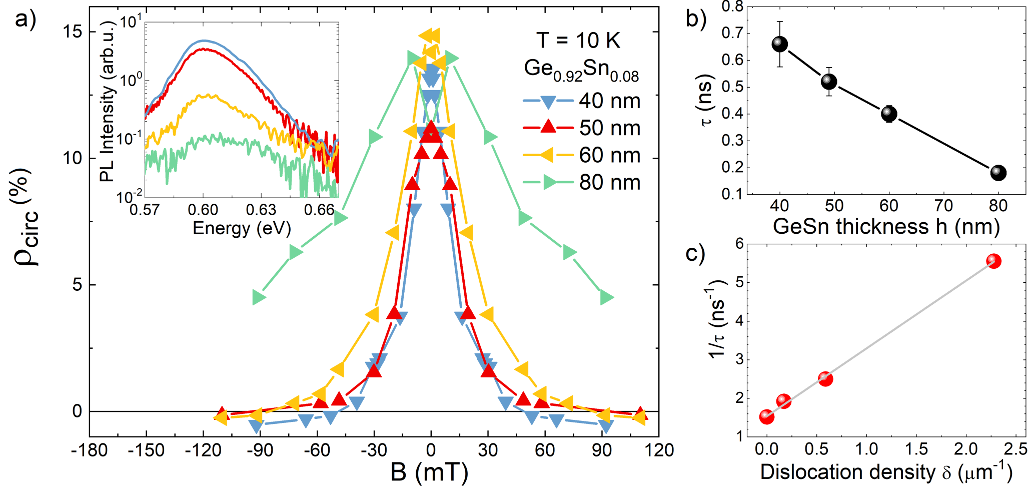

Figure 45: (a) Hanle curves of the $Ge_{0.92}Sn_{0.08}$ layers with different thickness. Hanle data are mirrored to negative magnetic fields to better emphasize the Lorentzian shape. The inset shows the low-temperature PL spectra. Measurements are obtained under a 1.16 eV laser excitation with a power density of 3.4 kW/cm^2 and a spot diameter of 50 µm. The dip observed at zero field for the 80 nm sample (green curve) is ascribed to the lower signal-to-noise ratio, with respect to the other samples, due to the low PL signal. The uncertainty on the measurement is 0.5 % except for the green data for which it is 2%. (b) Carrier lifetime τ derived from the Hanle curves as a function of layer thickness. (c) Inverse of carrier lifetime as a function of the linear dislocation density (see Tab. 4). The gray line is a linear fit, whose slope provides an estimate for the recombination velocity at the defects of $(1.77 \pm 0.03) \times 10^5$ cm/s. The error bars are within the size of the symbols.

in Fig. 45b. Here a linear reduction is clearly visible, an effect that is similar to strained III-V heterostructures [232].

To shine some light on the observed behaviour, we elaborate further on the kinetics that occurs in the presence of an increasing number of extended defects that can act as carrier sinks. At first, we notice that there can be recombination at the free surface. However, this contribution must be excluded as it has the same weight for all the samples. Then, we can consider a variation in the native oxide due to the lattice relaxation. However the latter is too small to give rise to any sizeable effect. Additionally, no effect can arise from a non-homogeneous photogeneration of carriers, since the laser penetration depth and the carrier diffusion guarantee that photogenerated carriers always distribute throughout the full thickness of the epitaxial layers [233, 234]. Finally, the number of threading dislocations that originates at the buried Ge/Si interface and pierce through the layers emerging at the top free surface is expected to be similar in all four samples. Following these considerations, the changes of the non-radiative lifetime observed in Fig. 45b can be primarily ascribed to the emergence of recombination centres at the defective $Ge_{1-x}Sn_x$ /Ge interface.

For the recombination at the defects, the following model can be applied. According to Shockley-Read-Hall statistics, it is possible to define a recombination efficiency $\sigma = 1/\delta\tau$ that describes the capture of minority carriers within the dislocations as a cause of strain and Coulomb potentials. This describes the probability that, within a mean lifetime, a photogenerated carrier sinks into one dislocation. The comparison between the experimentally accessible values of the carrier lifetime and the available dislocation sites gives an estimation of the process efficiency. By plotting the measured carrier recombination rate, obtained as the inverse of the carrier lifetime from Hanle curves, versus the linear dislocation density, obtained from the TEM analysis, we can unveil the recombination velocity. A notably linear dependence is indeed visible in Fig. 45c. This finding is in line with what observed in Si and Ge by Kurtz et al. [235, 236]. A linear fit (gray line) is superimposed to the data and the extracted slope gives an estimation

	Recombination velocity (cm/s)	Reference
Si/Ge interface	4000	[237]
	9750	[240]
Ge/SiO_2 interface	14500	[240]
iGe	85000	[239]
nGe/iGe interface	66000	[239]
iGe/GOI interface	49000	[239]
Si wafers	4000	[241]
	80-5000 [a]	[242]
SOI wafers	500-1800	[243]
$Si_{1-x}Ge_x$	300-4000 [b]	[237]
$Ge_{0.92}Sn_{0.08}$	177000	this work

[a] depending on the surface passivation process
[b] depending on the $Si_{1-x}Ge_x$ layer thicknesses and the Ge contents

Table 5: Survey of the recombination velocity for different materials.

of the recombination velocity at dislocations of $(1.77 \pm 0.03)\times10^5$ cm/s. When comparing this value with other group IV materials (see Table 5 and Fig. 46), our recombination velocity is larger by approximately 2 orders of magnitude in the case of dislocated Si-rich $Si_{1-x}Ge_x$/Si heterointerfaces [237, 238] and between 2 to 10 times for Si-Ge interfaces [239, 240]. This ultimately tells us that the carrier dynamics in strained $Ge_{1-x}Sn_x$/Ge heterostructures is limited by the crystal quality.

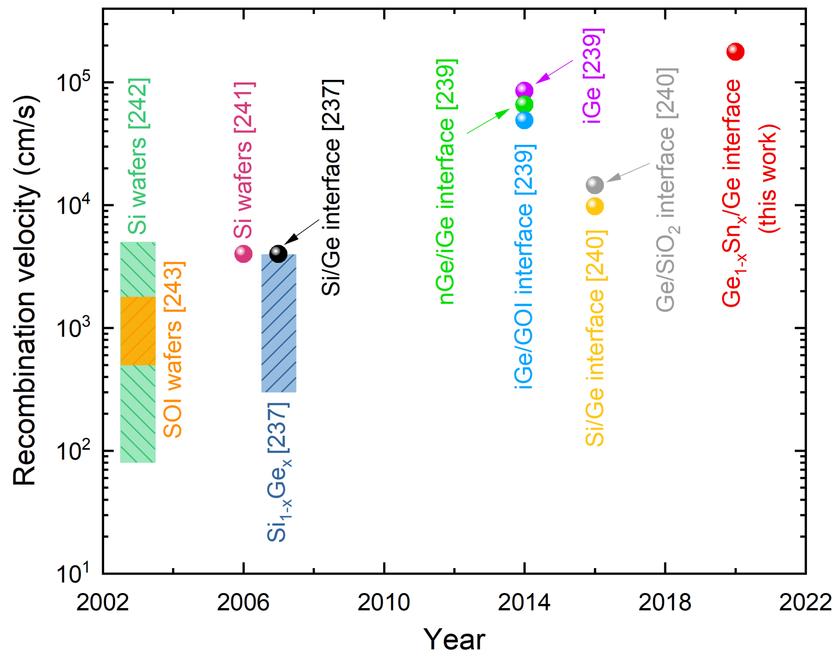

Figure 46: Recombination velocity from Table 5 versus year of published result. In the square bracket we report the reference from which we took the data. The rectangles represents a range of values. The error bars are within the size of the symbols.

Figure 47: Schematic cross section of the modulation-doped $Ge_{0.91}Sn_{0.09}$/Ge QW samples. From left to right we can observe samples S-20, S-100 and S-150, where the only changing parameter is the Ge spacer thickness.

10.2 p-type modulation-doped $Ge_{0.91}Sn_{0.09}$ quantum well

Three modulation-doped $Ge_{0.91}Sn_{0.09}$ QW samples have been grown. A 1.1 µm relaxed Ge buffer is deposited on a Si (001) substrate, then followed by 10 nm of B doped Ge layer (1.2×10^{18} cm^{-3}). Then, a single $Ge_{0.91}Sn_{0.09}$ QW is grown sandwitched between a Ge barrier, namely a spacer, of variable thickness and a topmost 50 nm Ge cap as shown in Fig. 47. The spacer has the function of varying the distance between the dopants and the well, thus offering a way to tune the electric field generated inside the material. On each sample we pattern Hall bars with different channel width via optical lithography (using the Heidelberg Instrument µPG 101 laser writer), followed by wet chemical etching (with a solution of H_2O_2 : HCl : H_2O in ratio 1:1:20). Thicknesses are extracted from XRD measurements, shown in Fig. 48.

10.2.1 Magnetotransport measurement

A magnetotransport characterization is made on our sample by a combination of resistivity and Hall effect measurements in the temperature range of 0.3 – 4 K. For this we fabricate a dedicate set of smaller Hall bars, used only for transport measurements, with a 600-µm-long and 30-µm-wide main channel. An optical image of a device is shown for S-20 in Fig. 49a.

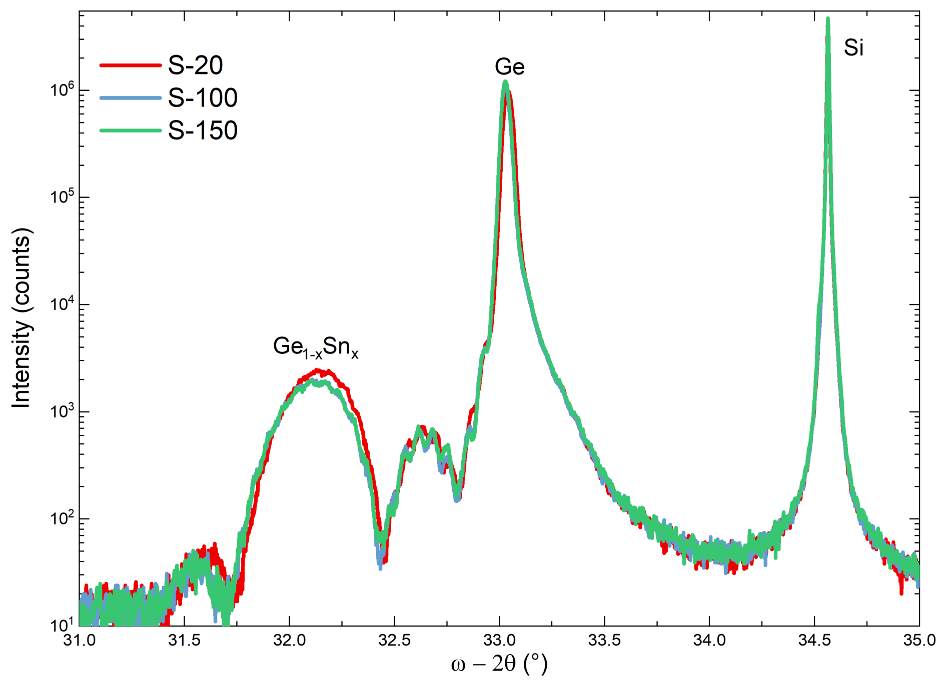

Figure 48: High-resolution XRD $\omega - 2\theta$ scan of $Ge_{1-x}Sn_x$ QW of samples S-20 (red), S-100 (blue) and S-150 (green). The interference pattern of the peak at approximately 32.2° indicates that the $Ge_{1-x}Sn_x$ layer is fully strained.

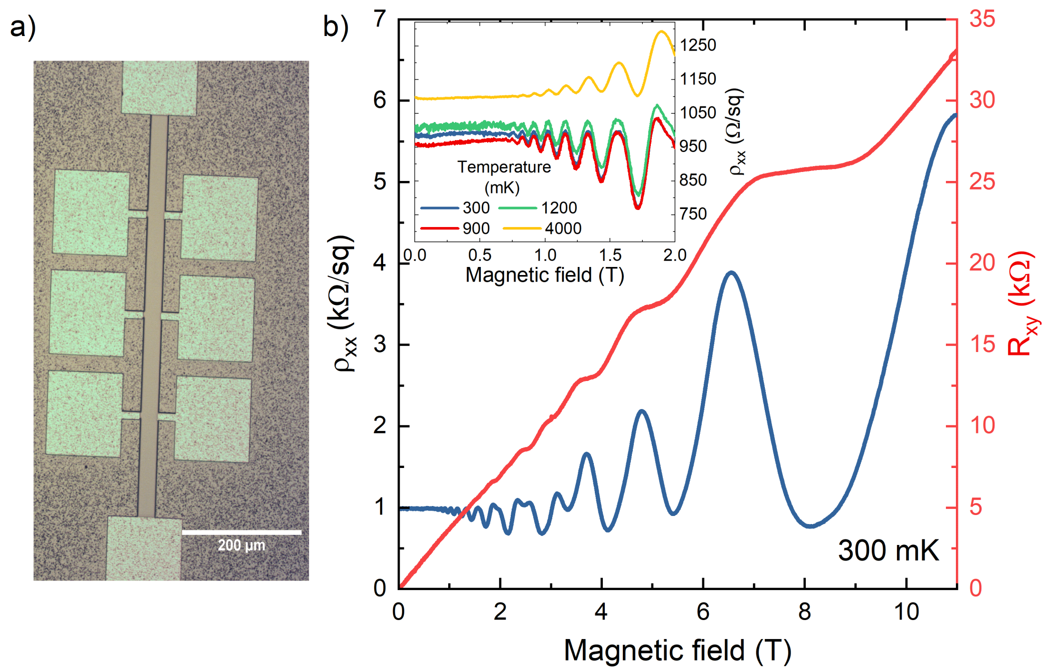

Figure 49: (a) Optical image of the device used for magneto-transport measurement. (b) Magnetotransport results for the sample S-20 at 300 mK, showing the Shubnikov-de Haas oscillations and the plateaus in the Hall resistance: fingerprint of two-dimensional hole gas formation. The oscillations are found in the whole temperature range of 0.3 – 4 K (inset). The measurements are obtained by a combination of resistivity and Hall effect measurements by sourcing 500 nA along the main channel and sweeping the magnetic field from -12 to +12 T.

Clear Shubnikov-de Haas oscillations are visible in the whole temperature range between 0.3 and 4 K (Fig. 49b and inset), confirming the formation of a 2DHG in the QW. Published results on similar structures suggest that oscillations are present up to 5 K [142] and from the clear visible pattern we speculate that the disappearance of the 2DHG may happen at even higher temperatures. At 1.95 T a second oscillation arises in the curve ascribed to the Zeeman spin splitting of HH states [142].

By restricting to the 0 - 2 T range, that is before the appearance of the second frequency, we can evaluate the two-dimensional density of carriers present in the well. The separation between two maxima in the $1/B$ plot is given by:

$$\Delta\left(\frac{1}{B}\right) = \frac{2\,e}{n\,h} \tag{55}$$

where e is the electron charge, n the two-dimensional carrier density and h is the Plank constant. From this we obtain $n = 4.2\times10^{11}$ cm^{-2}, which is in line with results reported in Ref. [142].

Magnetotransport analysis is used here as a proof of the formation of the 2DHG, while the main focus of this study is to address emergent spin-orbit phenomena using optical methods. Interestingly this system has not been studied deeply; indeed, so far, the only available data in literature on $Ge_{1-x}Sn_x$/Ge QW are transport measurements [142] and PL data for LED application in the infrared [244], while the only published result on the interplay between the strain and the SOC is reported in Ref. [36].

10.2.2 Electrical characterization

From now on we focus on the data obtained by measuring the device bonded in Fig. 50. Here we fabricated a dedicated Hall bar structures with a 4-mm-long and 200-µm-wide main channel. The need for a dedicated device to perform this kind of measurements is due to the fact that the optical measurements performed are made using an exciting laser with a spot diameter of 50 µm, thus a channel width

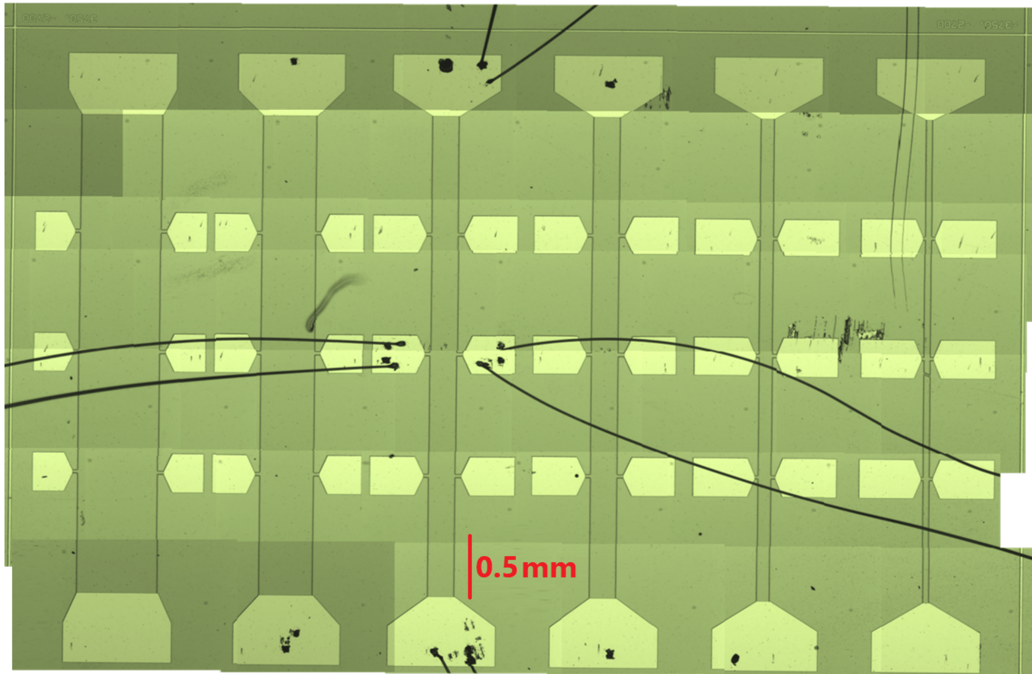

Figure 50: Optical image of the Hall bars for optical investigation fabricated on the sample S-20.

larger than the spot size is required.

An I-V measurement at 4 K in dark condition is taken by measuring this device along the main channel. The I-V is reported in the inset of Fig. 51 for the case of sample S-20. The linear response at low temperature demonstrates a good ohmic contact of the device and allows the evaluation of the resistance, which is reported in the inset as well. For results of samples S-100 and S-150 see Appendix C.

The I-V characteristic is also measured under illumination by carefully positioning the laser spot completely on the mesa. In this case the laser spot is moved along the main channel in the range -1.9 to +1.9 mm with respect to the centre of the bar (see the red line in Fig. 51a) and for each position we record an I-V trace. The resulting data are reported in Fig. 51b. An overall increased value of the current is found, which is in line with the additional contribution originating from the photogenerated carriers. The loss of the linearity in the response is ascribed

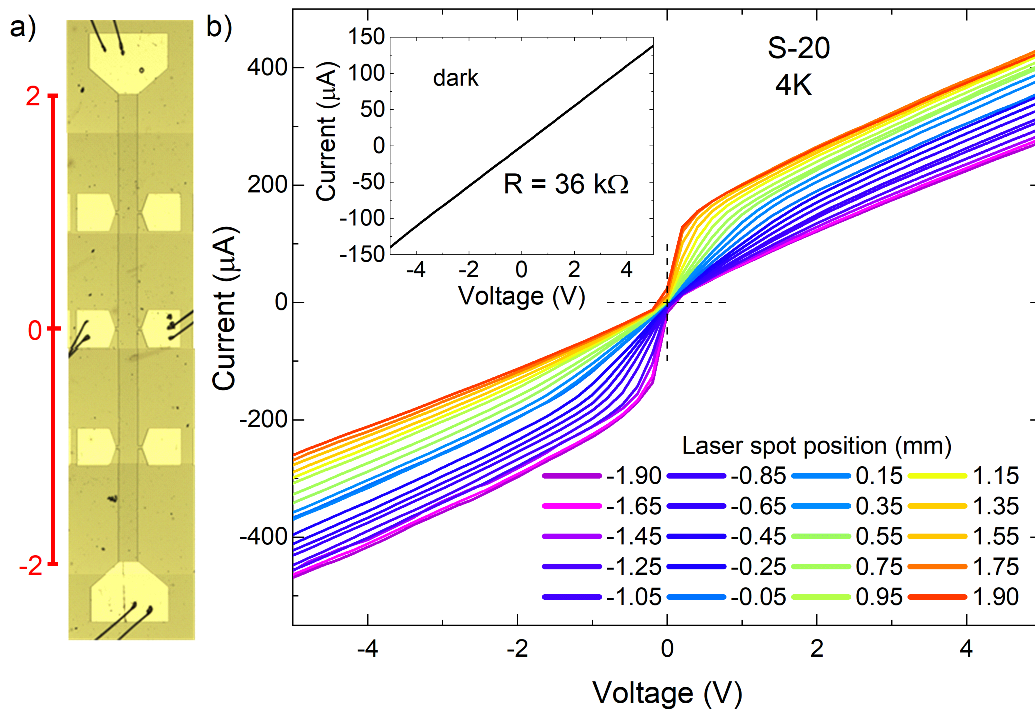

Figure 51: (a) Optical image of one device of sample S-20 that has been wire bonded for electrical measurements. (b) I-V characteristics under illumination at 3.4 kW/cm^2 of device in (a). The laser spot is moved along the channel from one contact to the other. Laser spot is 50 μm in diameter and the excitation energy is 1.16 eV.

to the local heating that likely perturbed the overall potential through Seebeck effect causing the observed bending. The I-V characteristic under illumination of samples S-100 and S-150 are presented in Appendix C.

Photocurrent (PC) is then analyzed while shining the laser along the channel. As a reference, in Fig. 52 we report the signal measured for the sample S-20. In Fig. 52a we show the PC measured at zero-bias at room temperature for different illumination conditions. We can see that the PC has opposite direction in proximity of the two contacts while at the centre of the channel the measured current is null since carriers equally drift in opposite directions. By lowering the laser pump by two orders of magnitude we observe a marked reduction and flattening of the signal along the Hall bar, further corroborating the presence of thermal contribution. We then compare the PC measured at RT and at 4 K (see Fig. 52b) and we find out that at cryogenic temperature the magnitude is reduced due to the suppression of the thermally activated population.

10.2.3 Optical characterization

In Fig. 53a we show the PL measurement conducted in a temperature range of 4-250 K. Two major features can be observed at different temperatures. From 4 to 125 K the spectrum is dominated by one peak that is located at 0.60 eV. This peak redshifts by approximately 10 meV from 0.60 to 0.59 eV at 150 K. According to what described in Ch. 7.2, the QW is under compressive strain due to the higher lattice parameter of $Ge_{1-x}Sn_x$ alloy with respect to the Ge barrier. As in the case of the epilayers discussed in Ch. 10.1, this ensures that despite the high Sn content the material possesses an indirect bandgap. Thus, this peak is attributed to the indirect bandgap recombination transition cL1-HH1.

From 150 K the, the emergence of a second peak at approximately 0.62 eV must be taken into account. However the higher magnitude of the cL1-HH1 peak at such temperature does not allow for a precise evaluation of the position of this second component. It is only from 175 K that the indirect transition loses spectral weight in favour of this second feature. The asymmetry of the PL emission from

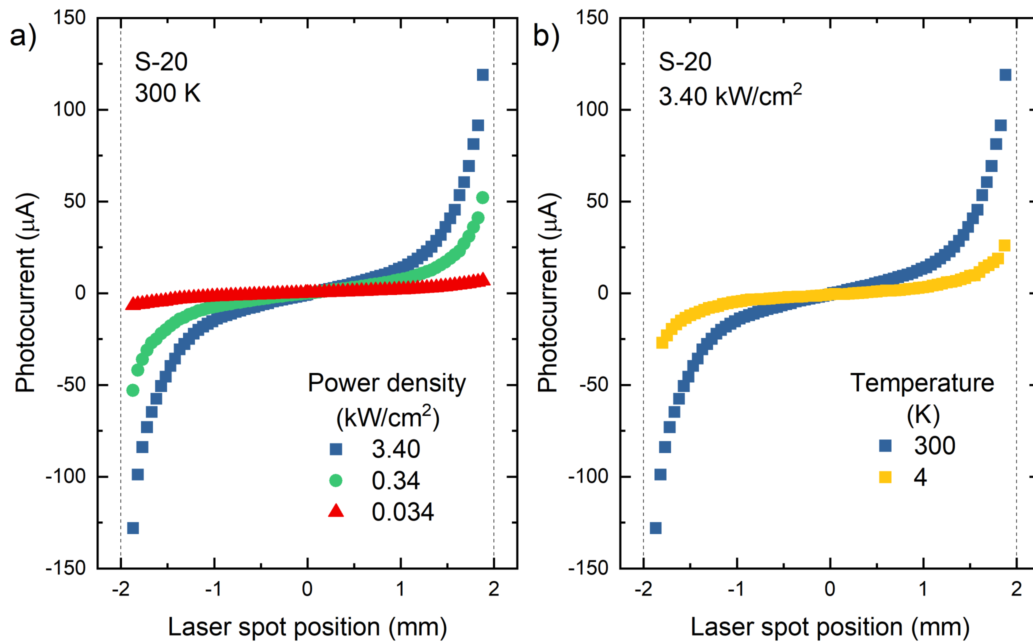

Figure 52: (a) Photocurrent measured while moving the laser spot along the main channel of sample S-20. Data at different power densities are shown at room temperature. (b) Comparison between photocurrent measured at 300 and at 4 K under an illumination of 3.40 kW/cm^2 from a 1.16 eV laser with a diameter spot of 50 μm. The dashed lines represent the position of the electric contacts. Error bars are within the size of the symbols.

50 to 250 K is likely to be originating from this second contribution. A colour-coded map of the evolution of the PL spectra is shown in Fig. 53c. We can clearly see the loss of intensity and the redshift of the cL1-HH1 peak as well as the emergence of the second peak.

In Fig. 53b we report the position of the maximum of the PL spectrum as a function of temperature showing that both peaks undergo a redshift, accordingly to Varshni's law. The origin of the second peak can be ascribed to the thermal activation of direct bandgap transitions (cΓ1-HH1) due to carriers that have acquired enough kinetic energy to be scattered back to the Γ-valley and recombine there in. In our interpretation we excluded the attribution to recombination from localized states (see for example Refs. [245]) for the following reasons. Our results are in line with previously reported literature results on similar systems (see Supporting Information of Ref. [246]), where this effect was attributed to the activation of the direct transition. Additionally the systems that showed this s-like behaviour, which typically are III-V alloys, had their emission accompanied by a reduction of the FWHM [247], while we do not observe such effect. Finally, the multivalley bandstructure of $Ge_{0.91}Sn_{0.09}$, in which Γ and L valleys are in close proximity (see Chs. 6 and 7), suggests that the direct transition can play an important role. Despite our considerations are not thoroughly conclusive, they point towards a dominant effect from the Γ levels compared to the localized states.

We observe a global increase of the energy position of the cL1-HH1 peak as the spacer thickness is reduced. We attribute this to a space filling effect arising in confined systems, which is a further verification by optical means of the formation of the 2DHG. The distance of the modulation doping layer changes the density of holes that end up in the QW, filling the lowest energy states. Therefore, the photogenerated carriers occupy higher energy levels, inducing a blueshift in the PL.

An additional investigation is carried on by varying the laser power density. The PL spectra are shown in Fig. 54a (for samples S-100 and S-150 see Appendix C). We observe a monotonic increase in the emission intensity as more carriers

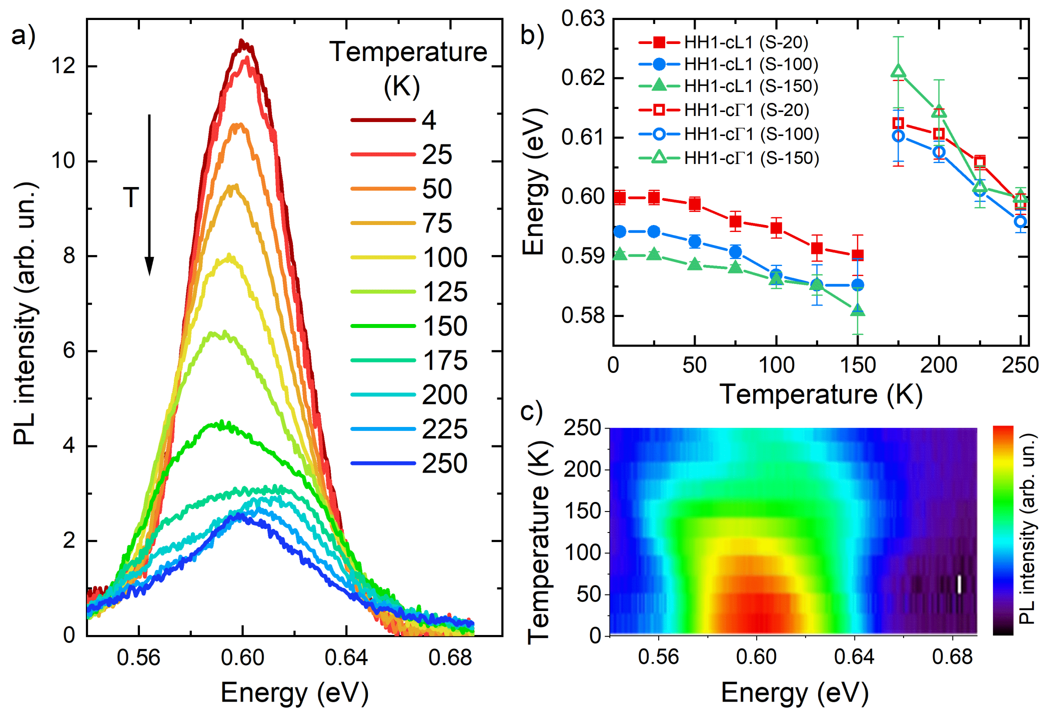

Figure 53: (a) PL spectra in the temperature range from 4 to 250 K of sample S-20. The excitation is fixed at a power density of 3.40 kW/cm^2 with a 50 µm spot diameter and a photon energy of 1.16 eV. At low temperatures the main peak is ascribed to the indirect recombination, while for T > 150 K the emergence of a second feature at higher energy can be observed. Possibly this peak comes from the direct transition. (b) Peak position as a function of the temperature for the three samples. Full mark are the peak positions of the indirect transitions while, open marks are the positions extracted for the higher energy peak. (c) Colour-coded PL intensity map as a function of the emission energy over the investigated temperature range.

are photogenerated. The PL efficiency of a QW can be in general described by the relation [248–250]:

$$\mathcal{I}_{\mathrm{PL}} = \eta I_0^{\alpha} \tag{56}$$

where $\mathcal{I}_{\mathrm{PL}}$ is the integrated intensity and I_0^{α} is the excitation power density of the laser. The exponent α depends on the recombination process and is expected to be close to 1 for exciton recombination and around 2 in the case of pure free-carrier recombination [248–250]. The coefficient η is related to the PL efficiency in the QW and includes several effects as absorption, capture, ionization and recombination of excitons, as well as sample geometry. In Fig. 54b we report the integrated intensity of all samples as a function of the pump power in a double-log scale. It can be seen that the integrated PL intensity increases linearly by rising the excitation power density and thus can be fitted with Eq. 56. The exponent α can be extracted from the fit as the angular coefficient of the line and we obtain $\alpha_1 = 1.22$, $\alpha_2 = 1.39$, and $\alpha_3 = 1.35$. for samples S-20, S-100 and S-150, respectively.

In QW the optical recombination is known to be dominated by exciton contribution at low temperature, thus α is expected to be approximately unitary [248]. In all our samples we find $\alpha > 1$, indicating that free electron-hole pairs can play also a role in the optical recombination process.

Interestingly, a blueshift of the PL peak is observed with increasing the pump density, as shown in Fig. 54c. Since the thermal heating from the laser source would cause an opposite effect, this feature suggests the presence of space filling. This effect is reported in literature to be found in QW with type-II band alignment (see Ch. 7.1) [251–253]. This is due to the fact that in such heterostructures the electrons are localized in the barrier while the holes are located in the well, or viceversa, causing a band bending at both sides of the interface [252]. These two species are accumulated in a narrow region close to the interface where they can recombine. By increasing the optical generation we fill up the lowest states causing the recombination to occur at higher energy and blueshifting the spectra.

For the case of a type-II band alignment, the steady-state density of electrons (n_w) and holes (p_w) generated in a well by an incident photon flux (I) are related

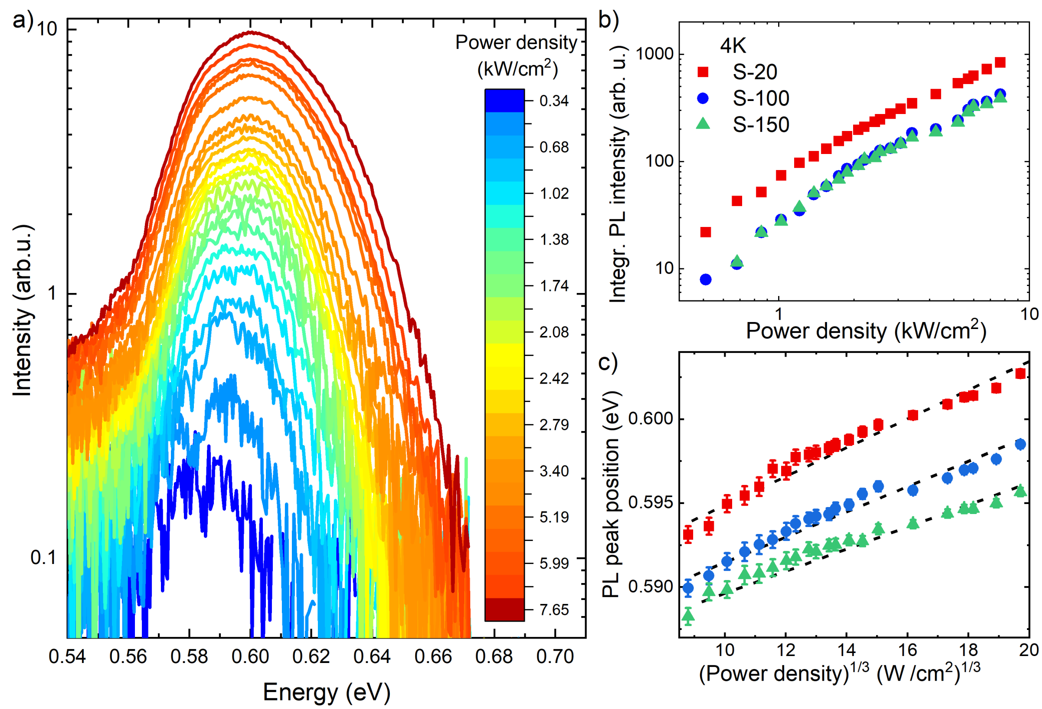

Figure 54: (a) PL spectra of sample S-20 at 4 K under varying excitation power density of a 1.16 eV laser having a spot diameter of 50 µm. (b) Integrated intensity and (c) peak position as a function of the power density for the three samples.

by the equation [251, 254–257]:

$$n_w\,p_w = n_w^2 = \frac{\alpha_A I L^2}{\gamma} \tag{57}$$

where α_A is the absorption coefficient, L is the sum of the well and the barrier thicknesses and γ is the radiative recombination coefficient. If we suppose that holes are confined in the well while electrons find their minimum level in the barrier, we have that in that case a dipole is formed which produces a triangular well and has an electric field::

$$\varepsilon = \frac{2\pi e n_w}{\epsilon_0} \propto \sqrt{I} \tag{58}$$

In this case the ground state is given by:

$$\mathrm{E}_0 = const\,\varepsilon^{2/3} = \left(\frac{9\pi}{8}\frac{2\pi e^2}{\epsilon_0}\right)^{2/3}\left(\frac{\hbar}{2m_e}\frac{\alpha_A L^2}{\gamma}\right)^{1/3} I^{1/3} \tag{59}$$

The electron quantization energy is therefore expected to shift proportionally to the third root of the excitation density. We thus plot the peak position as a function of the third root of the illumination power density in Fig. 54c. A linear response is visible, which strongly supports the above description. This is an interesting result as in literature there are theoretical works that predict both type-I [139, 141, 142] and type-II [143] band alignment for L states but a clear experimental proof can not be found. Here we give an experimental result that provide evidence of a type-II band alignment.

To gather access to the fundamental spin properties of 2DHG in $Ge_{0.91}Sn_{0.09}$ QW for spintronics application, we exploit optical spin orientation by illuminating with a circularly polarized laser (E = 1.16 eV). In the inset of Fig. 55a we plot the σ^+ (black line) and σ^- (red line) spectra for the sample S-20, showing the different PL intensity for the two configurations. When comparing our results with what observed in Si by Jonker et al. in Ref. [258], we notice that the polarization

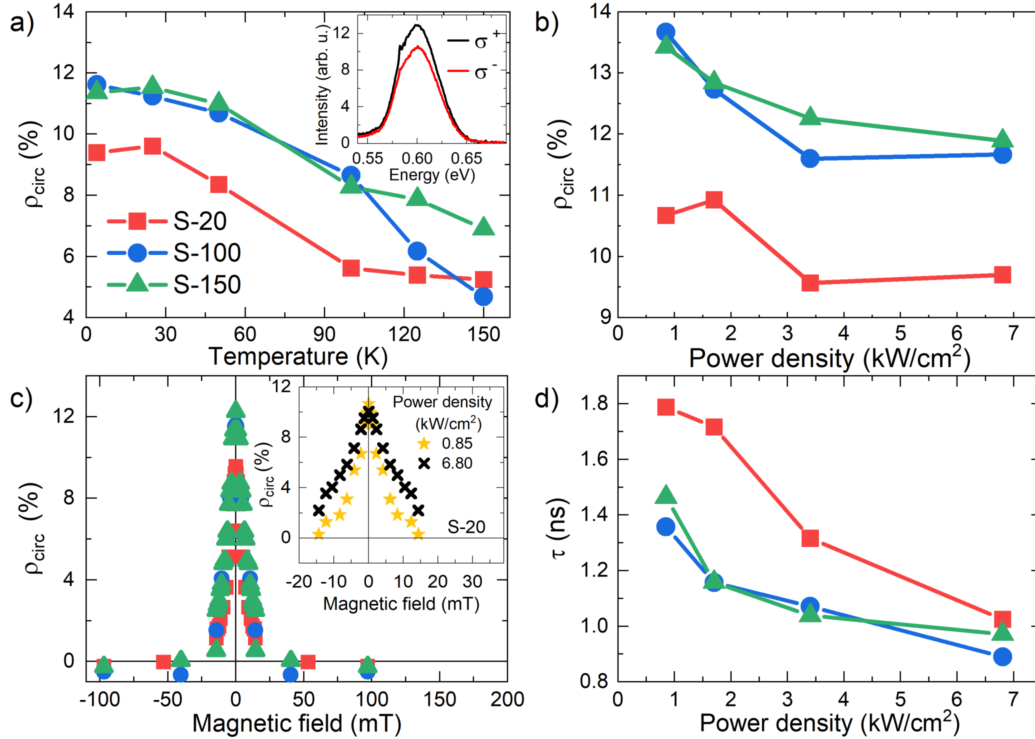

Figure 55: (a) Degree of circular polarization as a function of the temperature measured at the maximum of the emission with a power density of illumination of 3.40 kW/cm^2. The inset shows an example of σ^+ (black line) and σ^- (red line) emission of sample S-20 at 4 K. (b) Degree of circular polarization as a function of power density of the illumination measured at 4 K. (c) Hanle curves for all the three samples under an illumination of 3.40 kW/cm^2. The inset reports the Hanle curves of sample S-20 in a restricted region of the magnetic field under 0.85 and 6.80 kW/cm^2. The uncertainty of the ρ_{circ} data is 0.5 %. (d) Carrier lifetime (τ) at 10 K extracted from Hanle curves. Different illumination conditions are reported. For all the measurements the excitation is performed with a right-handed circularly polarized laser with photon energy of 1.16 eV and a spot diameter of 50 μm.

obtained in our sample by optical means is 3 to 4 times stronger than in Si, despite the absence of a magnetic field to orient the spin [258]. This confirms that our QW system has can be exploited for spintronics application. In Fig. 55a we report the ρ_{circ} measured at the maximum of the spectrum under an illumination power density of 3.40 kW/cm^2 in the temperature range of 0 – 150 K. In the whole temperature range the polarization of sample S-20 is lower than the other two. This is ascribed to the electric field modulation due to the different spacer thickness. By varying the spacer thickness, the distance between the ionized impurities and the well changes with a consequent modulation of the generated electric field. The electric field acts as a perturbation and leads to a loss of polarization when its strength is increased. Additionally, we observe a general depolarization as the temperature rises that can be attributed to phonon-assisted spin-relaxation phenomena, such as Elliott-Yafet mechanism (see Ch. 5). This mechanism becomes dominant in high temperature regime and can completely wash out of the polarization. Due to the disappearance of the PL peak at temperatures higher than 150 K (see Fig. 53a), we are unable to fully map this trend up to room temperature.

In Fig. 55b we report the circular polarization degree as a function of the power density of the excitation extracted at 4 K. Overall S-20 shows a lower ρ_{circ} that is consistent with the effect of the electric field described above. All samples show a reduction of the ρ_{circ} as the power density is increased. The increased overlap of the electron-hole wavefunctions, caused by the increased number of electron-hole pairs optically generated and confined in the active region, leads to a stronger exchange interaction that cause the Bir-Aronov-Pikus mechanism (see Ch. 5).

As seen for the case of $Ge_{1-x}Sn_x$ epilayers (Ch. 10.1) the Hanle effect can be successfully applied to $Ge_{1-x}Sn_x$ systems to investigate the spin lifetime. In the following we extend this magneto-optics technique also to the case of 2DHG system. The Lorentzian shape of the Hanle curves can be seen in Fig. 55c for all three samples under the excitation of 3.40 kW/cm^2.

We notice that a weak magnetic field of approximately 20 mT is sufficient

to completely wash out the polarization. As shown in the inset of Fig. 55c for the two extremal cases, by changing the illumination condition from 0.85 to 6.80 kW/cm^2 we observe an increase in the FWHM, thus suggesting a shortening of the spin lifetime (T_S). Using the same approximations introduced in Ch. 10.1 for the $Ge_{1-x}Sn_x$ epilayers, we can extract τ also for the 2DHG.

The results show that the spin lifetime is monotonically reduced as the power density is increased, which can be ascribed to a stronger contribution from non-radiative Auger recombination. In particular, the greatest effect is found for S-20 where τ is almost halved as it reduces from 1.8 down to 1 ns. These values are higher than for the case of the epilayer samples at the same Sn content (see Ch. 10.1). This is tentatively ascribed to the type-II band alignment as electrons and holes are spatially separated (one confined in the well, the other located in the barrier). This reduces the probability of recombination, lengthening the lifetime.

10.2.4 Inverse spin-Hall effect

The presence of a 2DHG, due to the confinement, concomitantly to the SIA, due to the asymmetric modulation doping, opens up the possibility to study the spin-to-charge interconversion process (see Ch. 2.2).

At first we therefore perform a photovoltage (V_T) measurement by connecting the side channel of the Hall bar in series to a load resistance (R_L) of 10 kΩ while we measure the voltage drop across R_L via a lock-in amplifier; no current is sourced in the sample. The experimental geometry for this measurement is shown in Figs. 56a and b following what suggested in Refs. [35, 62, 259]. For this part the current generator is set to operate in open circuit.

The laser excitation, incident normally to the sample surface (z-axis) with a power density of approximately 8 W/cm^2, is chosen to have right circular polarization and subsequently changed to the opposite helicity. The laser spot is moved across the centre of the sample. The V_T generated is then normalized by the laser power (P_{laser}) to compensate for effects originating from the photogenerated density and the outcome is shown in Fig. 57a. The satellite peak visible in the

V_T/P_{laser} graph can be ascribed to local dis-homogeneity of the sample that were hit by the laser during the scan.

The ratio V_T/P_{laser} shows a separation between the σ^+ and the σ^- curves. This means that a charge imbalance is generated after the optical orientation, suggesting the presence of a spin-dependent phenomena. From what described in Ch. 2.2, we expect to observe a bias signal that changes sign under the excitation with σ^+ and σ^- due to the spin-dependent scattering processes. However, the presence of spurious effects, such as heating-induced Seebeck effect, can introduce additional spin-independent contributions that increase the complexity of the measurements. To rule out these spin-independent effects we measure also the electric signal under excitation of a linearly-polarized light. Indeed, linear polarization can be seen as an equal sum of right- and left-circularly polarized light, thus generating a response located between the signal of σ^+ and σ^-.

Since we are interested in observing the gap between σ^+ and σ^- curves, we use the characterization of Fig. 57a to choose the position of the laser on our Hall bar that gives the biggest separation between the two helicities. Once the laser is set in the selected position, we perform a power dependent analysis with a zero bias applied. We change the exciting light beam to be σ^+, σ^- as well as linear polarization and the V_T generated is reported in Fig. 57b.

The linear polarization (green triangles) is located between the two circular polarization (here shown in blue squares for σ^+ and in red dots for σ^-), demonstrating that the observed effect has a spin-dependent origin. We observe that the V_T increases monotonically with the pump power. For the low pump power, a linear behavior in the log-log scale is observed, which then saturates for the two highest power densities analyzed. We ascribe this flattening of the curve to an increased contribution of thermal effects that reduce the efficiency of the spin-to-charge conversion in the highest illumination regime. This is clearer by considering V_T/P_{laser} shown in the inset of 57b. Here, we obtain an almost constant trend in the low illumination regime, while above approximately 10 W/cm^2 new mechanisms activate that compete with the spin-dependent current.

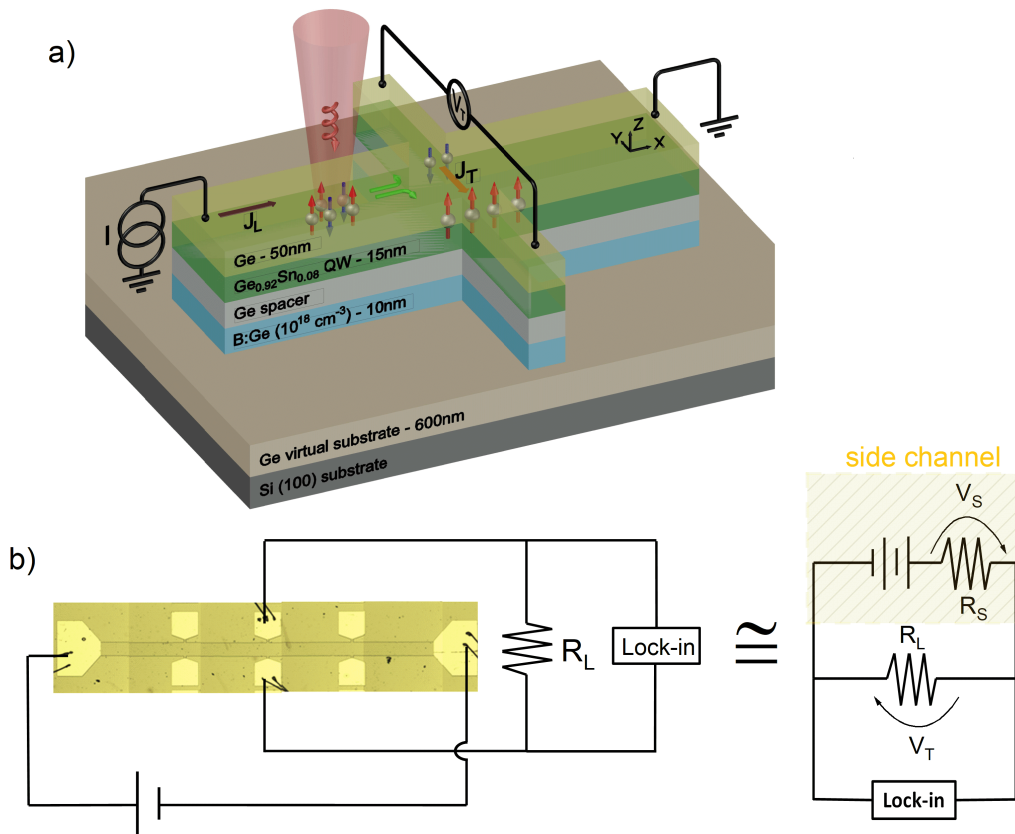

Figure 56: (a) Sketch of the set-up used for the ISHE measurement. The transverse HDP (V_T) is measured across the side channel by a lock-in connected to a load resistance (R_L) of 10 kΩ. (b) Optical image of the device with a representation of the electrical connections [260]. The Hall bar is 4 mm x 200 μm. On the right we report the equivalent circuit for the side channel where we point out that the channel itself possesses a resistance (R_S). The optical generation is accounted for by adding a current generator.

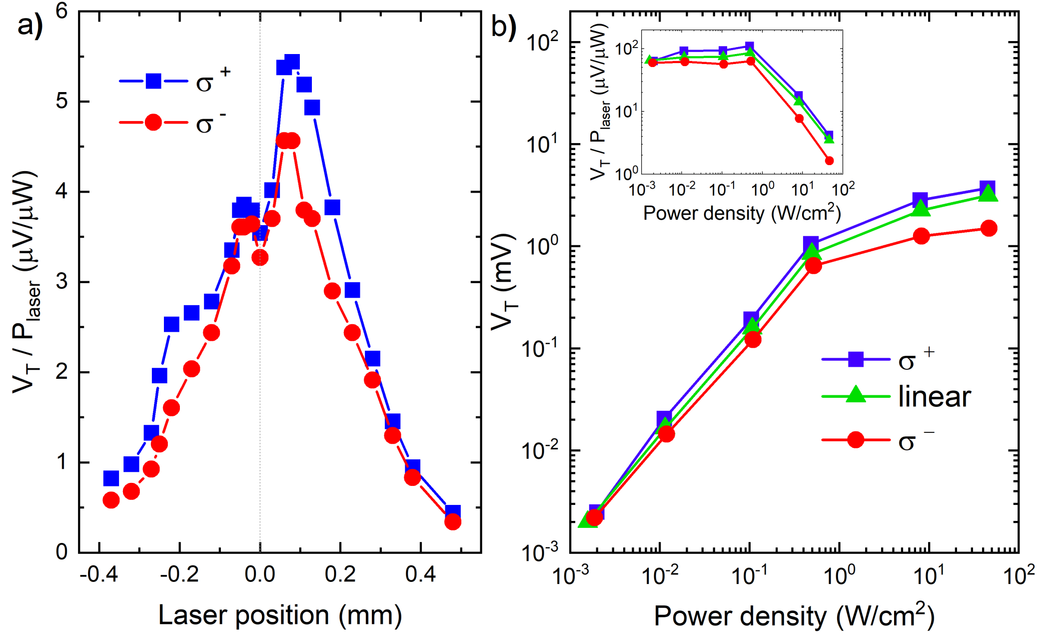

Figure 57: (a) Ratio between the photovoltage and the laser power as a function of the laser spot position for sample S-20. The dashed line represents the centre of the main channel. The excitation helicity is selected to be σ^+ (blue squares) and σ^- (red dots) and the measurement is performed at 4 K under an excitation of ~ 8 W/cm^2 with a 1.16 eV laser possessing a spot diameter of 50 μm. (b) Photovoltage as a function of laser power density for right-handed, linear and left-handed polarization of the pump laser. In the inset we plot the same data as panel (b) after dividing by the illumination power. The error bars are within the size of the symbols.

Nevertheless, the sizeable difference of the photovoltage for the two helicities is an appealing starting point for the investigation of the ISHE. To do this, the circularly polarized laser shine the sample at normal incidence in a fixed position, that is where we maximised the helicity difference. Then we connect the current generator to the main channel (see Fig. 56a, and b) and we source a longitudinal current. To rule out underneath contributions, we measure the helicity-dependent photovoltage (HDP), that is the difference between V_T generated under σ^+ (V_T^+) and σ^- (V_T^-) excitation [259]. From Eq. 12, we have:

$$\mathrm{HDP} = V_T^+ - V_T^- = \Theta_{SH}\,\rho_N\,w\,j_c\,(P^+ - P^-) = 2\,\Theta_{SH}\,\rho_N\,w\,j_c\,P^+ \tag{60}$$

where ρ_N is the resistivity of the sample, w the Hall bar width, P^+ (P^-) is the carrier spin polarization under σ^+ (σ^-) excitation. Here we have to use the carrier spin polarization right after the excitation and not the one extracted after the recombination process (that is ρ_{circ}). Since the compressive strain removes the degeneracy between LH and HH states (see Ch. 7.2), we can use $P^+ = 2\,\rho_{circ} = 0.18$, as can be understood by considering the optical orientation process described in Ch. 3.

From the circuit illustrated in Fig. 56b we extract the HDP generated across the sample (V_S) as:

$$V_S = \frac{R_S}{R_L}\,\mathrm{HDP} \tag{61}$$

where R_S is the resistance measured from the side channel. An I-V characteristic estimates R_S to be approximately 210 kΩ at 4 K. The results of the V_S are reported in Fig. 58a. A clear linear dependence is observed over a wide range of the illumination conditions, even if in the lowest regime (pink triangles) a deviation from linearity is visible due to the smaller signal-to-noise ratio. Interestingly when the laser power density is set to 8 W/cm^2 (dark-red squares) we observe a V_S of approximately 5 mV even in absence of a longitudinal current. We ascribe this to the small but non null contribution of Seebeck effect due to the laser-induced thermal heating.

By performing a linear fit we extract the spin-Hall angle according to Eq. 60.

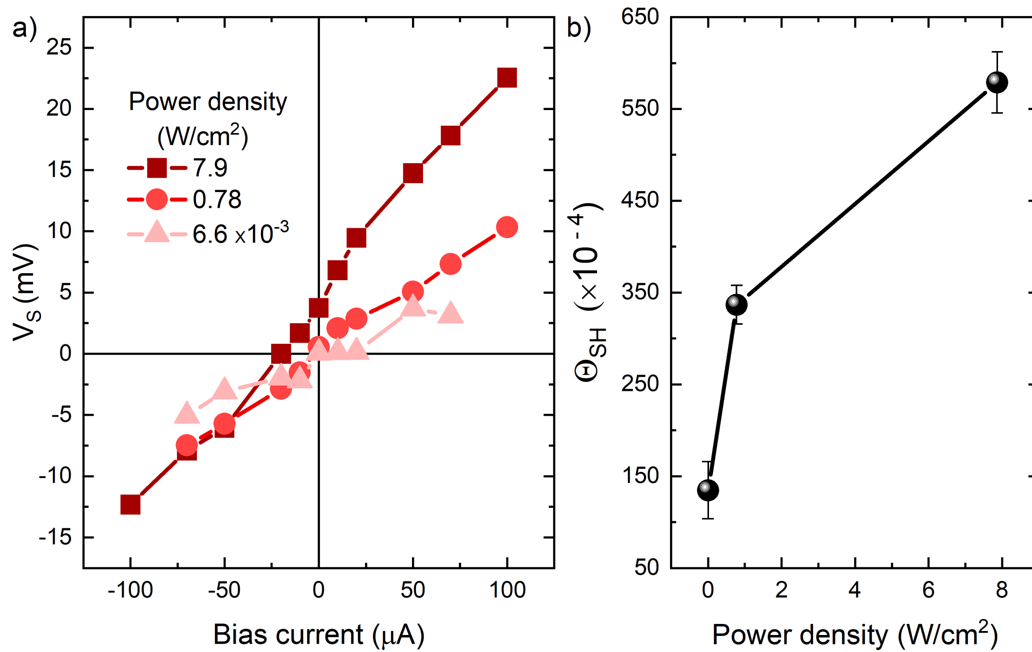

Figure 58: (a) Helicity-dependent photovoltage measured across the sample (V_S) as a function of the sourced current along the longitudinal channel. The relation is almost linear (see Eq. 12), thus confirming the presence of the ISHE. The deviation from lineartiy for the lowest excitation energy is ascribed to the higher noise-to-signal ratio as well as possibly to a weaker spin-to-charge conversion effect. (b) Calculated spin-Hall angle as a function of power densities. The power dependence indicate that a more efficient spin-to-charge conversion is found for higher excitation.

The values are reported in Fig. 58b. Here we see that Θ_{SH} increases monotonically with the power density going from approximately 130×10^{-4} to 580×10^{-4} when the laser is increased by three orders of magnitude from 7×10^{-3} to 8 W/cm^2.

By comparing our results with the reported values of Θ_{SH} for Si and Ge in Table 1, we observe that the extracted value for our $Ge_{0.91}Sn_{0.09}$/Ge QW is 10 to 60 times higher than in Ge, regardless of the used excitation density. This is in line with the expected SOC-induced enhancement of spin properties of Sn with respect to elemental Ge (see Chs. 1 and 2). Additionally, our results are approximately two times bigger than the only available data of Θ_{SH}, reported in Ref. [35] for the case of $Ge_{0.95}Sn_{0.05}$ epilayer. This is possibly ascribed to the increased Sn content as well as to the band spin-splitting induced by the presence of the SIA, which can further enhance spin-dependent phenomena.

11 Conclusions

Microelectronics has reached the end of the Moore's law and is now looking for a paradigm shift to push even further nowadays performances. Spin-optoelectronics is a promising alternative as it merges spintronics, optoelectronics, and nanotechnology to exploit all their advantages to develop devices where the information is encoded into the spin degree of freedom. This possibility is allowed via the SOC, a fundamental quantum mechanical property that couples the spin to the momentum of carriers. In this thesis we have studied SOC in heterostructures of group IV semiconductors, which possess the interesting property of being easily integrated in the Si fabrication processes.

We have performed polarization-resolved photoluminescence measurements on p-i-n diodes with the intrinsic region composed of 50 type-I Ge QWs embedded in $Si_{0.15}Ge_{0.85}$ barriers. A successful optical orientation has been achieved showing a different emission intensity of co- and counter-polarized emission with respect to the excitation for both the direct and the indirect transitions. By applying an external electric field, we have observed the QCSE for different illumination conditions.

We have exploited continuous-wave as well as time-resolved techniques to gather access to the Rashba physics of these low-dimensional systems at different illumination and bias conditions. Polarization-resolved photoluminescence analysis unveils a tunable degree of circular polarization with the illumination power density. This can be ascribed to the electrical screening of the Rashba field thanks to the photogenerated carriers. Indeed, ρ_{circ} increased approximately from 7 to 18 %. Our investigation is further supported by TRPL measurements performed on the indirect emission, from which we find τ_{indirect} = 14 ns. A result that is minimally affected by the illumination and the electric field. A contribution arising from defects is found in the TRPL analysis, increasing the complexity of the kinetics. A suppression of the defect contribution is however found with both illumination and electric field, leading to a reduction of their associated life-

time. A reduced capture cross-section of the defects as well as the activation of non-radiative Auger recombination are the two proposed explanations for this unexpected behaviour. These findings constitute an all-optical study of the Rashba physics in group IV semiconductors, leading the way towards future investigation of electrical-optical manipulation of spins in quantum technologies based on spin-photon interfaces.

In this thesis we have also carried out investigations of $Ge_{1-x}Sn_x$ alloy. In particular, we have introduced an effective approach for the determination of the carrier lifetime in this narrow gap semiconductors by exploiting a steady-state magneto-optic technique, based on the optical Hanle effect. This technique has never been applied to group IV materials, yet it proved to be a reliable and easy technique for the study of spin physics. The investigation is performed in coherently strained $Ge_{1-x}Sn_x$ with a Sn content from 0 to 10 % and we unveil a subnanosecond lifetime. We find out that non-radiative defect-related recombinations are limiting the carrier kinetics in our system. By increasing the thickness of $Ge_{1-x}Sn_x$ layers, we are able to activate the strain relaxation in a well-controlled way and study its consequences on the dynamics. By doing so, we demonstrate the emergence of the parasitic non-radiative recombination associated with the concomitant nucleation of dislocations, thus finding the shortest effective carrier lifetime for the largest dislocation density.

Finally, the SOC of modulation-doped $Ge_{0.91}Sn_{0.09}$ single QW embedded in Ge barriers has been investigated. The coherently grown well induces a compressive strain in the system that ensures an indirect bandgap nature. This novel heterostructure has shown the presence of a 2DHG formed within the well. Interestingly, power-dependent analysis has suggested a type-II band alignment in the L-valley despite being considered to possess a type-I band alignment from most of the theoretical reports. A more profound investigation is thus required for this system to obtain an experimental confirmation and solve this question.

Specifically, three samples have been studied with a different spacer layer. A successful optical orientation has shown a ρ_{circ} in the range of 10 - 14 % for all

samples. The Hanle-effect-based technique has been exploited to gather access to the carrier lifetime. A monotonic reduction of τ with the increasing illumination power density has been observed, which is in the range of 1 - 2 ns. Ultimately we have patterned a Hall bar device on each sample and we studied the inverse spin-Hall effect in this alloy. The spin-Hall angle has been extracted for different power densities of the illumination and has been found that Θ_{SH} increases with the excitation pump becoming 30 times bigger than that of Ge in the investigated range [71, 72]. These findings show that $Ge_{1-x}Sn_x$ heterostructures are a promising system for spin-optoelectronics applications.

In conclusion, this thesis is devoted to an all-optical investigation of SOC in heterostructures of group IV materials. The results obtained here are a step forward in the investigation of spin dynamics of electrons in group IV and pave the way to future exploration of electrical-optical manipulation of spin in quantum technologies based on spin-photon interaction. The spin manipulation as well as the generation of pure spin currents have important implications in the development of spintronics devices such as spin LEDs, spin interconnects, spin-transistors, spin probing devices and spin-based memories [261–263]. For example, in Fig. 59a after the injection of a pure spin current a gate voltage would manipulate the spin and select the on/off state of the node [262]. This, when considered in a more complex architecture (Fig. 59b), opens the possibility to perform spin-based logic operations [261].

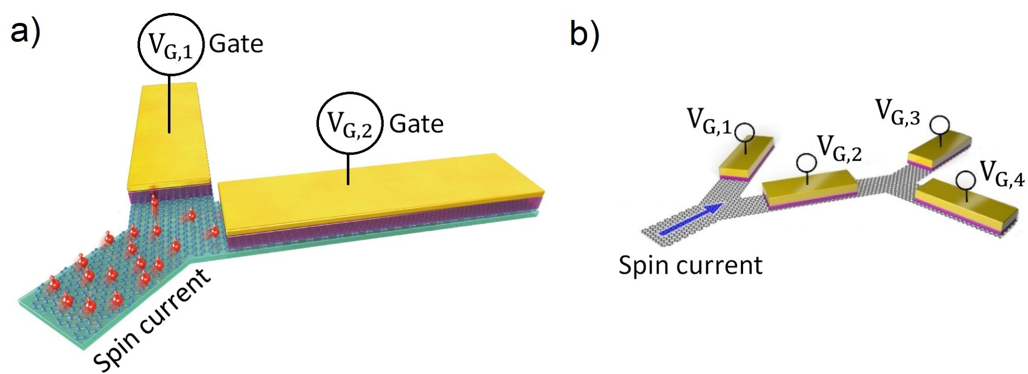

Figure 59: (a) A Y-shaped spin-current demultiplexer with gate voltages V_G for voltage control of pure spin currents. (b) Simple schematic of a more complex platform that enables logic operations [261, 262].

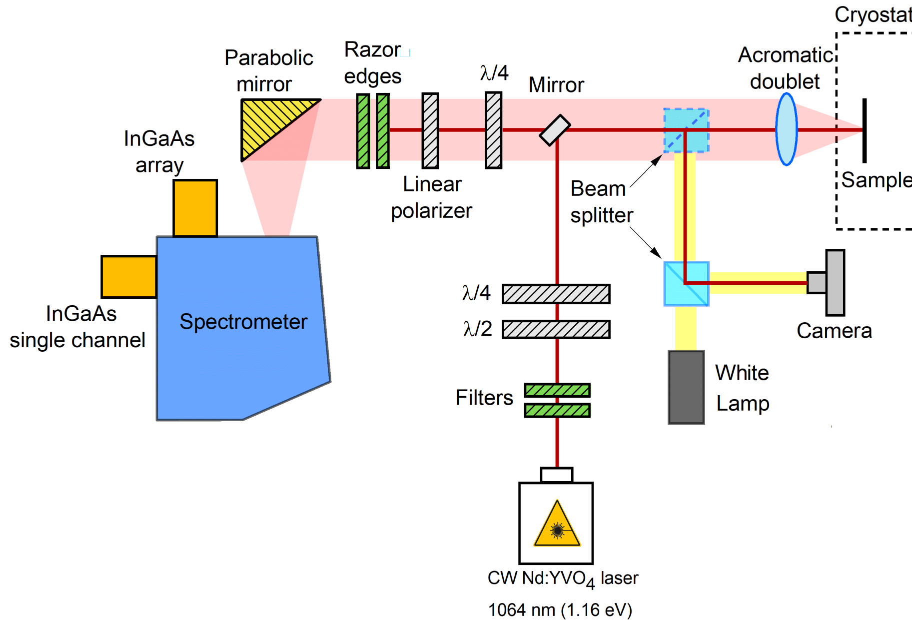

Figure 60: Sketch of the experimental set-up used for the polarization-resolved continuous-wave PL measurements.

Appendix A

This appendix is devoted to the description of the experimental set-up used in this thesis.

A.1 Continuous-wave PL set-up

In Fig. 60 we report a schematic drawing of the experimental set-up used for the polarization-resolved CWPL measurements. The light source is a linearly polarized CW Nd:YVO_4 laser emitting at 1064 nm (1.16 eV). The nominal power can be adjusted from few mW to 500 mW, whereas the effective power is measured by a power meter in proximity of the achromatic doublet. The exciting beam is filtered through two 1064 nm band-pass filters and a 850 nm long-pass filter. It passes through a half waveplate ($\lambda/2$) and a quarter waveplate ($\lambda/4$). This optical path allows us to control the circular polarization of the beam.

The laser is then directed on the sample by a 3 mm diameter silver mirror, mounted on a 5 cm diameter gimball support. This allows the measurements to be performed in backscattering configuration, that is, the direction of the luminescence detection is the same of the excitation and in our case it is also perpendicular to the sample surface. The laser light is focused on the sample surface by means of a 1-inch-diameter achromatic doublet with 100 mm focal length.

To observe the position of the beam onto the sample a flipping mirror is mounted on the optical path and is coupled to a lamp source and a camera.

The sample is mounted in a cryostat cooled by a closed cycle helium refrigerator (Oxford Optistat AC-V12) that can reach a base temperature of 4 K. The mounting process is performed by first gluing the sample on a copper plate via silver paste and then onto the cold finger of the cryostat via a heat sink paste; this ensures the sample a better heat dissipation. Vacuum is obtained by means of a set of pumps (HiCube Classic, produced by Pfeiffer Vacuum): a rotatory pump for the low vacuum regime combined with a turbomolecular pump to reach the base pressure of about 10^{-6} mbar.

The PL signal is collected by the doublet and sent to the analyzer, consisting of a rotating $\lambda/4$ waveplate followed by a linear polarizer. The waveplate is controlled by a software and can be coupled to the detection system to measure the intensity at different angles. Two 1064 nm razor edge filters reject the laser light that is reflected from the optics and the surface of the sample. The PL signal is coupled into a spectrograph. The monochromator is an HORIBA iHR320 equipped with 3 diffraction gratings. In this work, only the 150 lines/mm groove density with blaze at 2000 nm is used, whose spectral efficiency is shown in Fig. 61.

The dispersed light can be directed towards two different detectors that can be selected by means of a movable mirror. The choice is between:

- A liquid nitrogen cooled InGaAs multi channel detector (model Horiba Symphony II with 512 pixels) with a cut-off energy at approximately 0.77 eV. The quantum efficiency is shown in Fig. 62a.

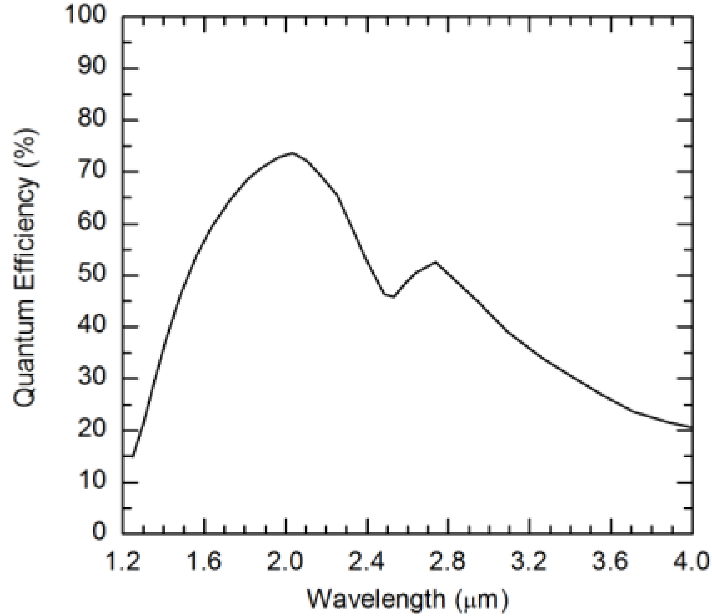

Figure 61: Quantum efficiency of the 150 lines/mm holographic diffraction grating. Blaze is at 2 μm.

- A liquid nitrogen cooled InGaAs single channel detector (DSSIGA 2.2 LN sold by Horiba Jobin Yvon) with a cut-off energy at approximately 0.52 eV. The quantum efficiency is shown in Fig. 62b. The output signal of the detector is filtered by means of a SR510 Stanford lock-in amplifier.

A.2 Time-resolved PL set-up

To perform time-resolved measurements we used the set-up depicted in Fig. 63. The excitation source is a 1.165 eV (1064 nm) DTL-324QT Nd:YAG Q-switch pulsed laser (Laser-Export) set to a repetition rate of 10 kHz with an average power density of 6.8 kW/cm^2. For the selected frequency the pulse width is approximately 11 ns as shown in Fig. 64. The optical path is the same as for CWPL so the reader can refer to Ch. A.1 for the complete explanation.

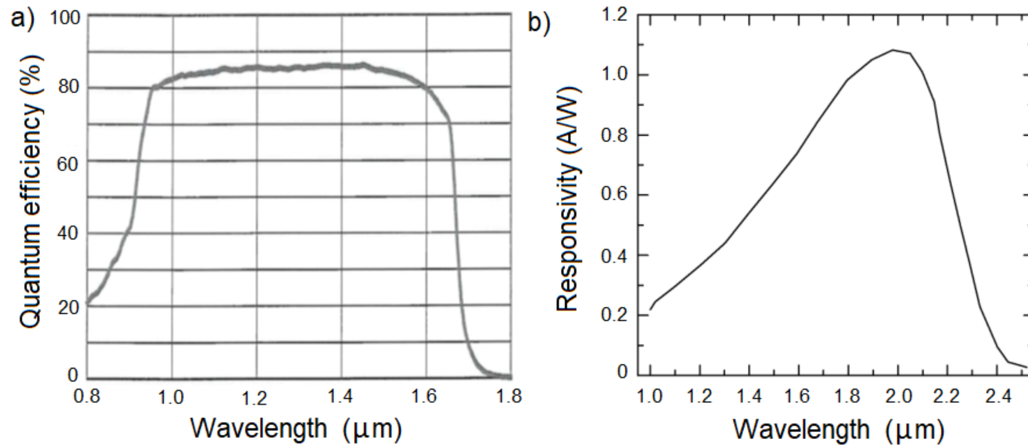

Figure 62: (a) Quantum efficiency of the InGaAs multi channel detector [264]. (b) Responsivity of the InGaAs single channel DSSIGA2.2 LN as a function of the wavelength.

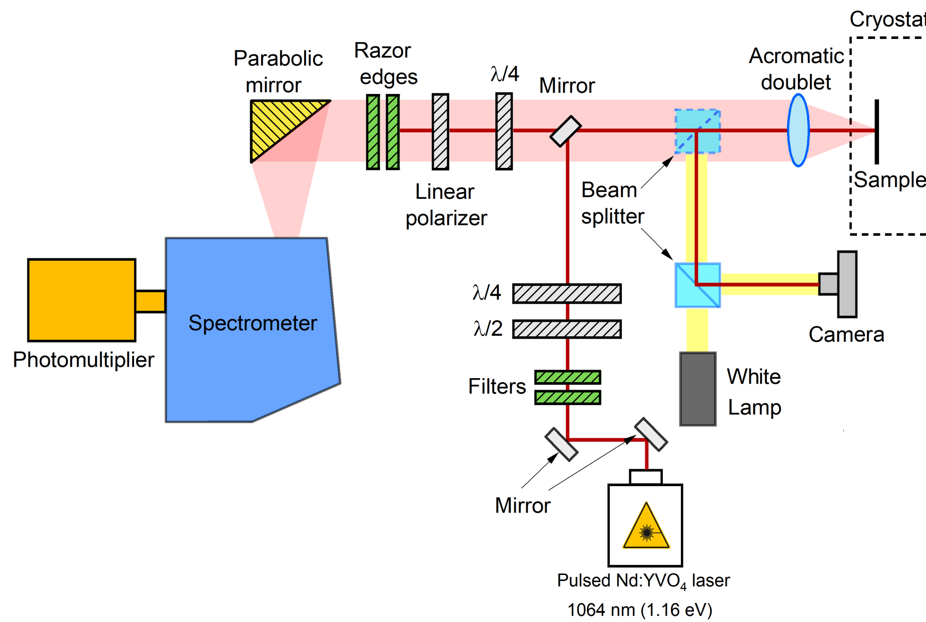

Figure 63: Sketch of the experimental set-up used for polarization resolved time-resolved PL measurements.

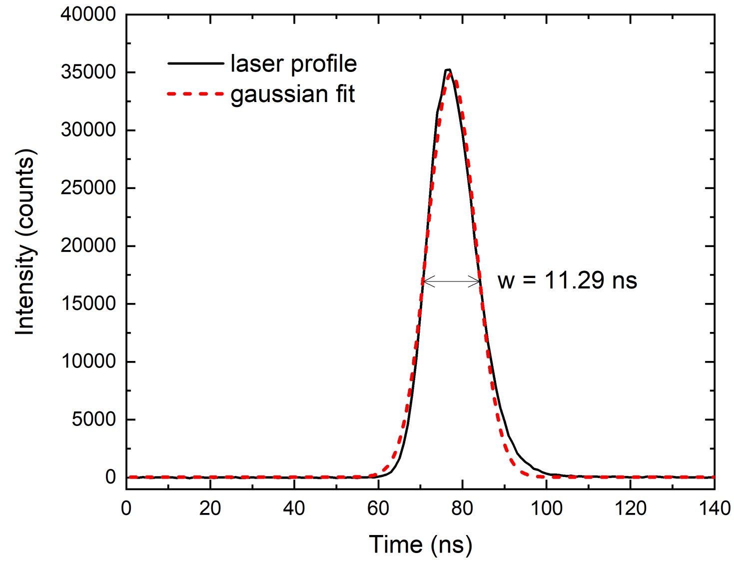

Figure 64: Laser pulse profile (black line) and Gaussian fit (red dashed line). The FWHM obtained from the fit is 11 ns.

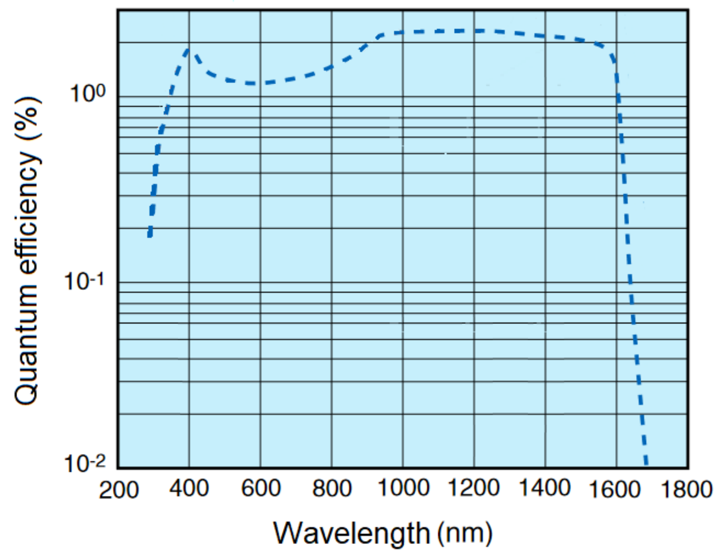

Figure 65: Quantum efficiency of the photocatode as given by the producer [265].

To detect the signal, the light is sent to a liquid nitrogen cooled Hamamatsu R5509-73 PMT, with a cut-off energy at about 0.77 eV and a quantum efficiency shown in Fig. 65. The signal is recorded by a FAST ComTec P7888-1(E) multi-stop acquisition board, working in single photon counting mode. The maximum time resolution offered by the instrument is 1 ns. The signal is displayed by means of an oscilloscope, and a trigger coming from the laser provides the start of the acquisition.

A.3 Photocurrent measurements

During the discussion of the p-i-n diode samples, we showed the spectral responsivity of a device (see Fig. 35a). Such measurement requires a small variation of the CWPL set-up where the excitation is switched to a SuperK EVO laser produced by NKT Photonics: a supercontinuum fiber laser able to emit a coherent radiation with spectral coverage from 900 to 2000 nm with an integrated output power greater than 3 W and a pulse repetition rate of 20 MHz. The SuperK EVO is then connected to a tunable wavelength filter, the SuperK Select, which allows to select the emission wavelength from the broad emission spectrum.

The laser is introduced along the optical path and shone on the sample after being filtered. The photocurrent is recorded by modulating the excitation and exploiting a lock-in while the power output for each wavelength is measured with a power meter.

A.4 Magnetic field characterization

To perform magneto-optic measurements such as Hanle effect (Ch. 4), we apply a magnetic field perpendicularly to the surface sample and therefore to the optical path as well. The magnetic field is generated via two sets of permanent cylindrical magnets that are placed within a supporting system that runs on a graduated rail (see Fig. 66a). This allows for a precise characterization of the magnetic field intensity. In Fig. 66b (66c) it is reported the magnetic field intensity as a function

of the distance between the Nd-based (Ferrite-based) magnets, whose diameter is 2 (6) cm. The uniformity of the magnetic field is ensured by the fact that the laser spot on the sample is much smaller than the magnets size (50 μm of the laser spot compared to few cm of the magnets).

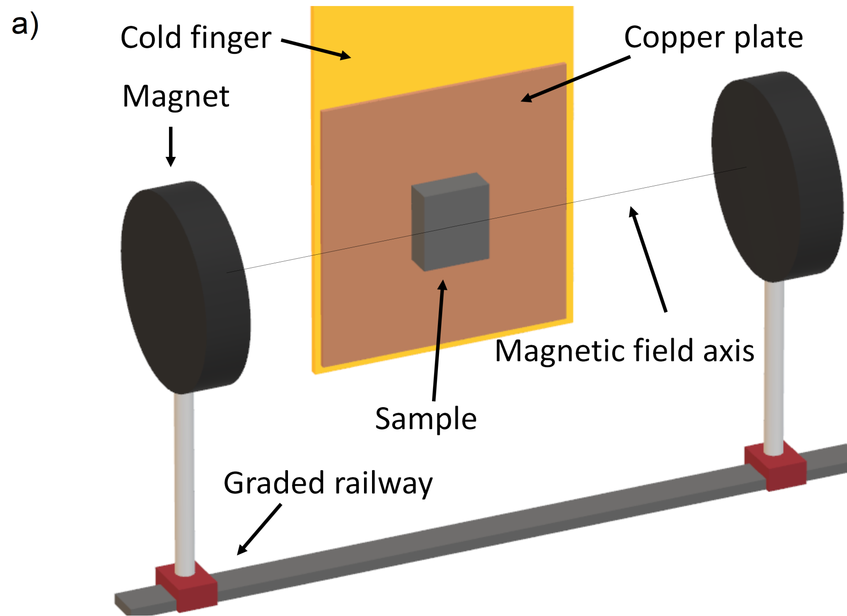

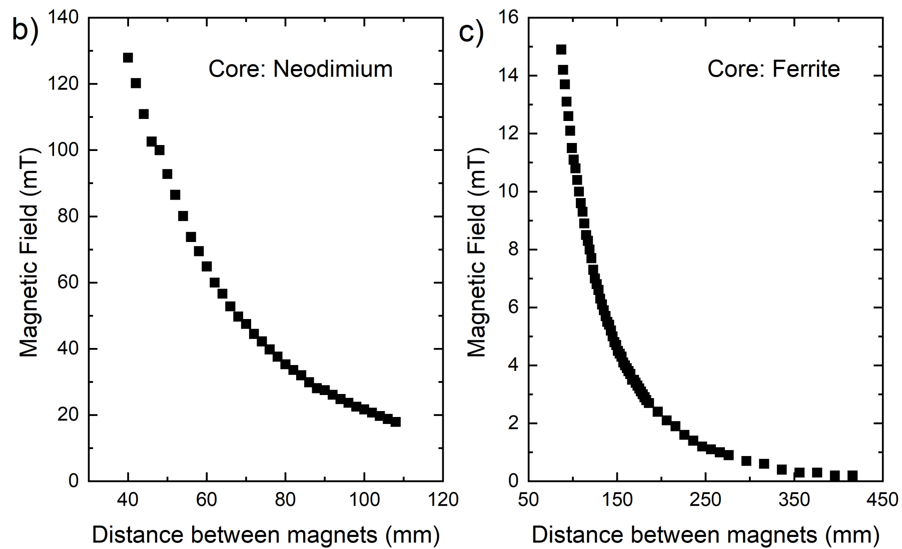

Figure 66: (a) Schematic of the application of the magnetic field in our set-up. (b) Magnetic field intensity as a function of the distance between the permanent magnets made of Neodymium and (c) Ferrite. The error bars are within the size of the symbols.

Appendix B

This appendix is devoted to the description of the technique exploited throughout this thesis for the study of the PL polarization, namely Stokes analysis.

B.1 Stokes analysis

If we consider a polarized light beam propagating along the z axis, the electric field can be described by two oscillating signals with period T:

$$E_x(\mathbf{r}, t) = E_{0x}\, cos(\omega t + k \cdot z + \delta_x) \tag{62}$$

$$E_y(\mathbf{r}, t) = E_{0y}\, cos(\omega t + k \cdot z + \delta_y) \tag{63}$$

where E_{0x} and E_{0y} are the maximum amplitudes, $\omega = \frac{2\pi}{T}$, $k = \frac{2\pi}{\lambda}$ and δ_x and δ_y are the arbitrary phase of the two components.

From Eqs. 62 and 63 we can describe the optical wave by means of an ellipse [266]:

$$\frac{E_x(z,t)^2}{E_{0x}^2} + \frac{E_y(z,t)^2}{E_{0y}^2} - 2\frac{E_x(z,t)E_y(z,t)}{E_{0x}E_{0y}} cos\delta = sin^2\delta \tag{64}$$

where we have defined $\delta = \delta_y - \delta_x$. Among all possible polarized states there are few that possess particular combinations of amplitude and phase that can be considered as degenerate states. Here we list them:

- linearly horizontal (vertical) polarized light: if $E_{0y} = 0$ ($E_{0x} = 0$),
- linear $+45°$ ($-45°$) polarized light: if $E_{0x} = E_{0y}$ and $\delta = 0$ ($\delta = \pi$),
- right (left) circularly polarized light: if $E_{0x} = E_{0y}$ and $\delta = \frac{\pi}{2}$ (δ = -$\frac{\pi}{2}$)

these states can be obtained in laboratories by using linear polarizers, half-waveplates and quarter-waveplates and find vast applications in experimental measurements. For example, we have already seen in Ch. 3 that circularly polarized light is fundamental for achieving optical spin orientation in semiconductors.

A complete description of the polarization can be obtained by measurable quantities known as Stokes parameters [267, 268]. These read as:

$$S_0 = E_{0x}^2 + E_{0y}^2 \tag{65}$$

$$S_1 = E_{0x}^2 - E_{0y}^2 \tag{66}$$

$$S_2 = 2E_{0x}E_{0y}\cos\delta \tag{67}$$

$$S_3 = 2E_{0x}E_{0y}\sin\delta \tag{68}$$

and satisfy the following relation:

$$S_0^2 = S_1^2 + S_2^2 + S_3^2 \tag{69}$$

The first parameter S_0 describes the total intensity of the beam; the second parameter S_1 describes the preponderance of horizontal over vertical polarization light; the third parameter S_2 describes the preponderance of linear +45° over −45° polarized light and the last S_3 describes the preponderance of right over left circularly polarized light.

The degree of polarization can be defined as:

$$\rho_{tot} = \frac{I_{pol}}{I_{tot}} = \frac{\sqrt{S_1^2 + S_2^2 + S_3^2}}{S_0} \tag{70}$$

where I_{pol} represents the sum of all possible contribution that yield a polarized light while I_{tot} is the total intensity.

Partially polarized light can be considered as a superposition of unpolarized and completely polarized light. In this case Eq. 69 becomes:

$$S_0^2 > S_1^2 + S_2^2 + S_3^2 \tag{71}$$

So far we have excluded unpolarized beam, i.e., when the electric field ran-

domly oscillates over time. In this case the above polarization description can not be used.

In this thesis the Stokes analysis is exploited by performing a complete characterization of the PL polarization. The measurement of the Stokes parameter is made by using a rotating quarter-waveplate followed by a fixed linear polarizer. In this configuration the PL intensity is given by [266]:

$$I(\theta) = \frac{1}{2}(A + B\, sin\, 2\theta + C\, cos\, 4\theta + D\, sin\, 4\theta) \tag{72}$$

where θ is the angle of the waveplate with respect to the polarizer and:

$$A = S_0 + \frac{S_1}{2}, \quad B = S_3, \quad C = \frac{S_1}{2}, \quad D = \frac{S_2}{2} \tag{73}$$

By fitting the data taken over 360° with Eq. 72 by using a least squares procedure, it is possible to extract the Sokes paramenter and obtain information on the polarization of the light. In particular, in our analysis we are interested in the degree of circular polarization that, similarly to Eq. 70, is defined as:

$$\rho_{\text{circ}} = \frac{S_3}{S_0} \tag{74}$$

In our measurement a positive (negative) value of ρ_{circ} means a co-polarized (counter-polarized) emission with respect of the excitation.

Appendix C

This appendix presents additional experimental results that are not presented in Chs. 9 or 10.

C.1 Additional experimental results: p-i-n diodes

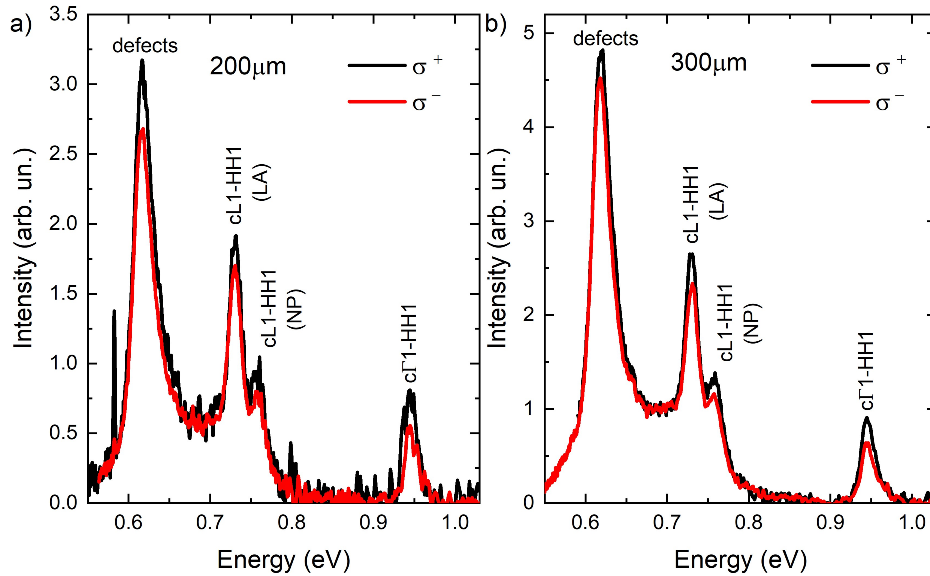

Figure 67: PL spectra of p-i-n diode with mesa diameter of (a) 200 μm and (b) 300 μm. The excitation is performed by a 1.165 eV laser with a power density of 3.40 kW/cm^2 and a spot diameter of 50 μm. Black (red) line represents co-polarized (counter-polarized) emission with respect to excitation.

In Figs. 67a and b we present the PL spectra of the other devices analyzed. In particular we studied p-i-n diodes with a mesa diameter of 200 μm (panel a) and 300 μm (panel b). Co- and counter-polarized emission with respect to σ^+ excitation are shown, demonstrating the successful optical spin orientation in these devices. For both devices we found that cΓ1-HH1 is at 0.945 eV, cL1-HH1 (NP)

is at 0.759 eV and cL1-HH1 (LA) is at 0.731 eV.

In Fig. 68a the temperature dependence of the cΓ1-HH1 transition for device with the diameter of 500µm is shown. The temperature dependence of the bandgap can be described by the Varshni's relation [269]:

$$E_g(T) = E_g(0\,K) - \frac{\alpha T^2}{T + \beta} \tag{75}$$

where α and β are constants extracted form the fit. For our devices we found $\alpha = 6.8 \cdot 10^{-4}$ eV/K and $\beta = 408$ K, in agreement with previous literature results [270]. The peak position, the fitting curve and the extracted parameters are shown in Fig. 68b. The purple square, origination from the measurement at 200 K, shows a significant deviation from the fit. This is ascribed to the weak PL signal that makes more complicated the correct positioning of the peak.

In Fig. 68c we report the peak shift caused by the QCSE in the temperature range from 4 to 125 K for the device with a diameter of 300 µm.

In Figs. 69a and b we show the PL spectra of the cΓ1-HH1 transition under the application of an external bias for devices with 200 µm and 300 µm diameter, respectively. We observe the QCSE in both devices. In Figs. 69c and d we show corresponding energy shift as a function of the electric field.

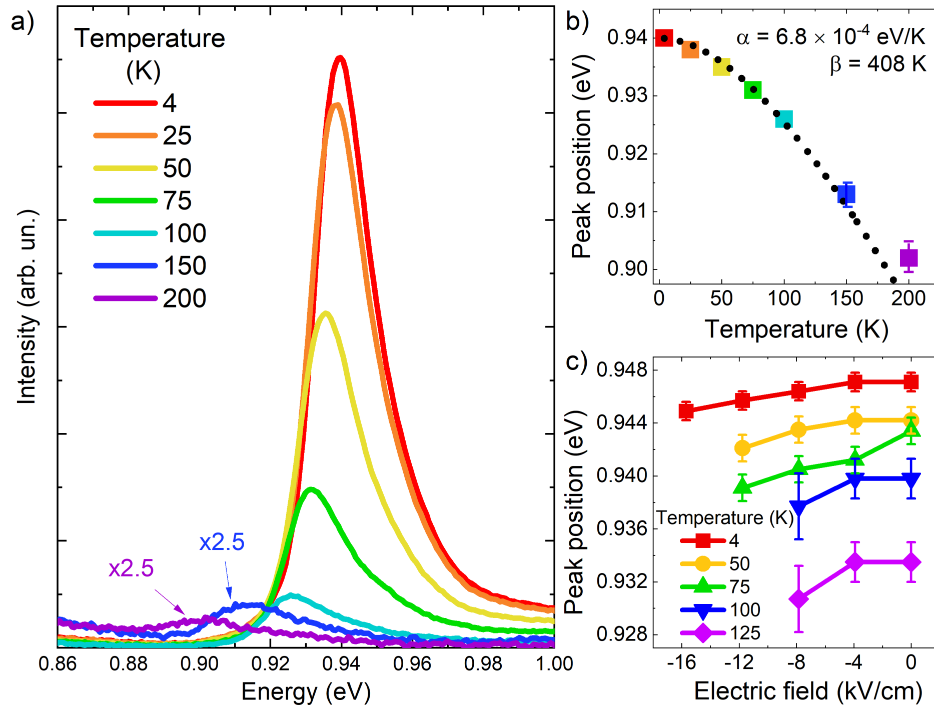

Figure 68: (a) Temperature dependence of the cΓ1-HH1 transition. The curves for 150 and 200 K have been magnified by 2.5 times for an improved visibility. (b) Peak position in the whole temperature range is reported and the Varshni fit is shown as a dotted black line. (c) QCSE in the temperature range from 4 to 125 K for the device with a diameter of 300 μm. The excitation is performed by a 1.165 eV laser with a power density of 3.40 kW/cm^2 and a spot diameter of 50 μm.

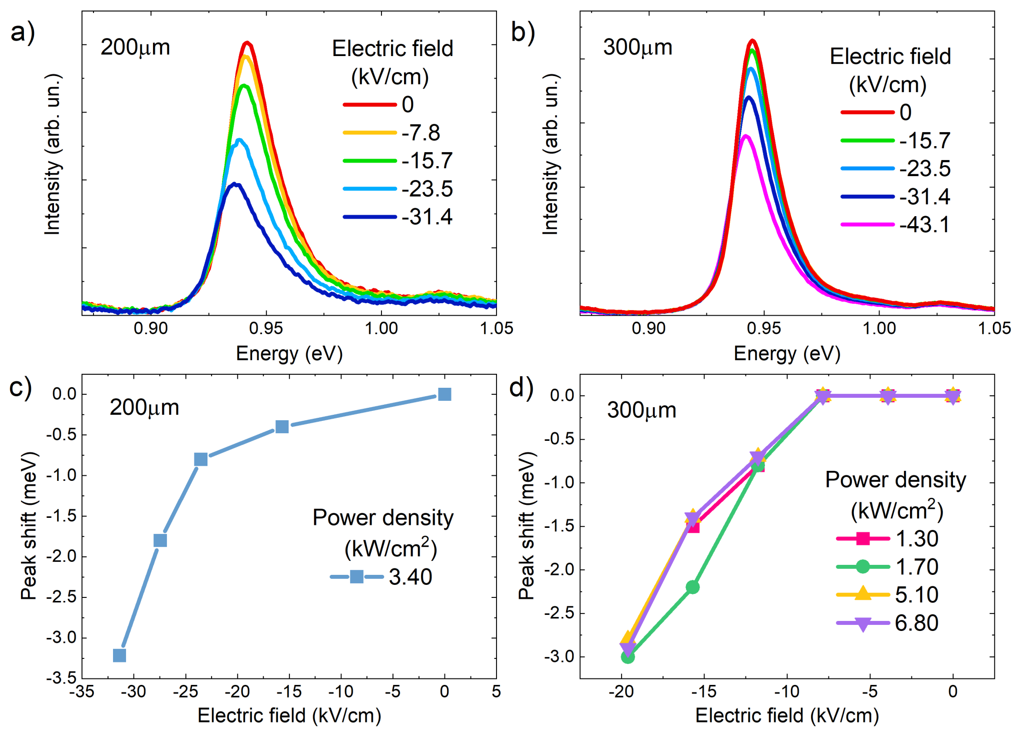

Figure 69: QCSE effect for p-i-n diodes with mesa diameter of (a) 200 μm and (b) 300 μm. The excitation is performed by a 1.165 eV laser with a power density of 3.40 kW/cm^2 and a spot diameter of 50 μm. Extracted peak shift for (c) 200 μm and (d) 300 μm devices under different illumination conditions.

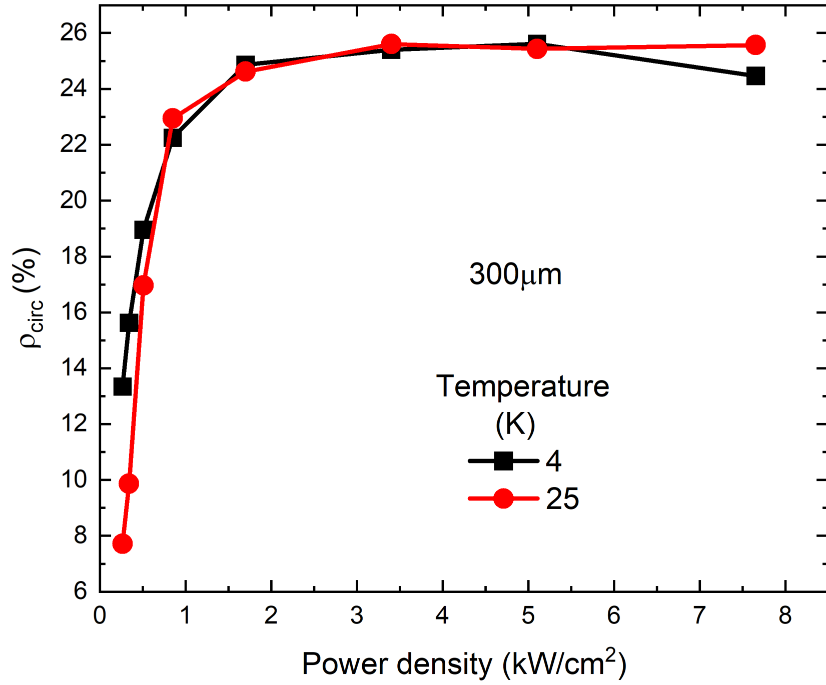

Figure 70: Degree of circular polarization (ρ_{circ}) as a function of illumination power density at 4 K (black line) and 25 K (red line) for the device with the diameter of 300 μm. No external bias has been applied to the device.

In Fig. 70 we show ρ_{circ} for the device with the 300-μm-wide active region. Two temperatures have been studied at no applied bias. We find that the behavior is similar for both 4 K and 25 K. The increment of the pump power results in a first upsurge of ρ_{circ}, which almost doubles its value from ~14 % at 0.25 kW/cm^2 up to ~ 25 % at 3.40 kW/cm^2. This is then followed by a weak loss of polarization for power densities higher than 3.40 kW/cm^2. This last effect is ascribed to the activation of spin-relaxation mechanism due to electron-hole exchange interaction [25], namely Bir-Aronov-Pikus mechanism, as well as a laser-induced thermal heating of the sample.

When comparing these results with the data shown in Fig. 37a we observe the same trend of the ρ_{circ} but the maximum value found in the 300 μm device is higher than the one shown previously (25 % compared to 18 %). This is ascribed

to the presence of defects in the device with a diameter of 500 μm that affect negatively the polarization. We expect the maximum value of ρ_{circ} to approach that of structurally symmetric p-i-n diodes. This is due to the fact that by screening the built-in potential with optical generation (as described in Ch. 9) we suppress the Rashba field and consequently any spin relaxation deriving from it. This situation is equivalent to a device where the Rashba field is not present, that is a structurally symmetric device. In 5-nm-thick Ge QW embedded in 10-nm-thick $Si_{0.15}Ge_{0.85}$ barriers with a symmetric structure, it was found a polarization of the direct emission of ~35 % [208]. The upsurge observed with the laser illumination brings the polarization closer to the reported value in Ref. [208] even if a perfect match is not found. A deeper investigation may bring light to this discrepancy.

In Figs. 71a and b we report the decay curves of co- and counter-polarized emission with respect of excitation for devices with 200 μm and 300 μm, respectively. In the inset we report the carrier lifetimes. For both devices we observe that for the highest power density the long decay is suppressed while the first part after the excitation is unaffected. This finds a confirmation in the carrier lifetime as the τ_{indirect} is found to be approximately 13 ns indipendently from the power density and the device size. τ_{defects} on the contrary is approximately halved when we go from the lowest to the highest illumination regime. In particular, for the device with the mesa diameter of 200 μm (300 μm) we find that τ_{defects} goes from ~100 ns (150 ns) down to ~50 ns (75 ns).

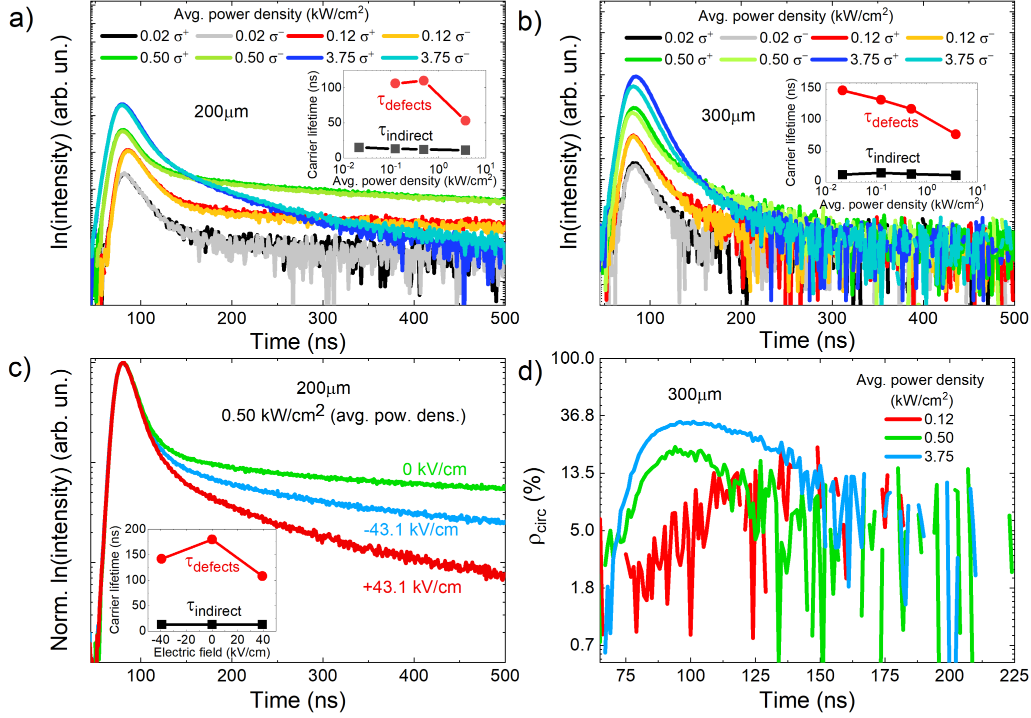

Figure 71: (a) Co- and counter-polarized decay curves measured at 0.758 eV (1636 nm) at null external bias for the p-i-n diode with the diameter of 200 µm. Different power densities of the excitation are reported. In the inset: carrier lifetimes of indirect and defects transitions obtained from double exponential fits performed on the average of co- and counter-polarization curves. (b) Same as in (a) for the device with 300 µm in diameter. (c) Co-polarized decay curve for a different field applied under an illumination of 0.50 kW/cm^2. (d) Decay curves of ρ_{circ} extracted for each power density.

C.2 Additional experimental results: $Ge_{1-x}Sn_x$ epilayer

In Fig. 72 we present the results from the Stokes analysis of the $Ge_{0.94}Sn_{0.06}$ epilayer sample. In the lower panel a color coded map of the PL intensity profile described by Eq. 72 for different magnetic field from 0 to 110 mT. In the upper panel we show the comparison between the Stokes curve at no field (blue curve) and the one at 90.4 mT (red curve). The variation in the curve induces a different value of ρ_{circ}. Here ρ_{circ} changes from 10 % at 0 mT to roughly 0 % at 90.4 mT.

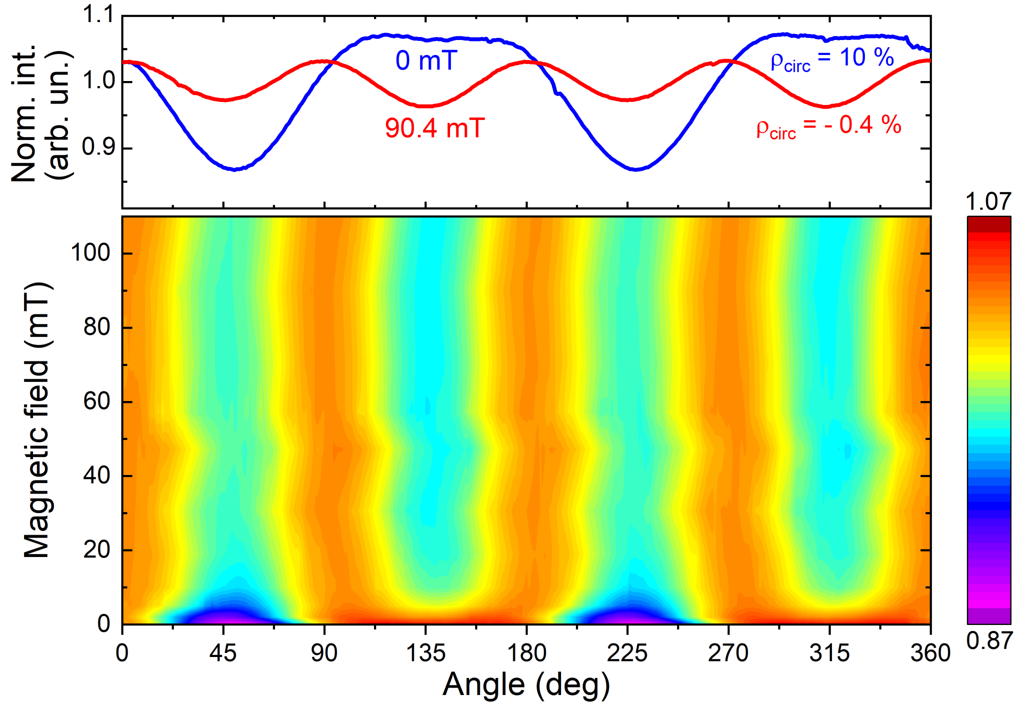

Figure 72: Color coded map of a Hanle curve measurement of sample S-20. In the upper panel an example of Stokes analysis where we show the intensity profile of the PL over a full turn of the analyzing quarter waveplate (see Appendix B for details of Stokes analysis).

C.3 Additional experimental results: $Ge_{1-x}Sn_x$ QW

In Figs. 73a and b we present the results from the electrical characterization of sample S-100 and S-150, respectively. The photocurrent is taken by shining the laser along the main channel (see Fig. 51 for reference positions on the channel). In each inset we show the I-V curve at dark condition and the extracted resistance. The asymmetry between positive and negative bias of the I-V in Fig. 73b is likely to be done to a non-perfectly symmetric electrical contacts.

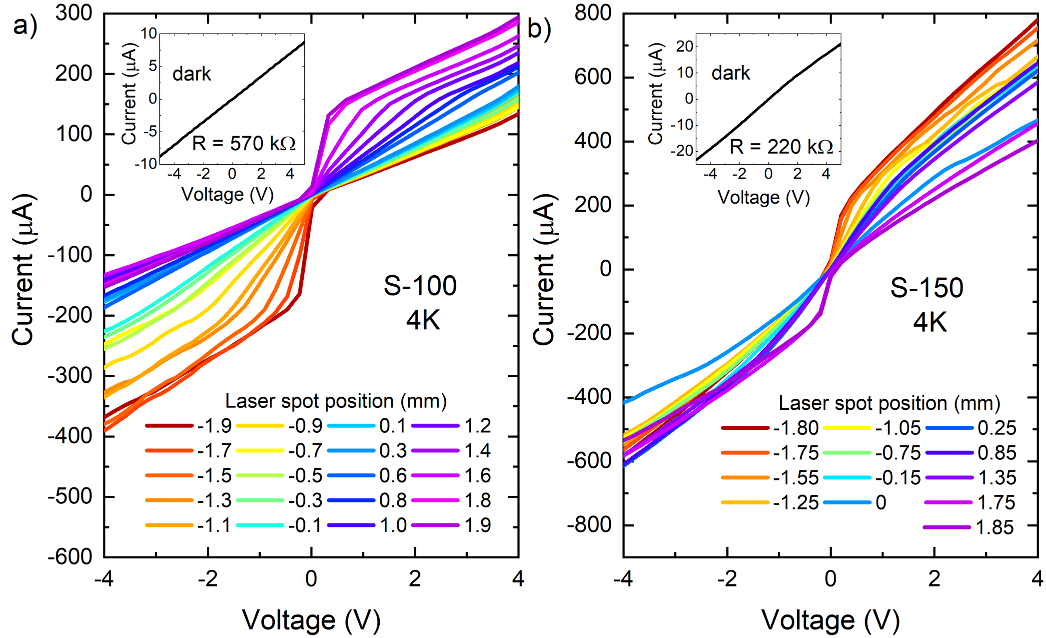

Figure 73: I-V characteristics under illumination at 3.4 kW/cm^2 for sample (a) S-100 and (b) S-150. The laser spot is moved along the channel from one contact to the other. Laser spot is 50 µm in diameter and the excitation energy is 1.16 eV. The insets show the I-V at dark of each sample and the extracted resistance R.

In Figs. 74a and b we show the PL spectra of sample S-100 and S-150, respectively, in a temperature range that goes from 4 to 225 K under an illumination power density of 3.40 kW/cm^2. The presence of a second peak at higher energy, located approximately at 0.62 eV, is found also for these samples for temperature above 150 K .

In Figs. 74c and d we report the PL spectra of sample S-100 and S-150, respectively, for different illumination conditions.

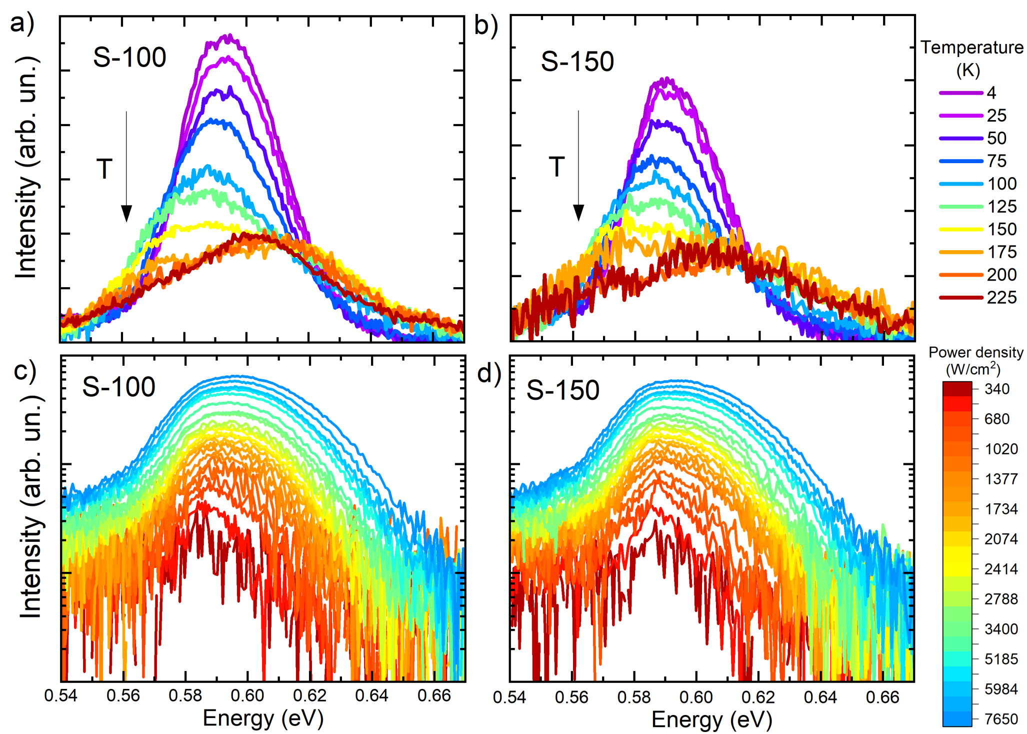

Figure 74: PL spectra in the range from 4 to 225 K of sample (a) S-100 and (b) S-150. The excitation light is fixed at a power density of 3.40 kW/cm^2 with a 50 μm spot diameter and a photon energy of 1.16 eV. PL spectra of sample (c) S-100 and (d) S-150 at 4 K under a varying power density of illumination.

Appendix D

In this appendix we report the *nextnano* code used in Ch. 9.3 for the simulation of the p-i-n diode.

D.1 Nextnano simulation code

```
global{
        temperature = 4 simulate1D{ }
        crystal_zb{ x_hkl = [ 1, 0, 0 ] y_hkl = [ 0, 1, 0 ] }
        substrate{ name = ”Si(1-x)Ge(x)” alloy_x = 0.9 }
}

grid{
        xgrid{
                line{ pos = -351 spacing = 1 }
                line{ pos = -350 spacing = 1 }
                line{ pos = -251 spacing = 1 }
                line{ pos = -250.1 spacing = 1 }
                line{ pos = -250 spacing = 0.1 }
                line{ pos = 2223 spacing = 0.1 }
                line{ pos = 2223.1 spacing = 1 }
                line{ pos = 2224 spacing = 1 }
                line{ pos = 2423 spacing = 1 }
                line{ pos = 2424 spacing = 1 }
        }
}

structure{
            output_region_index{ boxes = ”no” }
            output_material_index{ boxes = ”no” }
```

```
output_alloy_composition{ boxes = "no" }
region{
        everywhere{ }
        ternary_constant{ name = "Si(1-x)Ge(x)" alloy_x = 0.9 }
}
region{
        line{ x = [ -351, -350 ] }
        ternary_constant{ name = "Si(1-x)Ge(x)" alloy_x = 0.9 }
        doping{ constant{ name = "n-type" conc = 2e+19 } }
        contact{ name = "left_contact" }
}
region{
        line{ x = [ -350, -250 ] }
        ternary_constant{ name = "Si(1-x)Ge(x)" alloy_x = 0.9 }
        doping{ constant{ name = "n-type" conc = 2e+19 } }
}
region{
        line{ x = [ -250, 0 ] }
        ternary_constant{ name = "Si(1-x)Ge(x)" alloy_x = 0.9 }
}
region{
        array_x{ shift = 40 max = 50 }
        line{ x = [ 0, 23 ] }
        ternary_constant{ name = "Si(1-x)Ge(x)" alloy_x = 0.85 }
}
region{
        array_x{ shift = 40 max = 49 }
        line{ x = [ 23, 40 ] }
        binary{ name = "Ge" }
}
```

```
        region{
                line{ x = [ 2023, 2223 ] }
                ternary_constant{ name = "Si(1-x)Ge(x)" alloy_x = 0.9 }
        }
        region{
                line{ x = [ 2223, 2423 ] }
                ternary_constant{ name = "Si(1-x)Ge(x)" alloy_x = 0.9 }
                doping{ constant{ name = "p-type" conc = 4e+19 } }
        }
        region{
                line{ x = [ 2423, 2424 ] }
                ternary_constant{ name = "Si(1-x)Ge(x)" alloy_x = 0.9 }
                contact{ name = "right_contact" }
                doping{ constant{ name = "p-type" conc = 4e+19 } }
        }
}

impurities{
         donor{ name = "n-type" energy = 0.013 degeneracy = 2 }
         acceptor{ name = "p-type" energy = 0.011 degeneracy = 4 }
}

contacts{
        ohmic{ name = "right_contact" bias = [ 0 ] }
        ohmic{ name = "left_contact" bias = [ 0 ] }
}

strain{
        pseudomorphic_strain{ }
        output_strain_tensor{ }
```

```
        output_hydrostatic_strain{ boxes = "yes" }
}

classical{
        Gamma{ }
        L{ }
        X{ }
        HH{ }
        LH{ }
        SO{ }
        output_bandedges{ averaged = "no" }
        output_bandgap{ averaged = "no" }
}

quantum{
        region{
                name = "quantum_region"
                x = [ 960, 1023 ]
                boundary{ x = "dirichlet" }
                L{ num_ev = 10 }
                kp_8band{
                        num_electrons = 15
                        num_holes = 15
                        k_integration{ }
                        lapack{ }
                }
                output_wavefunctions{
                                max_num = 100
                                amplitudes = "no"
                                probabilities = "yes"
```

```
                }
            }
}

poisson{
        output_potential{ }
        output_electric_field{ }
}

run{
      solve_strain{ }
      solve_quantum{ }
      solve_poisson{ }
      outer_iteration{ iterations = 50 }
}
```

Bibliography

1. https://research.ibm.com/blog/2-nm-chip.
2. Report of the International Roadmap on Devices and Systems (2020).
3. Sugahara, S. & Nitta, J. Spin-Transistor Electronics: An Overview and Outlook. *Proceedings of the IEEE* **98,** 2124–2154 (2010).
4. Bader, S. & Parkin, S. Spintronics. *Annual Review of Condensed Matter Physics* **1,** 71–88 (2010).
5. Jansen, R. Silicon spintronics. *Nature Materials* **11,** 400–408 (2012).
6. Hirohata, A., Yamada, K., Nakatani, Y., Prejbeanu, I.-L., Diény, B., Pirro, P. & Hillebrands, B. Review on spintronics: Principles and device applications. *Journal of Magnetism and Magnetic Materials* **509,** 166711 (2020).
7. Hirohata, A. & Takanashi, K. Future perspectives for spintronic devices. *Journal of Physics D: Applied Physics* **47,** 193001 (2014).
8. Datta, S. & Das, B. Electronic analog of the electro-optic modulator. *Applied Physics Letters* **56,** 665–667 (1990).
9. Lindemann, M., Xu, G., Pusch, T., Michalzik, R., Hofmann, M. R., Žutić, I. & Gerhardt, N. C. Ultrafast spin-lasers. *Nature* **568,** 212–215 (2019).
10. Fiederling, R., Keim, M., Reuscher, G. a., Ossau, W., Schmidt, G., Waag, A. & Molenkamp, L. Injection and detection of a spin-polarized current in a light-emitting diode. *Nature* **402,** 787–790 (1999).
11. Fabian, J., Matos-Abiague, A., Ertler, C., Stano, P. & Zutic, I. Semiconductor spintronics. *arXiv preprint arXiv:0711.1461* (2007).
12. Winkler, R. Spin-dependent transport of carriers in semiconductors. *arXiv preprint cond-mat/0605390* (2006).
13. D'yakonov, M. I. *Spin Physics in Semiconductors* (Spinger-Verlag, 2004).

14. Winkler, R., Papadakis, S., De Poortere, E. & Shayegan, M. *Spin-Orbit Coupling in Two-Dimensional Electron and Hole Systems* (Springer, 2003).

15. Bychkov, Y. A. & Rashba, E. I. Properties of a 2D electron gas with lifted spectral degeneracy. *Soviet Journal of Experimental and Theoretical Physics Letters* **39,** 78 (1984).

16. Manchon, A., Koo, H., Nitta, J., Frolov, S. M. & Duine, R. A. New perspectives for Rashba spin–orbit coupling. *Nature Materials* **14,** 871 (2015).

17. Ganichev, S. D. & Golub, L. E. Interplay of Rashba/Dresselhaus spin splittings probed by photogalvanic spectroscopy –A review. *Physica Status Solidi (b)* **251,** 1801–1823 (2014).

18. Nitta, J., Akazaki, T., Takayanagi, H. & Enoki, T. Gate control of spin-orbit interaction in an inverted $In_{0.53}Ga_{0.47}As/In_{0.52}Al_{0.48}$ as heterostructure. *Physical Review Letters* **78,** 1335 (1997).

19. Engels, G., Lange, J., Schäpers, T. & Lüth, H. Experimental and theoretical approach to spin splitting in modulation-doped $In_xGa_{1-x}As/InP$ quantum wells for B→ 0. *Physical Review B* **55,** R1958 (1997).

20. Zutic, I., Fabian, J. & Das Sarma, S. Spintronics: Fundamentals and applications. *Reviews of Modern Physics* **76,** 323–410 (2004).

21. Morton, J. J., McCamey, D. R., Eriksson, M. A. & Lyon, S. A. Embracing the quantum limit in silicon computing. *Nature* **479,** 345–353 (2011).

22. Dushenko, S., Koike, M., Ando, Y., Shinjo, T., Myronov, M. & Shiraishi, M. Experimental Demonstration of Room-Temperature Spin Transport in *n*-Type Germanium Epilayers. *Physical Review Letters* **114,** 196602 (2015).

23. Hendrickx, N. W., Lawrie, W. I., Russ, M., van Riggelen, F., de Snoo, S. L., Schouten, R. N., Sammak, A., Scappucci, G. & Veldhorst, M. A four-qubit germanium quantum processor. *Nature* **591,** 580–585 (2021).

24. Li, P. & Dery, H. Spin-Orbit Symmetries of Conduction Electrons in Silicon. *Physical Review Letters* **107,** 107203 (2011).

25. Giorgioni, A., Paleari, S., Cecchi, S., Vitiello, E., Grilli, E., Isella, G., Jantsch, W., Fanciulli, M. & Pezzoli, F. Strong confinement-induced engineering of the g factor and lifetime of conduction electron spins in Ge quantum wells. *Nature Communications* **7,** 13886 (2016).

26. Zucchetti, C., Bollani, M., Isella, G., Zani, M., Finazzi, M. & Bottegoni, F. Doping dependence of the electron spin diffusion length in germanium. *APL Materials* **7,** 101122 (2019).

27. Rinaldi, C., Bertoli, S., Asa, M., Baldrati, L., Manzoni, C., Marangoni, M., Cerullo, G., Bianchi, M., Sordan, R., Bertacco, R. & Cantoni, M. Determination of the spin diffusion length in germanium by spin optical orientation and electrical spin injection. *Journal of Physics D: Applied Physics* **49,** 425104 (2016).

28. Yablonovitch, E., Jiang, H., Kosaka, H., Robinson, H., Rao, D. & Szkopek, T. Optoelectronic quantum telecommunications based on spins in semiconductors. *Proceedings of the IEEE* **91,** 761–780 (2003).

29. Morrison, C., Wiśniewski, P., Rhead, S. D., Foronda, J., Leadley, D. R. & Myronov, M. Observation of Rashba zero-field spin splitting in a strained germanium 2D hole gas. *Applied Physics Letters* **105,** 182401 (2014).

30. Zhou, Y., Han, W., Chang, L.-T., Xiu, F., Wang, M., Oehme, M., Fischer, I. A., Schulze, J., Kawakami, R. K. & Wang, K. L. Electrical spin injection and transport in germanium. *Physical Review B* **84,** 125323 (2011).

31. Wirths, S., Buca, D. & Mantl, S. Si–Ge–Sn alloys: From growth to applications. *Progress in Crystal Growth and Characterization of Materials* **62,** 1–39 (2016).

32. Gupta, S., Magyari-Köpe, B., Nishi, Y. & Saraswat, K. C. Achieving direct band gap in germanium through integration of Sn alloying and external strain. *Journal of Applied Physics* **113,** 073707 (2013).

33. Song, Z., Fan, W., Tan, C. S., Wang, Q., Nam, D., Zhang, D. H. & Sun, G. Band structure of $Ge_{1-x}Sn_x$ alloy: a full-zone 30-band k · p model. *New Journal of Physics* **21,** 073037 (2019).

34. Wirths, S., Geiger, R., von den Driesch, N., Mussler, G., Stoica, T., Mantl, S., Ikonic, Z., Luysberg, M., Chiussi, S., Hartmann, J. M., Sigg, H., Faist, J., Buca, D. & Grützmacher, D. Lasing in direct-bandgap GeSn alloy grown on Si. *Nature Photonics* **9,** 88–92 (2015).

35. Marchionni, A., Zucchetti, C., Ciccacci, F., Finazzi, M., Funk, H. S., Schwarz, D., Oehme, M., Schulze, J. & Bottegoni, F. Inverse spin-Hall effect in GeSn. *Applied Physics Letters* **118,** 212402 (2021).

36. Tai, C.-T., Chiu, P.-Y., Liu, C.-Y., Kao, H.-S., Harris, C. T., Lu, T.-M., Hsieh, C.-T., Chang, S.-W. & Li, J.-Y. Strain Effects on Rashba Spin-Orbit Coupling of 2D Hole Gases in GeSn/Ge Heterostructures. *Advanced Materials* **33,** 2007862 (2021).

37. Dyakonov, M. & Perel, V. Current-induced spin orientation of electrons in semiconductors. *Physics Letters A* **35,** 459–460 (1971).

38. Hirsch, J. E. Spin Hall Effect. *Physical Review Letters* **83,** 1834–1837 (1999).

39. Maekawa, S., Valenzuela, S. O., Saitoh, E. & Kimura, T. *Spin current* (Oxford University Press, 2017).

40. Kaviraj, B. & Sinha, J. Relativistic torques induced by currents in magnetic materials: physics and experiments. *RSC Advances* **8,** 25079–25093 (2018).

41. Ganichev, S. D., Bel'kov, V. V., Golub, L. E., Ivchenko, E. L., Schneider, P., Giglberger, S., Eroms, J., De Boeck, J., Borghs, G., Wegscheider, W., Weiss, D. & Prettl, W. Experimental Separation of Rashba and Dresselhaus Spin Splittings in Semiconductor Quantum Wells. *Physical Review Letters* **92,** 256601 (2004).

42. Rashba, E. I. The properties of semiconductors with an extremum loop. I. Cyclotron and combinational resonance in a magnetic field perpendicular to the plane of the loop. *Soviet Physics, Solid State* **2,** 1109–1122 (1960).

43. Rashba, E. I. The properties of semiconductors with an extremum loop: II. Magnetic susceptibility in a field perpendicular to the plane of the loop. *Soviet Physics, Solid State* **2,** 1692 (1960).

44. Rashba, E. I. & Boiko, I. I. The properties of semiconductors with extremum loops. III. Behavior in a magnetic field parallel to the plane of the loop. *Soviet Physics, Solid State* **3,** 922–934 (1961).

45. Rashba, E. I. & Sheka, V. I. The properties of semiconductors with extremum loops. IV. Angular dependence of combination resonance in a strong magnetic field. *Soviet Physics, Solid State* **3,** 1718–1723 (1962).

46. Dresselhaus, G. Spin-Orbit Coupling Effects in Zinc Blende Structures. *Physical Review* **100,** 580–586 (1955).

47. Balocchi, A., Duong, Q. H., Renucci, P., Liu, B. L., Fontaine, C., Amand, T., Lagarde, D. & Marie, X. Full Electrical Control of the Electron Spin Relaxation in GaAs Quantum Wells. *Physical Review Letters* **107,** 136604 (2011).

48. Virgilio, M. & Grosso, G. Optical spin orientation in strained Ge/SiGe quantum wells: A tight-binding approach. *Physical Review B* **80,** 205309 (2009).

49. Dyakonov, M. & Perel, V. Possibility of Orienting Electron Spins with Current. *Soviet Journal of Experimental and Theoretical Physics Letters* **13,** 467 (1971).

50. Sinova, J., Valenzuela, S. O., Wunderlich, J., Back, C. H. & Jungwirth, T. Spin Hall effects. *Reviews of Modern Physics* **87,** 1213–1260 (2015).

51. Loren, E. J., Rioux, J., Lange, C., Sipe, J. E., van Driel, H. M. & Smirl, A. L. Hole spin relaxation and intervalley electron scattering in germanium. *Physical Review B* **84,** 214307 (2011).

52. Rinaldi, C., Cantoni, M., Marangoni, M., Manzoni, C., Cerullo, G. & Bertacco, R. Wide-range optical spin orientation in Ge from near-infrared to visible light. *Physical Review B* **90,** 161304 (2014).

53. Hall, E. H. On a New Action of the Magnet on Electric Currents. *American Journal of Mathematics* **2,** 287 (1879).

54. Bottegoni, F., Zucchetti, C., Isella, G., Bollani, M., Finazzi, M. & Ciccacci, F. Spin-charge interconversion in heterostructures based on group-IV semiconductors. *La Rivista del Nuovo Cimento* **43,** 45–96 (2020).

55. Murakami, S., Nagaosa, N. & Zhang, S.-C. Dissipationless Quantum Spin Current at Room Temperature. *Science* **301,** 1348–1351 (2003).

56. Sinova, J., Culcer, D., Niu, Q., Sinitsyn, N. A., Jungwirth, T. & MacDonald, A. H. Universal Intrinsic Spin Hall Effect. *Physical Review Letters* **92,** 126603 (2004).

57. Onsager, L. Reciprocal Relations in Irreversible Processes. II. *Physical Review* **38,** 2265–2279 (1931).

58. Trier, F., Noël, P., Kim, J.-V., Attané, J.-P., Vila, L. & Bibes, M. Oxide spin-orbitronics: spin-charge interconversion and topological spin textures. *arXiv preprint arXiv:2103.16271* (2021).

59. Wunderlich, J., Irvine, A., Sinova, J., Park, B. G., Zârbo, L., Xu, X., Kaestner, B., Novák, V. & Jungwirth, T. Spin-injection Hall effect in a planar photovoltaic cell. *Nature Physics* **5,** 675–681 (2009).

60. Wunderlich, J., Park, B.-G., Irvine, A. C., Zârbo, L. P., Rozkotová, E., Nemec, P., Novák, V., Sinova, J. & Jungwirth, T. Spin Hall effect transistor. *Science* **330,** 1801–1804 (2010).

61. Okamoto, N., Kurebayashi, H., Harii, K., Kajiwara, Y., Beere, H., Farrer, I., Trypiniotis, T., Ando, K., Ritchie, D. A., Barnes, C. H. W. & Saitoh, E. Spin current depolarization under high electric fields in undoped InGaAs. *Applied Physics Letters* **98,** 242104 (2011).

62. Okamoto, N., Kurebayashi, H., Trypiniotis, T., Farrer, I., Ritchie, D., Saitoh, E., Sinova, J., Mašek, J., Jungwirth, T. & Barnes, C. Electric control of the spin Hall effect by intervalley transitions. *Nature Materials* **13,** 932–937 (2014).

63. Ando, K. & Saitoh, E. Observation of the inverse spin Hall effect in silicon. *Nature Communications* **3,** 629 (2012).

64. Bakun, A., Zakharchenya, B., Rogachev, A., Tkachuk, M. & Fleĭsher, V. Observation of a surface photocurrent caused by optical orientation of electrons in a semiconductor. *Soviet Journal of Experimental and Theoretical Physics Letters* **40,** 1293 (1984).

65. Kato, Y. K., Myers, R. C., Gossard, A. C. & Awschalom, D. D. Observation of the Spin Hall Effect in Semiconductors. *Science* **306,** 1910–1913 (2004).

66. Wunderlich, J., Kaestner, B., Sinova, J. & Jungwirth, T. Experimental Observation of the Spin-Hall Effect in a Two-Dimensional Spin-Orbit Coupled Semiconductor System. *Physical Review Letters* **94,** 047204 (2005).

67. Liu, L., Buhrman, R. & Ralph, D. Review and analysis of measurements of the spin Hall effect in platinum. *arXiv preprint arXiv:1111.3702* (2011).

68. Liu, L., Pai, C.-F., Li, Y., Tseng, H. W., Ralph, D. C. & Buhrman, R. A. Spin-Torque Switching with the Giant Spin Hall Effect of Tantalum. *Science* **336,** 555–558 (2012).

69. Valenzuela, S. O. & Tinkham, M. Direct electronic measurement of the spin Hall effect. *Nature* **442,** 176–179 (2006).

70. Mosendz, O., Vlaminck, V., Pearson, J. E., Fradin, F. Y., Bauer, G. E. W., Bader, S. D. & Hoffmann, A. Detection and quantification of inverse spin Hall effect from spin pumping in permalloy/normal metal bilayers. *Physical Review B* **82,** 214403 (2010).

71. Rojas-Sánchez, J.-C., Cubukcu, M., Jain, A., Vergnaud, C., Portemont, C., Ducruet, C., Barski, A., Marty, A., Vila, L., Attané, J.-P., Augendre, E., Desfonds, G., Gambarelli, S., Jaffrès, H., George, J.-M. & Jamet, M. Spin pumping and inverse spin Hall effect in germanium. *Physical Review B* **88,** 064403 (2013).

72. Bottegoni, F., Zucchetti, C., Dal Conte, S., Frigerio, J., Carpene, E., Vergnaud, C., Jamet, M., Isella, G., Ciccacci, F., Cerullo, G. & Finazzi, M. Spin-Hall Voltage over a Large Length Scale in Bulk Germanium. *Physical Review Letters* **118,** 167402 (2017).

73. Lampel, G. Nuclear Dynamic Polarization by Optical Electronic Saturation and Optical Pumping in Semiconductors. *Physical Review Letters* **20,** 491–493 (1968).

74. D'yakonov, M. I. & Perel, V. I. *Theory of Optical Spin Orientation of Electrons and Nuclei in Semiconductors* (eds Meier, F. & Zakharchenya, B. P.) In Optical Orientation, 11–71 (1984).

75. Corney, A. *Atomic and Laser Spectroscopy* (Clarendon Press, Oxford University Press, 1976).

76. Fox, M. *Optical properties of solids* (Oxford University Press, 2010).

77. Pierce, D. T. & Meier, F. Photoemission of spin-polarized electrons from GaAs. *Physical Review B* **13,** 5484–5500 (1976).

78. Lange, C., Isella, G., Chrastina, D., Pezzoli, F., Köster, N. S., Woscholski, R. & Chatterjee, S. Spin band-gap renormalization and hole spin dynamics in Ge/SiGe quantum wells. *Physical Review B* **85,** 241303 (2012).

79. Li, P., Trivedi, D. & Dery, H. Spin-dependent optical properties in strained silicon and germanium. *Physical Review B* **87,** 115203 (2013).

80. Prins, M. W. J., van Kempen, H., van Leuken, H., de Groot, R. A., Roy, W. V. & Boeck, J. D. Spin-dependent transport in metal/semiconductor tunnel junctions. *Journal of Physics: Condensed Matter* **7,** 9447–9464 (1995).

81. Poole, C. P. J. *Electron Spin Resonance: A Comprehensive Treatise on Experimental Techniques* (Dover Publication, 1996).

82. Hanle, W. Über magnetische Beeinflussung der Polarisation der Resonanzfluoreszenz. *Zeitschrift fur Physik* **30,** 93–105 (1924).

83. Zakharchenya, B., Kalevich, V., Kul'kov, V. & Flejsher, V. Optical orientation of electron-nuclear spin-system of semiconductor in a sloping magnetic field. *Fizika Tverdogo Tela* **23,** 1387–1394 (1981).

84. Schreiner, M., Krapf, M., Pascher, H., Denninger, G., Weimann, G. & Schlapp, W. Optically detected electron spin polarization and Hanle effect in AlGaAs/GaAs heterostructures. *Superlattices and Microstructures* **11,** 409–414 (1992).

85. Averkiev, N. S., Golub, L. E., Gurevich, A. S., Evtikhiev, V. P., Kochereshko, V. P., Platonov, A. V., Shkolnik, A. S. & Efimov, Y. P. Spin-relaxation anisotropy in asymmetrical (001) $Al_xGa_{1-x}As$ quantum wells from Hanle-effect measurements: Relative strengths of Rashba and Dresselhaus spin-orbit coupling. *Physical Review B* **74,** 033305 (2006).

86. Dzhioev, R., Aksyanov, I., Lazarev, M. & Ninua, O. Study of the Hanle effect with the transverse component of the electron spin orientation in III–V semiconductors. *Physics of the Solid State* **48,** 2270–2274 (2006).

87. Elliott, R. J. Theory of the Effect of Spin-Orbit Coupling on Magnetic Resonance in Some Semiconductors. *Physical Review* **96,** 266–279 (1954).

88. Yafet, Y. g Factors and Spin-Lattice Relaxation of Conduction Electrons. *Solid State Physics* **14,** 1–98 (1963).

89. Pikus, G. E. & Titkov, A. N. *Spin Relaxation under Optical Orientation in Semiconductors* (eds Meier, F. & Zakharchenya, B. P.) In Optical Orientation, 73–131 (1984).

90. Bir, G. L., Aronov, A. G. & Pikus, G. E. Spin relaxation of electrons due to scattering by holes. *Soviet Journal of Experimental and Theoretical Physics* **42,** 705 (1976).

91. Rossi, S., Vitiello, E. & Pezzoli, F. *Optical Spin Orientation in Ge-Based Heterostructures.* (eds Lockwood, D. J. & Pavesi, L.) In Silicon Photonics IV, 237–282 (Springer, 2021).

92. Ashcroft, N. W. & Mermin, N. D. *Solid-State Physics* (Harcourt College Publishers, 1976).

93. Olesinski, R. W. & Abbaschian, G. J. The Ge-Si (Germanium-Silicon) System. *Bulletin of Alloy Phase Diagrams* **5,** 180–183 (1984).

94. Dismukes, J. P., Ekstrom, L. & Paff, R. J. Lattice Parameter and Density in Germanium-Silicon Alloys1. *The Journal of Physical Chemistry* **68,** 3021–3027 (1964).

95. Herzog, H.-J. *Crystal structure, lattice parameters and liquidus-solidus curve of the SiGe system* In E. Kasper and K. Lyutovich, editors, Properties of Silicon Germanium and SiGe: Carbon, 45–49 (1999).

96. Kasper, E., Schuh, A., Bauer, G., Holländer, B. & Kibbel, H. Test of Vegard's law in thin epitaxial SiGe layers. *Journal of Crystal Growth* **157,** 68–72 (1995).

97. Paul, D. J. Si/SiGe heterostructures: from material and physics to devices and circuits. *Semiconductor Science and Technology* **19,** R75–R108 (2004).

98. Stöhr, H. & Klemm, W. Über Zweistoffsysteme mit Germanium. I. Germanium/Aluminium, Germanium/Zinn und Germanium/Silicium. *Zeitschrift für anorganische und allgemeine Chemie* **241,** 305–323 (1939).

99. Bhargava, N., Coppinger, M., Prakash Gupta, J., Wielunski, L. & Kolodzey, J. Lattice constant and substitutional composition of GeSn alloys grown by molecular beam epitaxy. *Applied Physics Letters* **103,** 041908 (2013).

100. Olesinski, R. & Abbaschian, G. The Ge-Sn (germanium-tin) system. *Bulletin of Alloys Phase Diagrams* **5,** 265–271.

101. Claflin, B., Grzybowski, G. J., Ware, M. E., Zollner, S. & Kiefer, A. M. Process for Growth of Group-IV Alloys Containing Tin by Remote Plasma Enhanced Chemical Vapor Deposition. *Frontiers in Materials* **7,** 44 (2020).

102. Doherty, J., Biswas, S., Galluccio, E., Broderick, C. A., Garcia-Gil, A., Duffy, R., O'Reilly, E. P. & Holmes, J. D. Progress on Germanium–Tin Nanoscale Alloys. *Chemistry of Materials* **32,** 4383–4408 (2020).

103. Taraci, J., Tolle, J., Kouvetakis, J., McCartney, M. R., Smith, D. J., Menendez, J. & Santana, M. A. Simple chemical routes to diamond-cubic germanium–tin alloys. *Applied Physics Letters* **78,** 3607–3609 (2001).

104. Vincent, B., Gencarelli, F., Bender, H., Merckling, C., Douhard, B., Petersen, D. H., Hansen, O., Henrichsen, H. H., Meersschaut, J., Vandervorst, W., Heyns, M., Loo, R. & Caymax, M. Undoped and in-situ B doped GeSn epitaxial growth on Ge by atmospheric pressure-chemical vapor deposition. *Applied Physics Letters* **99,** 152103 (2011).

105. Stringfellow, G. B. Epitaxy. *Reports on Progress in Physics* **45,** 469–525 (1982).

106. Herman, M. A. Silicon-Based Heterostructures: Strained-Layer Growth by Molecular Beam Epitaxy. *Crystal Research and Technology* **34,** 583–595 (1999).

107. Wood, D. M. & Zunger, A. Epitaxial effects on coherent phase diagrams of alloys. *Physical Review B* **40,** 4062–4089 (1989).

108. Kittel, C., McEuen, P. & McEuen, P. *Introduction to solid state physics* (Wiley New York, 1996).

109. Sze, S. M. Physics of semiconductor devices (2nd edition) (1981).

110. Höchst, H. & Hernández-Calderón, I. Angular resolved photoemission of InSb(001) and heteroepitaxial films of α-Sn(001). *Surface Science* **126,** 25–31 (1983).

111. Tsidilkovski, J. Electron Spectrum of Gapless Semiconductors. *Springer Series in Solid-State Sciences* (2012).

112. Kufner, S., Furthmuller, J., Matthes, L., Fitzner, M. & Bechstedt, F. Structural and electronic properties of α-tin nanocrystals from first principles. *Physical Review B* **87,** 235307 (2013).

113. Groves, S. & Paul, W. Band Structure of Gray Tin. *Physical Review Letters* **11,** 194–196 (1963).

114. Pollak, F. H., Cardona, M., Higginbotham, C. W., Herman, F. & Van Dyke, J. P. Energy-Band Structure and Optical Spectrum of Grey Tin. *Physical Review B* **2,** 352–363 (1970).

115. Becke, A. D. & Johnson, E. R. A simple effective potential for exchange. *The Journal of Chemical Physics* **124,** 221101 (2006).

116. Rojas-Sánchez, J.-C., Oyarzún, S., Fu, Y., Marty, A., Vergnaud, C., Gambarelli, S., Vila, L., Jamet, M., Ohtsubo, Y., Taleb-Ibrahimi, A., Le Fèvre, P., Bertran, F., Reyren, N., George, J.-M. & Fert, A. Spin to Charge Conversion at Room Temperature by Spin Pumping into a New Type of Topological Insulator: α-Sn Films. *Physical Review Letters* **116,** 096602 (2016).

117. Barfuss, A., Dudy, L., Scholz, M. R., Roth, H., Höpfner, P., Blumenstein, C., Landolt, G., Dil, J. H., Plumb, N. C., Radovic, M., Bostwick, A., Rotenberg, E., Fleszar, A., Bihlmayer, G., Wortmann, D., Li, G., Hanke, W., Claessen, R. & Schäfer, J. Elemental Topological Insulator with Tunable Fermi Level: Strained α-Sn on InSb(001). *Physical Review Letters* **111,** 157205 (2013).

118. Ohtsubo, Y., Le Fèvre, P., Bertran, F. ç. & Taleb-Ibrahimi, A. Dirac Cone with Helical Spin Polarization in Ultrathin α-Sn(001) Films. *Physical Review Letters* **111,** 216401 (2013).

119. Moontragoon, P., Ikonić, Z. & Harrison, P. Band structure calculations of Si–Ge–Sn alloys: achieving direct band gap materials. *Semiconductor Science and Technology* **22,** 742–748 (2007).

120. Weber, J. & Alonso, M. I. Near-band-gap photoluminescence of Si-Ge alloys. *Physical Review B* **40,** 5683–5693 (1989).

121. Mathews, J., Roucka, R., Xie, J., Yu, S.-Q., Menéndez, J. & Kouvetakis, J. Extended performance GeSn/Si(100) p-i-n photodetectors for full spectral range telecommunication applications. *Applied Physics Letters* **95,** 133506 (2009).

122. Gassenq, A., Gencarelli, F., Campenhout, J. V., Shimura, Y., Loo, R., Narcy, G., Vincent, B. & Roelkens, G. GeSn/Ge heterostructure short-wave infrared photodetectors on silicon. *Optics Express* **20,** 27297–27303 (2012).

123. Lu Low, K., Yang, Y., Han, G., Fan, W. & Yeo, Y.-C. Electronic band structure and effective mass parameters of $Ge_{1-x}Sn_x$ alloys. *Journal of Applied Physics* **112,** 103715 (2012).

124. Tonkikh, A. A., Eisenschmidt, C., Talalaev, V. G., Zakharov, N. D., Schilling, J., Schmidt, G. & Werner, P. Pseudomorphic GeSn/Ge(001) quantum wells: Examining indirect band gap bowing. *Applied Physics Letters* **103,** 032106 (2013).

125. Al-Kabi, S., Ghetmiri, S. A., Margetis, J., Pham, T., Zhou, Y., Dou, W., Collier, B., Quinde, R., Du, W., Mosleh, A., Liu, J., Sun, G., Soref, R. A., Tolle, J., Li, B., Mortazavi, M., Naseem, H. A. & Yu, S.-Q. An optically pumped 2.5µm GeSn laser on Si operating at 110 K. *Applied Physics Letters* **109,** 171105 (2016).

126. Zhou, Y., Dou, W., Du, W., Ojo, S., Tran, H., Ghetmiri, S. A., Liu, J., Sun, G., Soref, R., Margetis, J., Tolle, J., Li, B., Chen, Z., Mortazavi, M. & Yu, S.-Q. Optically Pumped GeSn Lasers Operating at 270 K with Broad Waveguide Structures on Si. *ACS Photonics* **6,** 1434–1441 (2019).

127. Tran, H., Pham, T., Margetis, J., Zhou, Y., Dou, W., Grant, P. C., Grant, J. M., Al-Kabi, S., Sun, G., Soref, R. A., Tolle, J., Zhang, Y.-H., Du, W., Li, B., Mortazavi, M. & Yu, S.-Q. Si-Based GeSn Photodetectors toward Mid-Infrared Imaging Applications. *ACS Photonics* **6,** 2807–2815 (2019).

128. Pham, T., Du, W., Tran, H., Margetis, J., Tolle, J., Sun, G., Soref, R. A., Naseem, H. A., Li, B. & Yu, S.-Q. Systematic study of Si-based GeSn photodiodes with 2.6 μm detector cutoff for short-wave infrared detection. *Optics Express* **24,** 4519–4531 (2016).

129. Davies, J. H. *The physics of low-dimensional semiconductors: an introduction* (Cambridge university press, 1998).

130. Christen, J., Bimberg, D., Steckenborn, A. & Weimann, G. Localization induced electron-hole transition rate enhancement in GaAs quantum wells. *Applied Physics Letters* **44,** 84–86 (1984).

131. Virgilio, M. & Grosso, G. Type-I alignment and direct fundamental gap in SiGe based heterostructures. *Journal of Physics: Condensed Matter* **18,** 1021–1031 (2006).

132. Schäffler, F. High-mobility Si and Ge structures. *Semiconductor Science and Technology* **12,** 1515–1549 (1997).

133. Jain, S., Willis, J. & F.R.S., R. B. A review of theoretical and experimental work on the structure of Ge_xSi_{1-x} strained layers and superlattices, with extensive bibliography. *Advances in Physics* **39,** 127–190 (1990).

134. Jancu, J.-M., Scholz, R., Beltram, F. & Bassani, F. Empirical spds* tight-binding calculation for cubic semiconductors: General method and material parameters. *Physical Review B* **57,** 6493–6507 (1998).

135. Gatti, E., Grilli, E., Guzzi, M., Chrastina, D., Isella, G. & von Känel, H. Room temperature photoluminescence of Ge multiple quantum wells with Ge-rich barriers. *Applied Physics Letters* **98,** 031106 (2011).

136. Giorgioni, A., Gatti, E., Grilli, E., Chernikov, A., Chatterjee, S., Chrastina, D., Isella, G. & Guzzi, M. Photoluminescence decay of direct and indirect transitions in Ge/SiGe multiple quantum wells. *Journal of Applied Physics* **111,** 013501 (2012).

137. Chaisakul, P., Marris-Morini, D., Frigerio, J., Chrastina, D., Rouifed, M.-S., Cecchi, S., Crozat, P., Isella, G. & Vivien, L. Integrated germanium optical interconnects on silicon substrates. *Nature Photonics* **8,** 482–488 (2014).

138. Kuo, Y.-H., Lee, Y. K., Ge, Y., Ren, S., Roth, J. E., Kamins, T. I., Miller, D. A. & Harris, J. S. Strong quantum-confined Stark effect in germanium quantum-well structures on silicon. *Nature* **437,** 1334–1336 (2005).

139. Lin, C.-Y., Ye, H.-Y., Lu, F.-L., Lan, H. S. & Liu, C. W. Biaxial strain effects on photoluminescence of Ge/strained GeSn/Ge quantum well. *Optical Materials Express* **8,** 2795–2802 (2018).

140. Maczko, H. S., Kudrawiec, R. & Gladysiewicz, M. Strain engineering of transverse electric and transverse magnetic mode of material gain in GeSn/SiGeSn quantum wells. *Scientific Reports* **9,** 1–14 (2019).

141. Qian, L., Fan, W. J., Tan, C. S. & Zhang, D. H. Temperature enhanced spontaneous emission rate spectra in GeSn/Ge quantum wells. *Optical Materials Express* **7,** 800–807 (2017).

142. Gul, Y., Myronov, M., Holmes, S. & Pepper, M. Activated and Metallic Conduction in p-Type Modulation-Doped Ge-Sn Devices. *Physical Review Applied* **14,** 054064 (2020).

143. Stange, D., von den Driesch, N., Rainko, D., Schulte-Braucks, C., Wirths, S., Mussler, G., Tiedemann, A. T., Stoica, T., Hartmann, J. M., Ikonic, Z., Mantl, S., Grützmacher, D. & Buca, D. Study of GeSn based heterostruc-

tures: towards optimized group IV MQW LEDs. *Optics Express* **24,** 1358–1367 (2016).

144. O'Reilly, E. P. Valence band engineering in strained-layer structures. *Semiconductor Science and Technology* **4,** 121–137 (1989).

145. Chang, S.-W. & Chuang, S. L. Theory of Optical Gain of Ge-$Si_xGe_ySn_{1-x-y}$ Quantum-Well Lasers. *IEEE Journal of Quantum Electronics* **43,** 249–256 (2007).

146. Chang, G.-E., Chang, S.-W. & Chuang, S. L. Theory for n-type doped, tensile-strained Ge-$Si_xGe_ySn_{1-x-y}$ quantum-well lasers at telecom wavelength. *Optics Express* **17,** 11246–11258 (2009).

147. Brunner, K. Si/Ge nanostructures. *Reports on Progress in Physics* **65,** 27–72 (2001).

148. Rogowicz, E., Kopaczek, J., Kutrowska-Girzycka, J., Myronov, M., Kudrawiec, R. & Syperek, M. Carrier Dynamics in Thin Germanium–Tin Epilayers. *ACS Applied Electronic Materials* **3,** 344–352 (2021).

149. Song, Z., Fan, W., Tan, C. S., Wang, Q., Nam, D., Zhang, D. H. & Sun, G. Band Structure of Strained Ge_{1-x} Sn_x Alloy: A Full-Zone 30-Band $k \cdot p$ Model. *IEEE Journal of Quantum Electronics* **56,** 1–8 (2020).

150. Rainko, D., Ikonic, Z., Elbaz, A., von den Driesch, N., Stange, D., Herth, E., Boucaud, P., El Kurdi, M., Grützmacher, D. & Buca, D. Impact of tensile strain on low Sn content GeSn lasing. *Scientific Reports* **9,** 259 (2019).

151. Bastard, G. Superlattice band structure in the envelope-function approximation. *Physical Review B* **24,** 5693–5697 (1981).

152. Bastard, G. Theoretical investigations of superlattice band structure in the envelope-function approximation. *Physical Review B* **25,** 7584–7597 (1982).

153. Altarelli, M. Electronic structure of two-dimensional semiconductor systems. *Journal of Luminescence* **30,** 472–487 (1985).

154. Kane, E. O. Band structure of indium antimonide. *Journal of Physics and Chemistry of Solids* **1,** 249–261 (1957).

155. Dingle, R., Störmer, H. L., Gossard, A. C. & Wiegmann, W. Electron mobilities in modulation-doped semiconductor heterojunction superlattices. *Applied Physics Letters* **33,** 665–667 (1978).

156. Weisbuch, C. & Vinter, B. *Quantum Semiconductor Structures. Fundamentals and Applications* (Academic Press, 1991).

157. Morrison, C., Casteleiro, C., Leadley, D. R. & Myronov, M. Complex quantum transport in a modulation doped strained Ge quantum well heterostructure with a high mobility 2D hole gas. *Applied Physics Letters* **109,** 102103 (2016).

158. Känel, H. v., Kummer, M., Isella, G., Müller, E. & Hackbarth, T. Very high hole mobilities in modulation-doped Ge quantum wells grown by low-energy plasma enhanced chemical vapor deposition. *Applied Physics Letters* **80,** 2922–2924 (2002).

159. Uomi, K., Mishima, T. & Chinone, N. Modulation-Doped Multi-Quantum Well (MD-MQW) Lasers. II. Experiment. *Japanese Journal of Applied Physics* **29,** 88–94 (1990).

160. Linh, N. T. & Delagebeaudeuf, D. in *The Physics of Submicron Structures* 53–61 (Springer, 1984).

161. Zhu, C., Ferreyra, R. A. & Morkoç, H. in *Wiley Encyclopedia of Electrical and Electronics Engineering* 1–50 (2015).

162. Ibach, H. & Lüth, H. *Solid-state physics: an introduction to theory and experiment* (Springer Science & Business Media, 2012).

163. Knap, W., Fal'ko, V. I., Frayssinet, É., Lorenzini, P., Grandjean, N., Maude, D. K., Karczewski, G., Brandt, B., Lusakowski, J., Grzegory, I., Leszczynski, M., Prystawko, P., Skierbiszewski, C., Porowski, S., Hu, X., Simin, G., Khan, M. A. & Shur, M. S. Spin and interaction effects in Shubnikov–de

Haas oscillations and the quantum Hall effect in GaN/AlGaN heterostructures. *Journal of Physics: Condensed Matter* **16,** 3421–3432 (2004).

164. Miller, D. A. B., Chemla, D. S., Damen, T. C., Gossard, A. C., Wiegmann, W., Wood, T. H. & Burrus, C. A. Band-Edge Electroabsorption in Quantum Well Structures: The Quantum-Confined Stark Effect. *Physical Review Letters* **53,** 2173–2176 (1984).

165. Bastard, G., Mendez, E. E., Chang, L. L. & Esaki, L. Variational calculations on a quantum well in an electric field. *Physical Review B* **28,** 3241–3245 (1983).

166. Bonfanti, M., Grilli, E., Guzzi, M., Virgilio, M., Grosso, G., Chrastina, D., Isella, G., von Känel, H. & Neels, A. Optical transitions in Ge/SiGe multiple quantum wells with Ge-rich barriers. *Physical Review B* **78,** 041407 (2008).

167. Cho, H., Kapur, P. & Saraswat, K. Power comparison between high-speed electrical and optical interconnects for interchip communication. *Journal of Lightwave Technology* **22,** 2021–2033 (2004).

168. Kibar, O., Van Blerkom, D., Fan, C. & Esener, S. Power minimization and technology comparisons for digital free-space optoelectronic interconnections. *Journal of Lightwave Technology* **17,** 546–555 (1999).

169. Arad, U., Redmard, E., Shamay, M., Averboukh, A., Levit, S. & Efron, U. Development of a large high-performance 2-D array of GaAs-AlGaAs multiple quantum-well modulators. *IEEE Photonics Technology Letters* **15,** 1531–1533 (2003).

170. Liu, C.-P., Seeds, A., Chadha, J., Stavrino, N., Parry, G., Whitehead, M., Krysa, A. & Roberts, J. Design, Fabrication and Characterisation of Normal-Incidence 1.56-μm Multiple-Quantum-Well Asymmetric Fabry-Perot Modulators for Passive Picocells. *IEICE Transactions on Electronics* **E85-C** (2003).

171. Helman, N., Roth, J., Bour, D., Altug, H. & Miller, D. Misalignment-tolerant surface-normal low-voltage modulator for optical interconnects. *IEEE Journal of Selected Topics in Quantum Electronics* **11,** 338–342 (2005).

172. Virgilio, M. & Grosso, G. Quantum-confined Stark effect in Ge/SiGe quantum wells: a tight-binding description. *Physical Review B* **77,** 165315 (2008).

173. Paul, D. J. 8-band **k**.**p** modeling of the quantum confined Stark effect in Ge quantum wells on Si substrates. *Physical Review B* **77,** 155323 (2008).

174. Sun, L., Yuan, G., Gao, L., Yang, J., Chhowalla, M., Gharahcheshmeh, M. H., Gleason, K. K., Choi, Y. S., Hong, B. H. & Liu, Z. Chemical vapour deposition. *Nature Reviews Methods Primers* **1,** 5 (2021).

175. Choy, K. Chemical vapour deposition of coatings. *Progress in Materials Science* **48,** 57–170 (2003).

176. Rosenblad, C., Deller, H. R., Dommann, A., Meyer, T., Schroeter, P. & von Känel, H. Silicon epitaxy by low-energy plasma enhanced chemical vapor deposition. *Journal of Vacuum Science & Technology A* **16,** 2785–2790 (1998).

177. Rosenblad, C., Deller, H., Graf, T., Müller, E. & von Känel, H. Low temperature epitaxial growth by LEPECVD. *Journal of Crystal Growth* **188,** 125–130 (1998).

178. Kummer, M., Rosenblad, C., Dommann, A., Hackbarth, T., Höck, G., Zeuner, M., Müller, E. & von Känel, H. Low energy plasma enhanced chemical vapor deposition. *Materials Science and Engineering: B* **89,** 288–295 (2002).

179. Kim, H., Taylor, N., Bramblett, T. R. & Greene, J. E. Kinetics of $Si_{1-x}Ge_x$ (001) growth on Si (001) 2×1 by gas-source molecular-beam epitaxy from Si_2H_6 and Ge_2H_6. *Journal of Applied Physics* **84,** 6372–6381 (1998).

180. Rosenblad, C., Känel, H. v., Kummer, M., Dommann, A. & Müller, E. A plasma process for ultrafast deposition of SiGe graded buffer layers. *Applied Physics Letters* **76,** 427–429 (2000).

181. Isella, G., Chrastina, D., Rössner, B., Hackbarth, T., Herzog, H.-J., König, U. & von Känel, H. Low-energy plasma-enhanced chemical vapor deposition for strained Si and Ge heterostructures and devices. *Solid-State Electronics* **48,** 1317–1323 (2004).

182. Thurmond, C. D., Trumbore, F. A. & Kowalchik, M. Germanium Solidus Curves. *The Journal of Chemical Physics* **25,** 799–800 (1956).

183. Trumbore, F. A. Solid Solubilities and Electrical Properties of Tin in Germanium Single Crystals. *Journal of The Electrochemical Society* **103,** 597 (1956).

184. Weisshaupt, D., Jahandar, P., Colston, G., Allred, P., Schulze, J. & Myronov, M. Impact of Sn segregation on $Ge_{1-x}Sn_x$ epi-layers growth by RP-CVD. *In 2017 40th International Convention on Information and Communication Technology, Electronics and Microelectronics (MIPRO),* 43–47 (2017).

185. Gencarelli, F., Vincent, B., Souriau, L., Richard, O., Vandervorst, W., Loo, R., Caymax, M. & Heyns, M. Low-temperature Ge and GeSn Chemical Vapor Deposition using Ge_2H_6. *Thin Solid Films* **520,** 3211–3215 (2012).

186. Bauer, M., Ritter, C., Crozier, P. A., Ren, J., Menendez, J., Wolf, G. & Kouvetakis, J. Synthesis of ternary SiGeSn semiconductors on Si(100) via Sn_xGe_{1-x} buffer layers. *Applied Physics Letters* **83,** 2163–2165 (2003).

187. Kouvetakis, J. & Chizmeshya, A. V. G. New classes of Si-based photonic materials and device architectures via designer molecular routes. *Journal of Materials Chemistry* **17,** 1649–1655 (2007).

188. Gencarelli, F., Vincent, B., Demeulemeester, J., Vantomme, A., Moussa, A., Franquet, A., Kumar, A., Bender, H., Meersschaut, J., Vandervorst, W., Loo, R., Caymax, M., Temst, K. & Heyns, M. Crystalline Properties and Strain Relaxation Mechanism of CVD Grown GeSn. *ECS Journal of Solid State Science and Technology* **2,** P134–P137 (2013).

189. Xie, J., Chizmeshya, A. V. G., Tolle, J., D'Costa, V. R., Menendez, J. & Kouvetakis, J. Synthesis, Stability Range, and Fundamental Properties of SiGeSn Semiconductors Grown Directly on Si(100) and Ge(100) Platforms. *Chemistry of Materials* **22,** 3779–3789 (2010).

190. Bauer, M. R., Tolle, J., Bungay, C., Chizmeshya, A. V., Smith, D. J., Menéndez, J. & Kouvetakis, J. Tunable band structure in diamond–cubic tin–germanium alloys grown on silicon substrates. *Solid State Communications* **127,** 355–359 (2003).

191. Loo, R., Wang, G., Souriau, L., Lin, J., Takeuchi, S., Brammertz, G. & Caymax, M. Epitaxial Ge on Standard STI Patterned Si Wafers: High Quality Virtual Substrates for Ge pMOS and III/V nMOS. *ECS Transactions* **25,** 335–350 (2019).

192. Shah, V., Dobbie, A., Myronov, M. & Leadley, D. High quality relaxed Ge layers grown directly on a Si(001) substrate. *Solid-State Electronics* **62,** 189–194 (2011).

193. Colace, L., Masini, G., Galluzzi, F., Assanto, G., Capellini, G., Di Gaspare, L., Palange, E. & Evangelisti, F. Metal-semiconductor-metal near-infrared light detector based on epitaxial Ge/Si. *Applied Physics Letters* **72,** 3175–3177 (1998).

194. Margetis, J., Ghetmiri, S. A., Du, W., Conley, B. R., Mosleh, A., Soref, R., Sun, G., Domulevicz, L., Naseem, H. A., Yu, S.-Q. & Tolle, J. Growth and Characterization of Epitaxial $Ge_{1-x}Sn_x$ Alloys and Heterostructures Using a Commercial CVD System. *ECS Transactions* **64,** 711–720 (2014).

195. Von den Driesch, N., Stange, D., Wirths, S., Mussler, G., Holländer, B., Ikonic, Z., Hartmann, J. M., Stoica, T., Mantl, S., Grützmacher, D. & Buca, D. Direct Bandgap Group IV Epitaxy on Si for Laser Applications. *Chemistry of Materials* **27,** 4693–4702 (2015).

196. De Cesari, S., Balocchi, A., Vitiello, E., Jahandar, P., Grilli, E., Amand, T., Marie, X., Myronov, M. & Pezzoli, F. Spin-coherent dynamics and carrier lifetime in strained $Ge_{1-x}Sn_x$ semiconductors on silicon. *Physical Review B* **99,** 035202 (2019).

197. Marchionna, S., Virtuani, A., Acciarri, M., Isella, G. & Von Kaenel, H. Defect imaging of SiGe strain relaxed buffers grown by LEPECVD. *Materials Science in Semiconductor Processing* **9,** 802–805 (2006).

198. Fitzgerald, E. A., Xie, Y.-H., Green, M. L., Brasen, D., Kortan, A. R., Michel, J., Mii, Y.-J. & Weir, B. E. Totally relaxed Ge_xSi_{1-x} layers with low threading dislocation densities grown on Si substrates. *Applied Physics Letters* **59,** 811–813 (1991).

199. LeGoues, F. K., Meyerson, B. S. & Morar, J. F. Anomalous strain relaxation in SiGe thin films and superlattices. *Physical Review Letters* **66,** 2903–2906 (1991).

200. Hohnisch, M., Herzog, H. J. & Schäffler, F. Relaxation of compositionally graded $Si_{1-x}Ge_x$ buffers: a TEM study. *Journal of Crystal Growth* **157.** Silicon Molecular Beam Epitaxy 1995, 126–131 (1995).

201. Chaisakul, P., Frigerio, J., Marris-Morini, D., Vakarin, V., Chrastina, D., Isella, G. & Vivien, L. O-band quantum-confined Stark effect optical modulator from Ge/Si0.15Ge0.85 quantum wells by well thickness tuning. *Journal of Applied Physics* **116,** 193103 (2014).

202. Birner, S., Zibold, T., Andlauer, T., Kubis, T., Sabathil, M., Trellakis, A. & Vogl, P. nextnano: General Purpose 3-D Simulations. *IEEE Transactions on Electron Devices* **54,** 2137–2142 (2007).

203. Polimeni, A., Patanè, A., Alessi, M. G., Capizzi, M., Martelli, F., Bosacchi, A. & Franchi, S. Stokes shift in quantum wells: Trapping versus thermalization. *Physical Review B* **54,** 16389–16392 (1996).

204. Rouifed, M. S., Chaisakul, P., Marris-Morini, D., Frigerio, J., Isella, G., Chrastina, D., Edmond, S., Roux, X. L., Coudevylle, J.-R. & Vivien, L. Quantum-confined Stark effect at 1.3 μm in Ge/Si(0.35)Ge(0.65) quantum-well structure. *Optics Letters* **37,** 3960 (2012).

205. Gatti, E., Giorgioni, A., Grilli, E., Guzzi, M., Chrastina, D., Isella, G., Chernikov, A., Kolata, K., Bornwasser, V., Köster, N. S., Woscholski, R. & Chatterjee, S. Relaxation and recombination processes in Ge/SiGe multiple quantum wells. *AIP Conference Proceedings* **1566,** 470–471 (2013).

206. Lange, C., Köster, N. S., Chatterjee, S., Sigg, H., Chrastina, D., Isella, G., von Känel, H., Schäfer, M., Kira, M. & Koch, S. W. Ultrafast nonlinear optical response of photoexcited Ge/SiGe quantum wells: Evidence for a femtosecond transient population inversion. *Physical Review B* **79,** 201306 (2009).

207. Kaplan, C. J., Kraus, P. M., Ross, A. D., Zürch, M., Cushing, S. K., Jager, M. F., Chang, H.-T., Gullikson, E. M., Neumark, D. M. & Leone, S. R. Femtosecond tracking of carrier relaxation in germanium with extreme ultraviolet transient reflectivity. *Physical Review B* **97,** 205202 (2018).

208. Pezzoli, F., Bottegoni, F., Trivedi, D., Ciccacci, F., Giorgioni, A., Li, P., Cecchi, S., Grilli, E., Song, Y., Guzzi, M., Dery, H. & Isella, G. Optical Spin Injection and Spin Lifetime in Ge Heterostructures. *Physical Review Letters* **108,** 156603 (2012).

209. Figielski, T. Recombination at dislocations. *Solid-State Electronics* **21,** 1403–1412 (1978).

210. Chosrowjan, H. in *Encyclopedia of Spectroscopy and Spectrometry (Third Edition)* (eds Lindon, J. C., Tranter, G. E. & Koppenaal, D. W.) Third Edition, 654–660 (Academic Press, 2017).

211. Venkatesh, Y., Venkatesan, M., Ramakrishna, B. & Bangal, P. R. Ultrafast Time-Resolved Emission and Absorption Spectra of meso-Pyridyl Porphyrins upon Soret Band Excitation Studied by Fluorescence Up-Conversion and Transient Absorption Spectroscopy. *The Journal of Physical Chemistry B* **120,** 9410–9421 (2016).

212. Bonati, C., Cannizzo, A., Tonti, D., Tortschanoff, A., van Mourik, F. & Chergui, M. Subpicosecond near-infrared fluorescence upconversion study of relaxation processes in PbSe quantum dots. *Physisical Review B* **76,** 033304 (2007).

213. Vitiello, E., Rossi, S., Broderick, C., Gravina, G., Balocchi, A., Marie, X., O'Reilly, E., Myronov, M. & Pezzoli, F. Continuous-Wave Magneto-Optical Determination of the Carrier Lifetime in Coherent $Ge_{1-x}Sn_x$/Ge Heterostructures. *Physical Review Applied* **14** (2020).

214. Pezzoli, F., Balocchi, A., Vitiello, E., Amand, T. & Marie, X. Optical orientation of electron spins and valence-band spectroscopy in germanium. *Physical Review B* **91,** 201201 (2015).

215. Pezzoli, F., Qing, L., Giorgioni, A., Isella, G., Grilli, E., Guzzi, M. & Dery, H. Spin and energy relaxation in germanium studied by spin-polarized direct-gap photoluminescence. *Physical Review B* **88,** 045204 (2013).

216. De Cesari, S., Bergamaschini, R., Vitiello, E., Giorgioni, A. & Pezzoli, F. Optically reconfigurable polarized emission in Germanium. *Scientific Reports* **8,** 11119 (2013).

217. Zelazna, K., Polak, M. P., Scharoch, P., Serafinczuk, J., Gladysiewicz, M., Misiewicz, J., Dekoster, J. & Kudrawiec, R. Electronic band structure of compressively strained $Ge_{1-x}Sn_x$ with $x < 0.11$ studied by contactless electroreflectance. *Applied Physics Letters* **106,** 142102 (2015).

218. Al-Kabi, S., Ghetmiri, S. A., Margetis, J., Du, W., Mosleh, A., Alher, M., Dou, W., Grant, J. M., Sun, G., Soref, R. A., Tolle, J., Li, B., Mortazavi, M., Naseem, H. A. & Yu, S.-Q. Optical Characterization of Si-Based $Ge_{1-x}Sn_x$ Alloys with Sn Compositions up to 12%. *Journal of Electronic Materials* **45,** 2133 (2016).

219. Lieten, R. R., Bustillo, K., Smets, T., Simoen, E., Ager, J. W., Haller, E. E. & Locquet, J.-P. Photoluminescence of bulk germanium. *Physical Review B* **86,** 035204 (2012).

220. Eales, T. D., Marko, I. P., Schulz, S., O'Halloran, E., Ghetmiri, S., Du, W., Zhou, Y., Yu, S.-Q., Margetis, J., Tolle, J., O'Reilly, E. P. & Sweeney, S. J. $Ge_{1-x}Sn_x$ alloys: Consequences of band mixing effects for the evolution of the band gap Γ-character with Sn concentration. *Scientific Reports* **9,** 14077 (2019).

221. O'Halloran, E. J., Broderick, C. A., Tanner, D. S. P., Schulz, S. & O'Reilly, E. P. Comparison of first principles and semi-empirical models of the structural and electronic properties of $Ge_{1-x}Sn_x$ alloys. *Optical and Quantum Electronics* **51,** 314 (2019).

222. Ghetmiri, S. A., Du, W., Margetis, J., Mosleh, A., Cousar, L., Conley, B. R., Domulevicz, L., Nazzal, A., Sun, G., Soref, R. A., Tolle, J., Li, B., Naseem, H. A. & Yu, S.-Q. Direct-bandgap GeSn grown on silicon with 2230nm photoluminescence. *Applied Physics Letters* **105,** 151109 (2014).

223. Parsons, R. R. Band-To-Band Optical Pumping in Solids and Polarized Photoluminescence. *Physical Review Letters* **23,** 1152–1154 (1969).

224. Roth, L. M. & Lax, B. *g* Factor of Electrons in Germanium. *Physical Review Letters* **3,** 217–219 (1959).

225. Guite, C. & Venkataraman, V. Measurement of Electron Spin Lifetime and Optical Orientation Efficiency in Germanium Using Electrical Detection of Radio Frequency Modulated Spin Polarization. *Physical Review Letters* **107,** 166603 (2011).

226. Lohrenz, J., Paschen, T. & Betz, M. Resonant spin amplification in intrinsic bulk germanium: Evidence for electron spin lifetimes exceeding 50 ns. *Physical Review B* **89,** 121201 (2014).

227. Julsgaard, B., von den Driesch, N., Tidemand-Lichtenberg, P., Pedersen, C., Ikonic, Z. & Buca, D. Carrier lifetime of GeSn measured by spectrally resolved picosecond photoluminescence spectroscopy. *Photonic Research* **8,** 788–798 (2020).

228. 't Hooft, G. W., van der Poel, W. A. J. A., Molenkamp, L. W. & Foxon, C. T. Giant oscillator strength of free excitons in GaAs. *Physical Review B* **35,** 8281–8284 (1987).

229. Dominici, S., Wen, H., Bertazzi, F., Goano, M. & Bellotti, E. Numerical study on the optical and carrier recombination processes in GeSn alloy for E-SWIR and MWIR optoelectronic applications. *Optics Express* **24,** 26363–26381 (2016).

230. Stanchu, H. V., Kuchuk, A. V., Mazur, Y. I., Margetis, J., Tolle, J., Yu, S.-Q. & Salamo, G. J. Strain suppressed Sn incorporation in GeSn epitaxially grown on Ge/Si(001) substrate. *Applied Physics Letters* **116,** 232101 (2020).

231. Albani, M., Assali, S., Verheijen, M. A., Koelling, S., Bergamaschini, R., Pezzoli, F., Bakkers, E. P. A. M. & Miglio, L. Critical strain for Sn incorporation into spontaneously graded Ge/GeSn core/shell nanowires. *Nanoscale* **10,** 7250–7256 (2018).

232. Amand, T., Marie, X., Dareys, B., Barrau, J., Brousseau, M., Dunstan, D. J., Emery, J. Y. & Goldstein, L. Well-width dependence of the excitonic lifetime in strained III-V quantum wells. *Journal of Applied Physics* **72,** 2077–2079 (1992).

233. Tran, H., Du, W., Ghetmiri, S. A., Mosleh, A., Sun, G., Soref, R. A., Margetis, J., Tolle, J., Li, B., Naseem, H. A. & Yu, S.-Q. Systematic study of $Ge_{1x}Sn_x$ absorption coefficient and refractive index for the device applications of Si-based optoelectronics. *Journal of Applied Physics* **119,** 103106 (2016).

234. Pezzoli, F., Isa, F., Isella, G., Falub, C. V., Kreiliger, T., Salvalaglio, M., Bergamaschini, R., Grilli, E., Guzzi, M., von Känel, H. & Miglio, L. Ge Crystals on Si Show Their Light. *Physical Review Applied* **1,** 044005 (2014).

235. Kurtz, A. D., Kulin, S. A. & Averbach, B. L. Effects of Growth Rate on Crystal Perfection and Lifetime in Germanium. *Journal of Applied Physics* **27,** 1287–1290 (1956).

236. Kurtz, A. D., Kulin, S. A. & Averbach, B. L. Effect of Dislocations on the Minority Carrier Lifetime in Semiconductors. *Physical Review* **101,** 1285–1291 (1956).

237. Trita, A., Cristiani, I., Degiorgio, V., Chrastina, D. & von Känel, H. Measurement of carrier lifetime and interface recombination velocity in Si–Ge waveguides. *Applied Physics Letters* **91,** 041112 (2007).

238. Grzybowski, G., Roucka, R., Mathews, J., Jiang, L., Beeler, R. T., Kouvetakis, J. & Menéndez, J. Direct versus indirect optical recombination in Ge films grown on Si substrates. *Physical Review B* **84,** 205307 (2011).

239. Geiger, R., Frigerio, J., Süess, M. J., Chrastina, D., Isella, G., Spolenak, R., Faist, J. & Sigg, H. Excess carrier lifetimes in Ge layers on Si. *Applied Physics Letters* **104,** 062106 (2014).

240. Srinivasan, S. A., Pantouvaki, M., Verheyen, P., Lepage, G., Absil, P., Van Campenhout, J. & Van Thourhout, D. Extraction of carrier lifetime in Ge waveguides using pump probe spectroscopy. *Applied Physics Letters* **108,** 211101 (2016).

241. Malyutenko, V. & Chyrchyk, S. Surface recombination velocity in Si wafers by photoinduced thermal emission. *Applied Physics Letters* **89,** 051909 (2006).

242. Palais, O. & Arcari, A. Contactless measurement of bulk lifetime and surface recombination velocity in silicon wafers. *Journal of Applied Physics* **93,** 4686–4690 (2003).

243. Kuwayama, T., Ichimura, M. & Arai, E. Interface recombination velocity of silicon-on-insulator wafers measured by microwave reflectance photoconductivity decay method with electric field. *Applied Physics Letters* **83,** 928–930 (2003).

244. Peng, L., Li, X., Liu, Z., Liu, X., Zheng, J., Xue, C., Zuo, Y. & Cheng, B. Horizontal GeSn/Ge multi-quantum-well ridge waveguide LEDs on silicon substrates. *Photonic Research* **8,** 899–903 (2020).

245. Li, Q., Xu, S. J., Xie, M. H. & Tong, S. Y. A model for steady-state luminescence of localized-state ensemble. *Europhysics Letters* **71,** 994–1000 (2005).

246. Pezzoli, F., Giorgioni, A., Patchett, D. & Myronov, M. Temperature-Dependent Photoluminescence Characteristics of GeSn Epitaxial Layers. *ACS Photonics* **3,** 2004–2009 (2016).

247. Li, Q., Xu, S. J., Xie, M. H. & Tong, S. Y. Origin of the 'S-shaped' temperature dependence of luminescent peaks from semiconductors. *Journal of Physics: Condensed Matter* **17,** 4853–4858 (2005).

248. Martini, S., Quivy, A. A., Tabata, A. & Leite, J. R. Influence of the temperature and excitation power on the optical properties of InGaAs/GaAs quantum wells grown on vicinal GaAs(001) surfaces. *Journal of Applied Physics* **90,** 2280–2289 (2001).

249. Jin, S., Zheng, Y. & Li, A. Characterization of photoluminescence intensity and efficiency of free excitons in semiconductor quantum well structures. *Journal of Applied Physics* **82,** 3870–3873 (1997).

250. Fouquet, J. & Burnham, R. Recombination dynamics in GaAs/$Al_xGa_{1-x}As$ quantum well structures. *IEEE Journal of Quantum Electronics* **22,** 1799–1810 (1986).

251. Pavarelli, N., Ochalski, T. J., Murphy-Armando, F., Huo, Y., Schmidt, M., Huyet, G. & Harris, J. S. Optical Emission of a Strained Direct-Band-Gap Ge Quantum Well Embedded Inside InGaAs Alloy Layers. *Physical Review Letters* **110,** 177404 (2013).

252. Böhrer, J., Krost, A. & Bimberg, D. Spatially indirect intersubband transitions of localized electrons and holes at the staggered band lineup $In_{0.52}Al_{0.48}As$/InP interface. *Journal of Vacuum Science & Technology B: Microelectronics and Nanometer Structures Processing, Measurement, and Phenomena* **11,** 1642–1646 (1993).

253. Böhrer, J., Krost, A. & Bimberg, D. Carrier dynamics in staggered-band lineup n-InAlAs/n-InP heterostructures. *Applied Physics Letters* **64,** 1992–1994 (1994).

254. Ledentsov, N. N., Böhrer, J., Beer, M., Heinrichsdorff, F., Grundmann, M., Bimberg, D., Ivanov, S. V., Meltser, B. Y., Shaposhnikov, S. V., Yassievich, I. N., Faleev, N. N., Kop'ev, P. S. & Alferov, Z. I. Radiative states in type-II GaSb/GaAs quantum wells. *Physical Review B* **52,** 14058–14066 (1995).

255. Weisbuch, C. & Vinter, B. *Quantum semiconductor structures: fundamentals and applications* (Elsevier, 2014).

256. Hatami, F., Grundmann, M., Ledentsov, N. N., Heinrichsdorff, F., Heitz, R., Böhrer, J., Bimberg, D., Ruvimov, S. S., Werner, P., Ustinov, V. M., Kop'ev, P. S. & Alferov, Z. I. Carrier dynamics in type-II GaSb/GaAs quantum dots. *Physical Review B* **57,** 4635 (1998).

257. Kazlauskas, K., Tamulaitis, G., Mickevičius, J., Kuokštis, E., Žukauskas, A., Cheng, Y.-C., Wang, H.-C., Huang, C.-F. & Yang, C. Excitation power dynamics of photoluminescence in In GaN/GaN quantum wells with enhanced carrier localization. *Journal of Applied Physics* **97,** 013525 (2005).

258. Jonker, B. T., Kioseoglou, G., Hanbicki, A. T., Li, C. H. & Thompson, P. E. Electrical spin-injection into silicon from a ferromagnetic metal/tunnel barrier contact. *Nature Physics* **3,** 542–546 (2007).

259. Liu, Y., Besbas, J., Wang, Y., He, P., Chen, M., Zhu, D., Wu, Y., Lee, J. M., Wang, L., Moon, J. & Nikesh Koirala, S. O. H. Y. Direct visualization of current-induced spin accumulation in topological insulators. *Nature Communications* **9,** 1–6 (2018).

260. Patane, A. & Balkan, N. *Semiconductor Research: Experimental Techniques* (Springer Science & Business Media, 2012).

261. Sierra, J. F., Fabian, J., Kawakami, R. K., Roche, S. & Valenzuela, S. O. Van der Waals heterostructures for spintronics and opto-spintronics. *Nature Nanotechnology* **16,** 856–868 (2021).

262. Lin, X., Su, L., Si, Z., Zhang, Y., Bournel, A., Zhang, Y., Klein, J.-O., Fert, A. & Zhao, W. Gate-Driven Pure Spin Current in Graphene. *Physical Review Applied* **8,** 034006 (3 2017).

263. Manipatruni, S., Nikonov, D. E. & Young, I. A. Beyond CMOS computing with spin and polarization. *Nature Physics* **14,** 338–343 (2018).

264. `https://www.horiba.com/fileadmin/uploads/Scientific/Documents/OSD/OBB/cameras/Synapse-Linear-InGaAs-Array-Camera.pdf`.

265. `https://www.hamamatsu.com/eu/en/product/type/R5509-73/index.html`.

266. Schaefer, B., Collett, E., Smyth, R., Barrett, D. & Fraher, B. Measuring the Stokes polarization parameters. *American Journal of Physics* **75,** 163–168 (2007).

267. Stokes, G. G. On the Composition and Resolution of Streams of Polarized Light from different Sources. *Transactions of the Cambridge Philosophical Society* **9,** 399–416 (1852).

268. Wolf, E. Optics in terms of observable quantities. *Il Nuovo Cimento* **12,** 884–888 (1954).

269. Temperature dependence of the energy gap in semiconductors. *Physica* **34,** 149–154 (1967).

270. Wu, P. H., Huang, Y. S., Hsu, H. P., Chrastina, D., Isella, G., von Känel, H. & Tiong, K. K. Temperature dependence of the direct interband transitions of a Ge/SiGe multiple-quantum-well structure with Ge-rich barriers. *Physical Review B* **85,** 035303 (2012).

Acknowledgments

Since the very beginning I want to thank my supervisor, Prof. Fabio Pezzoli, as he guided me through this beautiful experience that lasted three years. He assisted me thoroughly through my journey without hesitation while offering me his patience and competence. I will always be thankful for his support. He showed me what it means to have passion for science and he gave me a bright example of how someone should love his own work. A significant portion of the wonder I experienced is, for sure, thanks to him.

Nevertheless, an equally significant importance lies in the people I was lucky to work with. I am grateful to Elisa Vitiello, who greeted me the very first time I stepped into the office and who taught me everything I had to know to grow as an experimentalist. Like Fabio, she showed me how to successfully be a scientist as well as a parent. I want to thank Jacopo Pedrini for the constant help that he gave me and the fruitful conversations we had during all these years. His ability to make me laugh even during stressful moments has been, to me, an invaluable blessing. A huge recognition goes to Luca Barbisan, who shared with me beautiful moments both in the university as well as outside, those moments are very precious to me. All the funny theories developed during the lunch breaks will not fade away! Special mention also goes to Prof. Emiliano Bonera, who lent me a hand various times during these three years, I really appreciated his kindness. I can not forget Prof. Emanuele Grilli, who provided me with his knowledge and with many solutions in the experimental problems I faced. Thanks to Stefano Vichi, who helped me in overcoming the barriers I found with coding in a delicate moment of my PhD. Thank to Giorgio, Valentina, Andrea, Marta, Luciano, Stefano, Ian, Mario, Cristina and many others, for sharing valuable moments with me.

I can say without hesitation that I have found a second family within this group.

During the first half of my second year I spent six months at The University

of Warwick. I thank Prof. Maksym Myronov for accepting me into his group and offering me the possibility to experience a different approach to the semiconductor field. I am grateful to Dr. Gerard Colston and Pedram Jahandar for their support during my abroad period.

I would like to thank Dr. Enrico Talamas Simola, Prof. Giovanni Isella and Dr. Andrea Ballabio from the L-NESS group for providing me with the $Si_{1-x}Ge_x$ samples.

Last but not the least I have to endlessly thank my family as I have always been supported in my choices, especially those about my will to continue my studies.

Thank you